

UC Berkeley

UC Berkeley Electronic Theses and Dissertations

Title

Investigating Physicochemical Principles for Sample Preparation and Detection From Single-cell Immunoblots

Permalink

<https://escholarship.org/uc/item/2k22p81c>

Author

Tan, Kristine Y.

Publication Date

2021

Peer reviewed|Thesis/dissertation

Investigating Physicochemical Principles for Sample Preparation and Detection From
Single-cell Immunoblots

by

Kristine Yan-Ling Tan

A dissertation submitted in partial satisfaction of the

requirements for the degree of

Joint Doctor of Philosophy
with University of California, San Francisco

in

Bioengineering

in the

Graduate Division

of the

University of California, Berkeley

Committee in charge:

Professor AmyE. Herr , Chair
Professor Bo Huang
Professor Markita Landry

Summer 2021

Investigating Physicochemical Principles for Sample Preparation and Detection From
Single-cell Immunoblots

Copyright 2021
By
Kristine Yan-Ling Tan

Abstract

Investigating Physicochemical Principles for Sample Preparation and Detection From Single-cell Immunoblots

by

Kristine Yan-Ling Tan

Joint Doctor of Philosophy
With University of California, San Francisco in Bioengineering
University of California, Berkeley

Professor Amy E. Herr, Chair

Proteins are complex molecules that carry out diverse actions in cells for proper structure, function, and regulation in any organism. Proteins are encoded by genes, but can undergo modifications not encoded by DNA, that result in differences in function, even amongst proteins of the same type. These modifications beget protein isoforms, or variants of the same protein, that can have different biological functions and alter the behavior of an individual cell. Differences at the single-cell level can result in subpopulations of cells of heterogeneous behavior that can influence stem cell differentiation, disease development, and the efficacy of drug treatments. In order to understand and predict these phenomena, it is important to detect protein isoforms at the single-cell level. However, specific detection of the modifications that distinguish protein isoforms with single-cell resolution sensitivity remains challenging. To address the challenge of protein isoform detection, single-cell electrophoretic cytometry (scEPC) methods have been developed. scEPC leverages microscale transport phenomena and timescales to perform separations on individual cells to distinguish protein isoforms prior to detection via conventional immunoassay. Here, we advance our understanding of scEPC to guide assay design.

First, we characterize separation and detection performance with different gel pore size to interrogate large ranges of protein molecular masses that are relevant to protein signaling pathways. Furthermore, through our understanding of mathematical models established for bulk, (non-single cell) separations, we elucidate and identify anomalous protein electromigration behavior for large molecular mass proteins. The anomalous migration indicates further optimization of the cell lysis and protein solubilization sample preparation steps of our assay is potentially required for larger molecular mass targets.

Next, we aim to reduce fluorescence background for in-gel immunoassays that results from using benzophenone as a photoactivatable molecule for immobilizing protein in the gel matrix for subsequent fluorescence detection. We hypothesize that the benzophenone chemical structure, which contains two aromatic rings, contributes to increased fluorescence background signal due to autofluorescence and increased hydrophobic interactions that non-specifically interact with fluorescent immunoprobables to retain the immunoprobables in the gel matrix. We investigate an alternative photoactivatable molecule, diazirine, a three-membered ring comprised of two nitrogen atoms and one carbon atom, to reduce background fluorescence signal and enable detection lower abundance isoforms. Due to the chemical structure diazirine, we hypothesize that diazirine has lower autofluorescence compared to benzophenone. Furthermore, diazirine is a more hydrophilic molecule, which we hypothesize will reduce non-specific interaction with immunoprobables compared to benzophenone. Thus, we determine how to appropriately evaluate and compare diazirine and benzophenone, with regard to metrics important for in-gel immunoassay fluorescence background and signal.

Lastly, we begin preliminary investigations to measure subcellular estrogen receptor- α (ER α) isoform expression from the cell membrane, cytoplasm, and nucleus using two approaches. To detect membrane-localized isoforms, we utilize a ligand that binds to ER α and is conjugated to a bulky molecule to pull down and isolate membrane-localized protein. To differentiate cytoplasmic and nuclear localized isoforms, we investigate efficacy of employing differential detergent fractionation chemistry and bi-directional electrophoretic separations. We anticipate that the finding presented here will advance assay capability to detect a wide range of protein isoform targets.

To my family and friends

Table of Contents

Table of Contents	ii
List of Figures.....	iv
List of Tables.....	vi
Acknowledgements	vii
Chapter 1 : Introduction.....	1
1.1 Introduction	1
1.2 Cell Lysis with Detergents for In-Gel Single-Cell Lysis	3
1.3 Protein electrophoretic mobility in polyacrylamide gel electrophoresis	6
1.4 Detection of protein targets following electrophoretic separations	8
1.5 References.....	10
Chapter 2 : Ferguson analysis of protein electromigration during single-cell electrophoresis in an open microfluidic device	13
2.1 Introduction	13
2.2 Materials and Methods.....	15
2.3 Results and Discussion.....	17
2.4 Conclusions	27
2.5 References.....	29
Chapter 3 : Comparison of Photoactivatable Crosslinkers for In-Gel Immunoassays ...	33
3.1 Introduction	33
3.2 Materials and Methods.....	34
3.3 Results and Discussion.....	38
3.4 Conclusions and Future Directions	45
3.5 Appendix	46
3.6 References.....	47
Chapter 4 : Western blotting using an offset electrode configuration during electrotransfer	50
4.1 Introduction	50
4.2 Results and Discussion.....	51
4.3 Conclusion & Next Steps	62
4.4 Appendix	63
4.6 References.....	68
Chapter 5 : Developing Methods to Measure the Sub-Cellular Localization of Estrogen Receptor- α (ER α) Isoforms	69
5.1 Introduction	69
5.2 Materials and Methods.....	70
5.3 Results and Discussion.....	73
5.4 Conclusions and Future Directions	83
5.5 References.....	83
Chapter 6 : Conclusions and Future Directions.....	87
Appendix	88

A. RT-qPCR experiments for analysis of mRNA transcript expression after drug treatment	88
A.1 Method.....	88
A.2 Results and Discussion	88
A.3 Supplementary Information.....	91

List of Figures

Figure 1-1 Workflow for single-cell electrophoretic protein cytometry.	2
Figure 2-1: Dependence of migration distance on protein molecular mass in three different gel compositions.	19
Figure 2-2: Additional false-color fluorescence micrographs and intensity plots of electromigration for PTBP1, HSP90, SFPQ, and Vinculin protein targets.	20
Figure 2-3. Ferguson and calibration plots for 5 protein targets detected from single cells that were lysed on-chip.	22
Figure 2-4. Standard curves of logarithmic molecular mass vs normalized migration for single-cell SDS-PAGE in an open microfluidic device.	24
Figure 2-5: Comparisons of different fluorescent protein signal characteristics between 5%T and 8%T gels for all five immunoprobed protein targets.	25
Figure 2-6. Percent of the peaks that pass QC in the MATLAB scripts and have SNR \geq 3.	27
Figure 3-1 In-gel protein capture of DyLight 633 labelled protein target in DZA and BPMAC functionalized hydrogels.	39
Figure 3-2 Measuring sources that contribute to increased background fluorescence for in-gel immunoassays.	41
Figure 3-3 Utilizing DZMA hydrogels for single-cell immunoblotting to detect PTBP1 from MDA-MB-231 breast cancer cells.	43
Figure 3-4 Swelling ratios (Q) of 0 mM, 12mM DZMA hydrogels and 3 mM BPMA hydrogels in a polar solvent, water (A) and nonpolar solvent 70% IPA (B).	44
Figure 3-5 AUC and SNR analysis of purified labelled ovalbumin after native microscale separations using 1x Tris-glycine run buffer.	45
Figure 3-6: Confirmation of diazirine identity and purity.	47
Figure 4-1: Finite element analysis model of electric field magnitude and electrical current path in various electrotransfer system designs.	52
Figure 4-2: Relationship between μ to any combination of MW and %T	54
Figure 4-3: Experimental results of using offset electrode configuration to perform electrotransfer in forward and reverse orientations	56
Figure 4-4: Experimental results of using offset electrode configuration to transfer protein out of thin gels	58
Figure 4-5: Finite element analysis model of electric field magnitude and electrical current path in Gen 1.1 design	59
Figure 4-6: Finite element analysis model of electric field magnitude and electrical current path in Gen 2.0 design	60
Figure 4-7: Finite element analysis model of electric field magnitude and electrical current path in Gen 2.1 design	61
Figure 4-8: Comparison of the EZ magnitude at the active transfer area in all electrotransfer system.	62
Figure 4-9: Schematic of step-by-step NetFix gel fabrication.	64
Figure 5-1. Internal 'ladder' protein controls of known molecular weight are used to predict migration distance of our complex of interest in different gel compositions.	75
Figure 5-2: Single-cell pull down blot of MCF-7 cells with E2-BSA-FITC stimulation reveals the membrane-bound E2-BSA-FITC ligand.	76

Figure 5-3: Number of microwells with ER- α 66 signal that also had FITC signal.....	76
Figure 5-4: Detection of GFP protein localized to the cytoplasmic fraction and nuclear PTBP1 localized to the nucleus after performing scDDF.....	77
Figure 5-5: Detection of three cytoplasmic proteins in the nuclear fraction after performing scDDF.....	78
Figure 5-6: False-colored micrographs of a microwell containing a naïve MCF-7 cell that has been treated with fluorescently labelled wheat germ agglutinin that bind specifically to the plasma membrane, as it undergoes cytoplasm-specific lysis (left) and electrophoresis (right).....	79
Figure 5-7: Increasing concentration of Triton X-100 in cytoplasmic lysis buffer formulation does not improve detection of cytoplasmic proteins.	80
Figure 5-8: Heating cytoplasmic lysis buffer with convection delivery solubilizes β -tubulin.....	81
Figure 5-9: Increasing lysis times for the cytoplasmic lysis step did not improve detection of cytoplasmic proteins.	82
Figure A-1: Effect of Tamoxifen and E2 treatments on ER α mRNA expression.....	89
Figure A-2: Effect of Tamoxifen and E2 treatments on corresponding mRNA transcripts from ER α signaling pathways for MDA-MB-231 and MC-7 cell lines.	90
Figure A-3: Δ Ct values for ER α mRNA transcript expression.....	91
Figure A-4: Δ Ct values for signaling pathway mRNA transcript expression for additional transcripts.....	92
Figure A-5: Schematic of ER α protein domains and how they map to the mRNA transcript sequence.....	94
Figure A-6: RT-qPCR product run on a 2% agarose gel.....	95
Figure A-7: RT-qPCR product run on a 2% agarose gel with SYBR safe stain.	96
Figure A-8: Location of new primers ordered (blue)	96

List of Tables

Table 1-1 Comparison of properties and attributes of benzophenone and diazirine as photoactivatable molecules for protein crosslinking	9
Table 2-1. Predicted Size of mTOR from Migration Distance	21
Table 2-2. Extrapolated y-intercepts (free solution mobility) from Ferguson Plot	23
Table 2-3. Predicted Size-Exclusion limits	24
Table A-1: RT-qPCR Primers used in experiments.	93
Table A-2: List and description of primers tested using RT-qPCR.....	93

Acknowledgements

Grad school has not been an easy journey. It has challenged me and pushed me beyond what I previously encountered during undergrad and my time in industry. I am so thankful for all the mentors, friends, and people who have supported me on this academic journey. I have been fortunate to be surrounded by some of the most caring people who inspire me to become a better person and scientist.

First off, I am so thankful for Professor Amy E. Herr who I feel privileged to have had the opportunity to learn from and complete my Ph.D. in her group. Amy has pushed me to a higher standard both as a scientist and engineer and as a person. Amy is a role model with her tireless dedication to her work both in the lab and with the broader community. Under Amy's mentorship, I have developed the skills to not only critically ask questions, design effective experiments, and analyze data, but also to communicate those results clearly and effectively. I am forever grateful that she accepted me into the lab and for all the support and opportunities that she provided.

In addition to Amy, the entire Herr lab has been filled with the most dedicated and kind people I have ever met. Everyone I've interacted with in the lab, as well as previous lab members who I've met outside of the lab, has been a role model and set the standard to become a better scientist. I am grateful for guidance provided by Ginny, Kevin, Eli, Elaine, Shaheen, and Sam and especially grateful for those who have more directly mentored me. From initial mentors Julea and John who took the time to answer my questions, discuss projects, and demonstrate experimental protocols to Hector and Anjali who I've been able to turn to for any random advice and who were not afraid to give me blunt constructive feedback when I needed it. I am also grateful to have joined the Herr Lab with three outstanding individuals and scientists. Ali, Alisha, and Andoni have been peers who set examples I aspire to, leading the way and being companions during the Ph.D. journey. Safe to say, I cannot imagine graduate school without their company. And last but definitely not least, Gabi and Louise who have taught me so much both inside and outside the lab. I've been so grateful to have co-workers who not only indulge my antics but also push me out of my comfort zone and take me outside of the lab on adventures.

Next, I want to thank my family and friends. Both my immediate and extended family for always being there and supportive. My parents' initial encouragement to pursue science and math have led me here today. And even though they may not understand the exact nature of my work and what I am doing, I know I can rely on my parents and brother to provide advice on any other questions which has allowed me to focus on my work. I am thankful for all the friends who have stuck with me throughout this Ph.D. From the friends I've made during grad school back all the way back to friends from high school. The entire BEAST community has been full of friendly and welcoming faces. Specific friends from the same cohort, outside of the Herr lab, such as Kristen, Marc, Priya and Anushka who I've shared the joys and pains of grad school with. I am especially thankful for Priya and Alisha for being amazing and patient housemates who tolerated my weird late-night hours, Anushka and Siddhesh for always inviting me to eat Indian food, and Anushka for always being willing to discuss random topics from our most recent experimental results to the newest boba store that opened up. I am eternally grateful for the friends I made during my time at Illumina such as

Michelle and Alvin who have always welcomed me into their home, feeding me, introducing me to tea, and letting me play with their cats; and Chris, Avi, and Peter who always make me laugh. Special shoutout to my friends from undergrad, especially Olivia who has been there to commiserate the pains of grad school with me and is always the first person I turn to when I want to share any piece of news from the most insignificant detail of what I ate for lunch to the milestones of submitting a manuscript or passing my qualifying exam. And my other friends from undergrad who have supported me even though our lives have diverged to very different paths: Tiffany, Lisa, Neil, Chris, Josh, and Juwon have all provided a welcoming space for me to escape to when grad school became too overwhelming.

I also want to give special thanks to all previous mentors. From my high school AP Bio teacher Mr. Williamson and my tennis coach Steve Yu who were constant sources of encouragement and always had faith that I could succeed even when I had my worst doubts. Additionally, I want to thank my undergraduate research mentors Prof. Neil Chi and Prof. Koichi Masuda who introduced me to and further developed my interests in research, providing opportunities for me to explore and shape my career.

I would also like to thank the members of my qualifying exam and dissertation committees: Prof. Dorian Liepmann, Prof. Aaron Streets, Prof. Bo Huang, and Prof. Markita Landry. Their input and guidance was very helpful as I shaped my research projects and eventual dissertation. Finally, I would like to thank the organizations that financially supported our research. The National Institutes of Health, the Chan Zuckerberg Biohub, and Thermo Fisher Scientific. Without their financial support, the research we performed would not have been possible.

Chapter 1: Introduction

1.1 Introduction

Even across a population of the same type of cells there are differences in the genes and proteins that are expressed, and thus differences in the signaling pathways that are active in a cell. These differences can result in heterogeneous outcomes in stem cell differentiation, disease development, and the efficacy of drug treatments. Thus, it is important to detect and understand these differences at the single-cell level to capture the full response amongst a population of cells. Proteins are the molecular machinery that carry out functions in the cell, from sensing and responding to external stimuli, forming the structure of the cell, or participating in cell signaling pathways and thus are important targets to study at the single-cell level.

However, proteins are also not a heterogeneous population and different protein isoforms or proteoforms, which are different forms of a protein, exist¹. Proteoforms can have different functions resulting in different biological outcomes. For example, detection of estrogen receptor- α (ER- α) dictates breast cancer (BCa) treatment, but the presence of ER- α isoforms in cell subpopulations confounds targeted therapy outcomes. ER- α 46 and ER- α 36 are both truncated isoforms overlooked during BCa classification, but both can impact drug efficacy. While ER- α 46 blocks downstream signaling² and restores drug sensitivity³, ER- α 36 activates pathways leading to cell growth, survival, and invasion^{4,5}. Thus, the detection of distinct ER- α isoforms is necessary for improved prognosis of patient response to therapies.

Isoforms can arise from variations in sequence, alternative splicing of mRNA transcripts, and through posttranslational modifications¹. However, detecting isoform is challenging due to the lack of probes specific to unique isoforms and lack of resolution to detect isoform expression in cell subpopulations. Thus, tools able to distinguish different isoforms are critical to understanding the impact of isoforms on different biological outcomes. Separation science provides methods to distinguish molecules based on differences in physicochemical properties and identify different protein isoforms. Electrophoretic protein separations are therefore powerful tools to detect isoforms, as proteoforms can be distinguished and separated based on physicochemical properties such as protein size, shape, or net charge before detection with a target-specific probe such as an antibody. Understanding and developing measurement tools to address the need for single-cell isoform detection motivates the work in this dissertation.

Single-cell electrophoretic protein cytometry (scEPC) can overcome isoform measurement challenges by utilizing microfluidics to perform size-based protein separations on individual cells to distinguish truncated isoforms prior to detection by conventional immunoassay^{6,7}. The work presented in subsequent chapters discusses our understanding and advances for scEPC to measure proteoforms from single-cells.

To perform single-cell electrophoretic protein cytometry, a single polyacrylamide gel substrate is used for single-cell isolation, cell lysis and protein solubilization with detergents, electrophoretic separation of proteins from cell lysate, covalent immobilization of protein, and introduction of target-specific probes for detection⁷ (

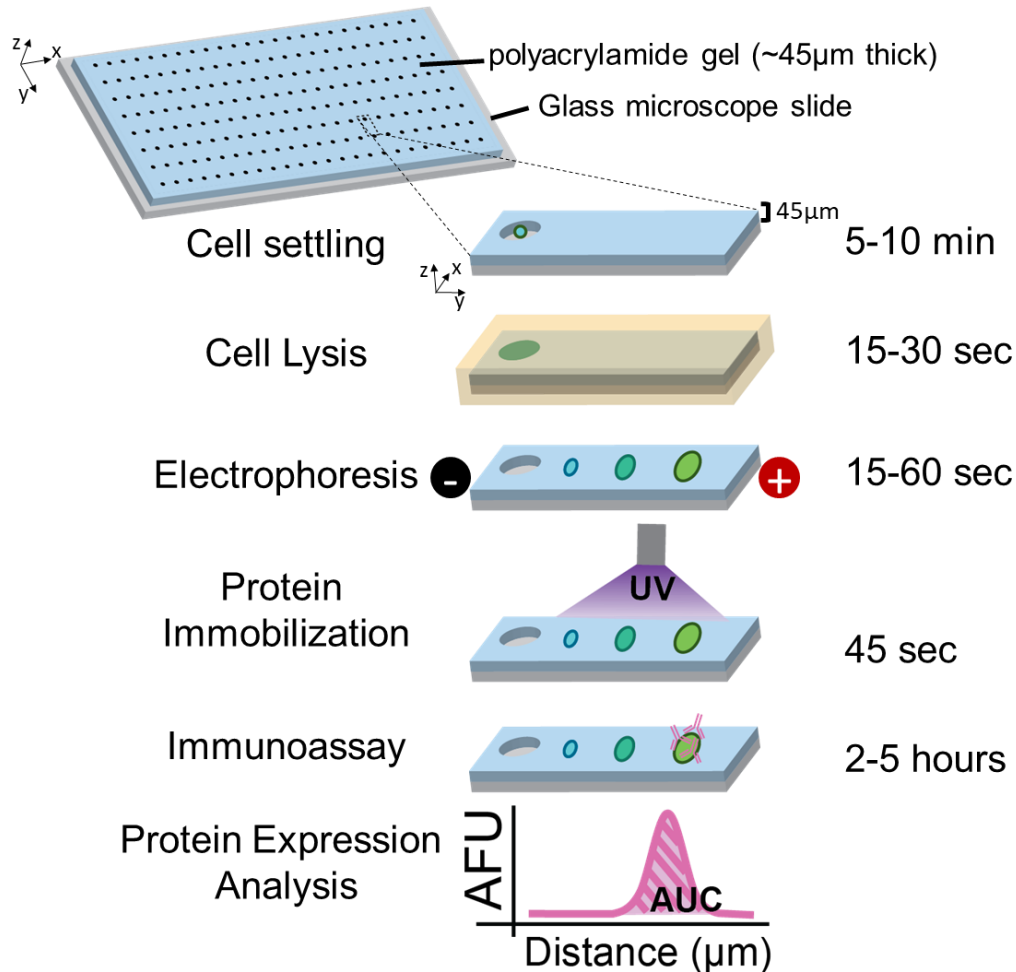


Figure 1-1 Workflow for single-cell electrophoretic protein cytometry. A thin ~45µm hydrogel contains an array of microwells. Single cells are gravity settled into an array of microwells for subsequent cell lysis and protein solubilization. Following cell lysis, an electric field is applied to inject and separate proteins from the cell lysate into the polyacrylamide gel adjacent to the microwell. Immediately following protein separation, once the electric field turned off, the entire gel is exposed to UV light to activate a benzophenone moiety, that was incorporated in the gel precursor, to covalently crosslink protein to the gel matrix. Protein targets are then detected directly in the gel matrix through diffusively introducing fluorescently labeled, target-specific probes to the gel. The entire gel is then imaged on a fluorescence microarray scanner and image analysis is performed to obtain average intensity profiles for each protein target for each individual cell. Gaussian fitting is performed for each protein peak to quantify relative protein expression as the area under the curve of the Gaussian peak.

We devote the remainder of this chapter to understand the fundamental physicochemical phenomena that guide assay performance, from sample preparation to protein immobilization and detection.

1.2 Cell Lysis with Detergents for In-Gel Single-Cell Lysis

In order to perform electrophoresis and separate out individual protein molecules or complexes, proteins must first be extracted from the biological sample of interest and purified to remove contaminants or substances that interfere with detection of the target molecule of interest⁸. Additionally, during the separation to isolate the protein target of interest, it is necessary that proteins are solubilized in solution. However, this is a challenge with biological samples due to the complex network and structure of cells. The cell is organized into compartments, or organelles, that are often surrounded by a membrane. Furthermore, the cell itself has an outer plasma membrane that acts as a selective barrier to preserve the internal components while keeping foreign material out of the cell. Moreover, inside the cell, protein molecules interact with each other to form protein complexes. Thus, in order to access the protein target molecules, it is necessary to break down not only the membranes that act as barriers but also break apart protein complexes, all without damaging the target molecules of interest.

To accomplish this, proteins must be solubilized, which is defined as the disruption of noncovalent protein interaction with other components⁸. This is distinct from protein denaturation which is the disruption of the native, functional protein state by breaking the interactions (bonds) that hold the protein together. Forces of varying strength are involved in protein binding and types of interactions include disulfide bonds, hydrogen bonds, electrostatic interactions, charge-dipole interactions, dipole-dipole interactions, Van der Waals forces, and hydrophobic interactions⁸. Depending on the location of the protein and the nature of the interactions the protein is involved with, different strength detergents are necessary to isolate the protein target of interest. However, stronger detergents may lead to protein denaturation, so there must be a balance between the intermolecular and intramolecular interaction and disruptive capacity of the solubilization medium that determines if proteins are solubilized or denatured. For example, transmembrane proteins contain hydrophobic regions in order to interact with the hydrophobic tails of the lipid bilayer. These hydrophobic regions can be difficult to solubilize in aqueous solutions without first denaturing the protein. Thus, in order to successfully solubilize membrane proteins, stronger detergents are necessary, however stronger detergents also serve to denature the protein such that it is no longer functional after purification and isolation.

Factors that can denature proteins include heat, changes in pH or salinity of the solution, organic solvents, irradiation, denaturant chemicals, and detergents. Detergents, which for molecular biology applications is synonymous with surfactants (surface active agents), are molecules that bind to and denature protein⁹. They have a general structure that is amphipathic, meaning they have a hydrophobic tail and hydrophilic head. The head group determines how soluble the surfactant is in water and can be classified as nonionic (e.g. Triton X-100), ionic (anionic e.g. sodium dodecyl sulfate or cationic e.g. CTAB), and zwitterionic (e.g. CHAPS)⁹. As a general pattern, surfactants with a larger headgroup and longer hydrocarbon chain have milder properties and surfactants with a short hydrocarbon chain are more likely to denature and disrupt protein complexes⁹.

Nonionic detergents have an uncharged head group and are generally milder and non-denaturing¹⁰. Nonionic detergents are used to disrupt protein-lipid and lipid-lipid interactions and are thus useful to permeabilize cells¹⁰. Proteins that are solubilized in nonionic detergent retain their tertiary structure and thus retain functional activity of the protein. Examples of nonionic detergents include Triton X-100, digitonin, maltosides, glucosides, and polyoxyethylene glycols¹⁰. Each nonionic detergent can have specific residues they preferentially interact with. For example, digitonin selectively interacts and binds to cholesterol in the cell membrane, breaking apart the cell membrane as it binds¹¹ but leaves other non-cholesterol-rich membranes (such as the mitochondrial membrane) intact^{12,13}.

Ionic detergents are generally harsher and denaturing. They disrupt inter- and intramolecular protein-protein interactions. Examples of anionic detergents include sodium dodecyl sulfate (SDS) and sodium deoxycholate (NaDoc). An example of a cationic detergent is cetrimonium bromide (CTAB). SDS binds to protein at a fixed ratio of 1.4 g SDS per 1 g of protein, which is a critical feature for enabling size-based separations⁸. This fixed binding ratio normalizes the protein charge-to-mass ratio, such that the charge of an individual protein molecule is proportional to its molecule weight and proteins are separated based on size.

Zwitterionic detergents contain an equal positive and negative charge in the head group such that they are net neutral and are intermediate disruption of protein interactions (in between nonionic and ionic detergents)^{10,14}. However, the net charge can change based on the pH of the solution and it is important in isoelectric focusing that zwitterions have a net neutral charge across the entire range of interest. Zwitterionic detergents combine the properties of ionic and nonionic detergents. Zwitterions are more deactivating than nonionic detergent and may disrupt protein-protein interactions but are still non-denaturing, which makes zwitterions useful for studying membrane proteins. Examples include CHAPS and lauryldimethyl amine oxide (LDAO)¹⁴.

In solution, detergent molecule form micelles with the hydrophobic tails aligned to the center of the micelles and the hydrophilic headgroup on the outside, interfacing with the solution¹⁵. The shape of the micelle depends on the relative size of the head-to-tail and the aggregation number which is the number of monomers in the micelle¹⁵. The critical micelle concentration (CMC) is the minimum concentration of detergent at which micelles form and is dependent on temperature and changes in the solvent environment^{9,15}. Below the CMC, the detergent molecules exist as monomers⁹. Above the CMC, the monomer concentration is constant, but the micelle concentration increases. When detergents solubilize hydrophobic and amphipathic molecules, mixed micelles are formed¹⁵.

In order to perform electrophoresis to study proteins, it is necessary solubilize protein to use detergents to 1) extract the protein target(s) of interest from the biological sample, 2) purify the protein target(s) from contaminants and interfering substances, and 3) keep the protein target(s) in solution during the separation process, preventing precipitation and aggregation of the protein⁸. However, it can be challenging to solubilize proteins

from biological samples due to cellular biological membranes, such as the plasma and nuclear membrane. In order to solubilize protein, the phospholipid membrane must first be solubilized.

The process of phospholipid membrane solubilization has been studied *in vitro* with pure phospholipid membranes and happens in three general steps¹⁶. During the first step, the monomer detergent partitions into the phospholipid bilayer¹⁶. Next, the membrane becomes saturated with the incorporated detergent, forming a mixed lipid-detergent micelle¹⁶. Finally, the phospholipid bilayer is fully solubilized by detergent micelles¹⁶. In biological membranes that contain protein, solubilization occurs in four general steps¹⁷. The process starts again with detergent monomers partitioning into the phospholipid bilayer. Next, detergent-detergent interactions destabilize the bilayer structures to fragment the membrane. Then lipid-protein units start becoming solubilized as sheets or micelles^{14,17}. Finally, solubilization is achieved when there are mixed micelles of lipid and detergent or detergent and protein^{14,17}.

There are two proposed models for how detergents bind to proteins: the decorated micelle model and the necklace-and-beads models. The decorated micelle model proposes that the extended protein wraps around the micelle¹⁸. The necklace-and-beads model (also called the pearl and necklace model) proposes that electrostatic repulsion between micelles denatures the protein and micelles form on different parts of the extended protein¹⁸. With nonionic and zwitterionic detergents, proteins are only denatured about the CMC¹⁸. With ionic detergents, protein unfolding can begin below the CMC¹⁸.

In addition to detergents, chaotropes, which are chemical denaturants that disrupt noncovalent protein interactions, can also be used for protein sample preparation⁸. The exact mechanism of chaotropes is still debated. Either chaotropes bind directly to protein or chaotropes indirectly modify properties of the solvent and disrupt hydrogen bonds between water molecules to weaken the hydrophobic effect^{8,18}. Chaotropes are used to denature and emulsify proteins but they are unable to solubilize the lipid bilayer and thus are used in combination with detergents¹⁸. Detergents also prevent protein aggregation when proteins unfold and expose additional hydrophobic residues¹⁸.

In order to determine which detergents or combination of detergents, with or without chemical denaturants, are appropriate to include for cell lysis and protein solubilization sample preparation, we must consider physicochemical properties of the target molecule of interest and any downstream procedures. For example, if the goal is to isolate functional proteins following separation, then a nonionic detergent such as n-dodecyl- β -D-maltoside (DDM) can be used to preserve function¹⁹. It is possible to use a mixture of detergents to combine effects, but properties such as the CMC are more difficult to predict for mixtures⁹. Additionally, when purchasing commercial detergents, purity and consistency can vary. For example, digitonin is extracted from plants and purity can vary across lots and Triton X-100 consists of several different species of different polyethylene glycol headgroups which can vary⁹.

In Chapter 2, we investigate how on-chip sample preparation in our single-cell open microfluidic assay influences electromigration and separation performance compared to theoretical models based on expectations from separations with bulk (non-single cell) sample preparation. With bulk systems cell lysis is done off-chip and various protocols exist that have been optimized based on the protein target of choice and its location in the cell. However, with on-chip lysis and the short timescales used in our single-cell assay, we wanted to determine if our sample prep conditions were sufficient to detect a wide range of molecular mass protein targets. Then in Chapter 5 we investigate differential detergent fractionation buffer chemistries to measure subcellular expression of ER α isoforms.

1.3 Protein electrophoretic mobility in polyacrylamide gel electrophoresis

After appropriate sample preparation, proteins undergo electrophoretic separation. In polyacrylamide gel electrophoresis, an electric field is applied to first inject the protein sample into the polyacrylamide gel matrix and then proteins electromigrate through the polyacrylamide sieving matrix based on the physicochemical properties of the molecules.

The application of a voltage and thus electric field (E) provides the driving force for protein migration. With increasing voltage, the migration velocity (U) of the ions and molecules in the system also increase. The electrophoretic mobility (μ) characterizes the migration velocity of a molecule when an electric field is applied.

$$\mu = \frac{U}{E} \quad 1.1$$

In electrophoretic systems, the two main forces acting on protein and influencing migration are the drag force

$$F_d = 6\pi\nu a\vec{U} \quad 1.2$$

(where F_d is the total drag force, ν is the fluid kinematic viscosity, a is a measure of protein size, specifically the radius, and \vec{U} is the fluid velocity relative to the moving protein) and electric forces

$$F_E = q\vec{E} \quad 1.3$$

(where F_E is the total electrical force, q is the net charge of the protein and \vec{E} is the electric field). Balancing these equations, we can obtain electrophoretic mobility as

$$\mu = \frac{q}{6\pi\nu a} \quad 1.4$$

where the electrophoretic mobility is proportional to the protein net charge and inversely proportional to protein radius (or size). Using this relationship, we can analyze protein separations based on molecule mass and charge.

The use of sieving matrices such as polyacrylamide and agarose have long been adopted to aid in protein and nucleic acid separation. The Ferguson relationship²⁰

$$\log(\mu) = \log \mu_0 - K_r T \quad 1.5$$

is a log-linear equation that relates the electrophoretic mobility of a molecule in a sieving matrix (μ) based on it the electrophoretic mobility of a molecules in free solution (μ_0), a retardation coefficient (K_r) and the total acrylamide concentration (T). The retardation coefficient is a factor that relates properties of a molecule and how they may interact with the sieving matrix. Ferguson plots are generated by measuring the electrophoretic mobilities of protein targets in a series of different gel concentrations^{21,22} and have been utilized to elucidate information about protein size, conformation and net charge based on migration and separation performance. For size-based separations, the difference in transport rates between proteins of different sizes determines separation performance. However, for equilibrium electrophoresis methods, such as isoelectric focusing, gradients are established across the separation matrix and proteins electromigrated to the position where the protein is at equilibrium. For the work discussed in this dissertation, size-based separations utilizing SDS are the main focus.

For SDS-polyacrylamide gel electrophoresis (PAGE) size-based separations, we can make predictions on what Ferguson analysis should tell us. Because all proteins should have a normalized charge-to-mass ratio, they should all have the same mobility in free solution^{21,23}. On a Ferguson plot, this would manifest as all of the log-linear fit equations for each protein converging to the same y-intercept. Furthermore, in SDS-separations because protein molecules migrate solely due to molecular mass in the sieving matrix, the retardation coefficient (K_r) should scale linearly with molecular mass^{21,24}. For SDS-protein separations, an R plot of the retardation coefficients can be used as a calibration curve to determine the molecular mass of unknown protein species. To generate an R plot, the slope of the Ferguson linear equation of each protein is plotted against the known molecular mass of known standard protein targets. A linear fit is generated and can be used to determine the molecular mass of unknown protein targets based on their retardation coefficients. Using both the free-solution mobility and retardation coefficient determined using Ferguson analysis, it is possible to identify anomalously migrating SDS-protein complexes that do not behave as predicted²³.

However, to perform Ferguson analysis, experiments with multiple gel concentrations are necessary. For experiments with only one gel concentration, relative mobility can be used. To obtain relative mobility, the mobility of the molecular is normalized relative to that of a faster moving dye front, and the free-solution mobility is the mobility of the dye front²³. Alternatively, an empirical log-linear relationship between the molecular weight of a linearized protein molecule and migration distance has been established by Shapiro²⁵ for a single gel concentration. Unlike Ferguson analysis, this relationship assumes a normalized charge-to-mass ratio and is only applicable for a limited molecular weight range. Outside of the linear range, the relationship becomes sigmoidal²⁵. According to this relationship,

$$MW = k(10^{-bx}) \quad 1.6$$

where MW is the protein molecular mass (kDa), x is the protein migration distance in the gel, and b and k are empirically determined constants. An equation is determined

for a separation of known molecular weight ladder proteins in order to correctly identify and estimate the molecular weight of target or unknown protein species.

In Chapter 2 we utilize protein electromigration performance to scrutinize efficacy of protein solubilization in the preceding cell lysis step to identify shortcomings with the current on-chip lysis buffers. We identify an anomalously migrating protein based on its free-solution mobility and retardation coefficient. In Chapter 4, we utilize our understanding of protein electrophoretic mobility to develop models simulating protein elution from the gel onto a blotting membrane.

1.4 Detection of protein targets following electrophoretic separations

Following electrophoretic separation, in order to visualize protein targets, immobilization of the protein to preserve the separation is required for detection. In bulk (non-single cell) separations, separations are typically performed in the gel before being vertically electrotransferred to either porous nitrocellulose or polyvinylidene fluoride (PVDF) membranes which non-specifically adsorb protein through non-covalent hydrophobic interaction²⁶. In Chapter 4, we investigate an alternative geometry for the electrotransfer step, characterizing efficacy of transfer with microscale thin gels. After the electrotransfer, the membrane is incubated in a solution of target-specific probes that are able to bind to specific molecular targets of interest²⁷. Fluorescence or colorimetric detection is then used to visualize the probes and through specific binding, the target proteins. However, for scEPC, in order to minimize losses, the number of transfer steps and handling have been reduced. Instead, proteins are directly immobilized in the sieving polyacrylamide matrix through the activation of a benzophenone moiety^{6,7}. To functionalize polyacrylamide gels with benzophenone, a benzophenone methacrylamide (BPMA) functional group is incorporated in the gel precursor solution during gel fabrication to polymerize into the polyacrylamide gel matrix^{6,7}. Upon exposure to UV light (~350 nm) the benzophenone molecule is activated as a biradical that can form covalent bonds with protein by abstracting hydrogens from C-H bonds to form C-C bonds²⁸.

While benzophenone is critical for enabling scEPC, we hypothesize that it contributes to background fluorescence signal due to its chemical structure. We hypothesize that due to the double aromatic ring structure, benzophenone contributes to increased background fluorescence 1) due to autofluorescence from the conjugated double bonds that absorb and emit photons in the visible spectrum and 2) through non-specific hydrophobic interactions with fluorescent antibody probes that retain the probes in the gel even after wash steps. In Chapter 3, we explore an alternative photoactivatable molecule that can also covalently crosslink protein upon UV activation, diazirine.

Diazirine is commonly used in photolabeling and protein crosslinking and does not have the same aromatic structure as benzophenone. The chemical structure of diazirine consists of a three-membered ring comprised of two nitrogen atoms and one carbon atom. Diazirines have been used in a wide variety of crosslinking applications such as photolabeling²⁹, crosslinking protein into gel³⁰, adhesion for bioadhesives³¹, diazirine-

based chemical probes for histone readers and erasers³², and as a crosslinker for an elastin-like polymer³³. Upon UV activation, the diazirine ring breaks irreversibly releasing N₂ and forming a reactive carbene species that can insert into nearby C-H or heteroatom-H bonds to form a covalent bond^{29,34}. In contrast, UV-activation of benzophenone generates a diradical species that can react with nearby C-H bonds to form covalent bonds²⁸. The highly reactive carbene species has a shorter half-life, in the pico- to nano-second range, compared to the benzophenone diradical half-life of 120 μs³⁴. Furthermore, after activation, while any unbound benzophenone molecule is available for reactivation upon subsequent exposure to UV²⁸ carbenes can be quenched by the surrounding solvent, resulting in lower protein target crosslinking efficiency^{29,35}. Table 1-1 summarizes and compares the properties of the two molecules.

Table 1-1 Comparison of properties and attributes of benzophenone and diazirine as photoactivatable molecules for protein crosslinking

Benzophenone	Diazirine
<ul style="list-style-type: none"> • Activated by UV wavelengths (350-365 nm) • Converted to diradical • Reacts with neighboring C-H bonds • Can persist as long as 120 μs before relaxing back to original BP molecule • Repeated photoactivation to form diradicals – increased crosslinking efficiency • High affinity towards methionine 	<ul style="list-style-type: none"> • Activated by 350 - 360 nm wavelengths • Activation generates reactive carbene species via loss of N₂ • Inserts into neighboring C-H or heteroatom-H bonds • Carbene half-life is in the pico- to nanosecond range • Smaller molecular size, allowing incorporation closer to target active site • Carbenes can react with water resulting in decreased crosslinking efficiency

For protein crosslinking and photolabeling applications, diazirine has been previously reported reaction yields, ranging from 1-30% depending on any additional functional groups as well as the solvent in which the reaction took place^{36,37}. For example, UV-activation of 3-trifluoromethyl-3-phenyldiazirine in methanol yielded 95% of the activated carbene species inserting into O-H in methanol, but only 50% C-H insertion when activated in cyclohexane due to lower carbene reactivity with the solvent²⁹. When used for photolabeling, yields <10% are typical³⁵. While crosslinking efficiency of diazirine has been reported lower than benzophenone³⁵, the hydrophobic structure of benzophenone can limit the concentration that can be solubilized in the hydrogel precursor. We hypothesize that the less hydrophobic structure of diazirine will allow a higher concentration of diazirine methacrylate to be solubilized in the hydrogel precursor to improve in-gel protein capture. Thus, in Chapter 3 we explore efficacy of using diazirine to reduce background fluorescence signal and apply it to single-cell electrophoretic cytometry.

1.5 References

- (1) Aebersold, R.; Agar, J. N.; Amster, I. J.; Baker, M. S.; Bertozzi, C. R.; Boja, E. S.; Costello, C. E.; Cravatt, B. F.; Fenselau, C.; Garcia, B. A.; et al. How Many Human Proteoforms Are There? *Nat. Chem. Biol.* **2018**, *14* (3), 206–214. <https://doi.org/10.1038/nchembio.2576>.
- (2) Li, L.; Haynes, M. P.; Bender, J. R. Plasma Membrane Localization and Function of the Estrogen Receptor Alpha Variant (ER46) in Human Endothelial Cells. *Proc. Natl. Acad. Sci. U. S. A.* **2003**, *100* (8), 4807–4812. <https://doi.org/10.1073/pnas.0831079100>.
- (3) Klinge, C. M.; Riggs, K. A.; Wickramasinghe, N. S.; Emberts, C. G.; McConda, D. B.; Barry, P. N.; Magnusen, J. E. Estrogen Receptor Alpha 46 Is Reduced in Tamoxifen Resistant Breast Cancer Cells and Re-Expression Inhibits Cell Proliferation and Estrogen Receptor Alpha 66-Regulated Target Gene Transcription. *Mol. Cell. Endocrinol.* **2010**, *323* (2), 268–276. <https://doi.org/10.1016/j.mce.2010.03.013>.
- (4) Zhang, X.; Ding, L.; Kang, L.; Wang, Z.-Y. Estrogen Receptor-Alpha 36 Mediates Mitogenic Antiestrogen Signaling in ER-Negative Breast Cancer Cells. *PLoS One* **2012**, *7* (1), e30174. <https://doi.org/10.1371/journal.pone.0030174>.
- (5) Chen, J.-Q.; Russo, J. ERalpha-Negative and Triple Negative Breast Cancer: Molecular Features and Potential Therapeutic Approaches. *Biochim. Biophys. Acta* **2009**, *1796*, 162–175. <https://doi.org/10.1016/j.bbcan.2009.06.003>.
- (6) Hughes, A. J.; Spelke, D. P.; Xu, Z.; Kang, C.-C.; Schaffer, D. V.; Herr, A. E. Single-Cell Western Blotting. *Nat. Methods* **2014**, *11* (7), 749–755. <https://doi.org/10.1038/nmeth.2992>.
- (7) Kang, C.-C.; Yamauchi, K. A.; Vlassakis, J.; Sinkala, E.; Duncombe, T. A.; Herr, A. E. Single Cell-Resolution Western Blotting. *Nat. Protoc.* **2016**, *11* (8), 1508–1530. <https://doi.org/10.1038/nprot.2016.089>.
- (8) Rabilloud, T. Solubilization of Proteins for Electrophoretic Analyses. *Electrophoresis* **1996**, *17* (5), 813–829. <https://doi.org/10.1002/elps.1150170503>.
- (9) Linke, D. *Chapter 34 Detergents. An Overview*, 1st ed.; Elsevier Inc., 2009; Vol. 463. [https://doi.org/10.1016/S0076-6879\(09\)63034-2](https://doi.org/10.1016/S0076-6879(09)63034-2).
- (10) Seddon, A. M.; Curnow, P.; Booth, P. J. Membrane Proteins , Lipids and Detergents : Not Just a Soap Opera. **2004**, *1666*, 105–117. <https://doi.org/10.1016/j.bbamem.2004.04.011>.
- (11) Mooney, R. A. Use of Digitonin-Permeabilized Adipocytes for CAMP Studies. *Methods Enzymol.* **1988**, *159* (C), 193–202. [https://doi.org/10.1016/0076-6879\(88\)59020-1](https://doi.org/10.1016/0076-6879(88)59020-1).
- (12) Frenkel, N.; Makky, A.; Sudji, I. R.; Wink, M.; Tanaka, M. Mechanistic Investigation of Interactions between Steroidal Saponin Digitonin and Cell Membrane Models. *J. Phys. Chem. B* **2014**, *118* (50), 14632–14639. <https://doi.org/10.1021/jp5074939>.
- (13) Holden, P.; Horton, W. A. Crude Subcellular Fractionation of Cultured Mammalian Cell Lines. *BMC Res. Notes* **2009**, *2* (1), 243. <https://doi.org/10.1186/1756-0500-2-243>.
- (14) le Maire, M.; Champeil, P.; Möller, J. V. Interaction of Membrane Proteins and Lipids with Solubilizing Detergents. *Biochim. Biophys. Acta* **2000**, *1508*, 86–111.

- (15) Garavito, R. M.; Ferguson-Miller, S. Detergents as Tools in Membrane Biochemistry. *J. Biol. Chem.* **2001**, *276* (35), 32403–32406. <https://doi.org/10.1074/jbc.R100031200>.
- (16) Lichtenberg, D.; Ahyayauch, H.; Goñi, F. M. The Mechanism of Detergent Solubilization of Lipid Bilayers. *Biophys. J.* **2013**, *105* (2), 289–299. <https://doi.org/10.1016/j.bpj.2013.06.007>.
- (17) Kragh-hansen, U.; Maire, M.; Møller, J. V. Kragh-Hansen, Le Maire, Møller - 1998 - The Mechanism of Detergent Solubilization of Liposomes and Protein-Containing Membranes. *Biophys. J.* **1998**, *75* (March), 1–15.
- (18) Otzen, D. Protein – Surfactant Interactions: A Tale of Many States. *Biochim. Biophys. Acta* **2011**, *1814* (5), 562–591. <https://doi.org/10.1016/j.bbapap.2011.03.003>.
- (19) Huang, B.; Wu, H.; Bhaya, D.; Grossman, A.; Granier, S.; Kobilka, B. K.; Zare, R. N. Counting Low – Copy Number Proteins in a Single Cell. *Science* (80-.). **2007**, *315* (January), 81–85.
- (20) FERGUSON, K. A.; Lipsett, M. B.; Bell, P. H.; Cacciola, A. R.; Child, R. G.; Davies, M. C.; English, J. P.; Finn, B. M.; Meisenhelder, J. H.; Moyer, A. W.; et al. STARCH-GEL ELECTROPHORESIS--APPLICATION TO THE CLASSIFICATION OF PITUITARY PROTEINS AND POLYPEPTIDES. *Metabolism.* **1964**, *13* (10), SUPPL:985-1002. [https://doi.org/10.1016/S0026-0495\(64\)80018-4](https://doi.org/10.1016/S0026-0495(64)80018-4).
- (21) Rodbard, D.; Chrumbach, A. Unified Theory for Gel Electrophoresis and Gel Filtration. *Proc. Natl. Acad. Sci.* **1970**, *65* (4), 970–977. <https://doi.org/10.1073/pnas.65.4.970>.
- (22) Rodbard, D.; Chrumbach, A. Estimation of Molecular Radius, Free Mobility, and Valence Using Polyacrylamide Gel Electrophoresis. *Anal. Biochem.* **1971**, *40*, 95–134.
- (23) Westerhuis, W. H. J.; Sturgis, J. N.; Niederman, R. A. Reevaluation of the Electrophoretic Migration Behavior of Soluble Globular Proteins in the Native and Detergent-Denatured States in Polyacrylamide Gels. *Anal. Biochem.* **2000**, *284* (1), 143–152. <https://doi.org/10.1006/abio.2000.4684>.
- (24) Herr, A. E.; Singh, A. K. Photopolymerized Cross-Linked Polycrylamide Gels for on-Chip Protein Sizing. *Anal. Chem.* **2004**, *76* (16), 4727–4733. <https://doi.org/10.1021/ac049686u>.
- (25) Shapiro, A. L.; Vinuela, E.; Maizel Jr., J. V. Molecular Weight Estimation of Polypeptide Chains by Electrophoresis in SDS-Polyacrylamide Gels. *Biochem. Biophys. Res. Commun.* **1967**, *28* (5), 815–820.
- (26) Tonkinson, J. L.; Stillman, B. A. *NITROCELLULOSE: A TRIED AND TRUE POLYMER FINDS UTILITY AS A POST-GENOMIC SUBSTRATE*; 2002; Vol. 7.
- (27) *Protein Transfer Technical Handbook*; Thermo Fisher Scientific, 2015.
- (28) Dormán, G.; Nakamura, H.; Pulsipher, A.; Prestwich, G. D. The Life of Pi Star: Exploring the Exciting and Forbidden Worlds of the Benzophenone Photophore. *Chem. Rev.* **2016**, *116* (24), 15284–15398. <https://doi.org/10.1021/acs.chemrev.6b00342>.
- (29) Brunner, J.; Senn, H.; Richards, F. M. 3-Trifluoromethyl-3-Phenyldiazirine. A New Carbene Generating Group for Photolabeling Reagents. *J. Biol. Chem.* **1980**, *255*

- (8), 3313–3318. [https://doi.org/10.1016/s0021-9258\(19\)85701-0](https://doi.org/10.1016/s0021-9258(19)85701-0).
- (30) Wang, Y.; Delgado-Fukushima, E.; Fu, R. X.; Doerk, G. S.; Monclare, J. K. Controlling Drug Absorption, Release, and Erosion of Photopatterned Protein Engineered Hydrogels. *Biomacromolecules* **2020**, *21* (9), 3608–3619. <https://doi.org/10.1021/acs.biomac.0c00616>.
- (31) Nanda, H. S.; Shah, A. H.; Wicaksono, G.; Pokholenko, O.; Gao, F.; Djordjevic, I.; Steele, T. W. J. Nonthrombogenic Hydrogel Coatings with Carbene-Cross-Linking Bioadhesives. *Biomacromolecules* **2018**, *19* (5), 1425–1434. <https://doi.org/10.1021/acs.biomac.8b00074>.
- (32) Yang, T.; Liu, Z.; Li, X. D. Developing Diazirine-Based Chemical Probes to Identify Histone Modification “readers” and “Erasers.” *Chem. Sci.* **2015**, *6* (2), 1011–1017. <https://doi.org/10.1039/c4sc02328e>.
- (33) Raphael, J.; Parisi-Amon, A.; Heilshorn, S. C. Photoreactive Elastin-like Proteins for Use as Versatile Bioactive Materials and Surface Coatings. *J. Mater. Chem.* **2012**, *22* (37), 19429–19437. <https://doi.org/10.1039/c2jm31768k>.
- (34) Tanaka, Y.; Bond, M. R.; Kohler, J. J. Photocrosslinkers Illuminate Interactions in Living Cells. *Mol. Biosyst.* **2008**, *4* (6), 473–480. <https://doi.org/10.1039/b803218a>.
- (35) A. Fleming, S. Chemical Reagents in Photoaffinity Labeling. *Tetrahedron* **1995**, *51* (46), 12479–12520. [https://doi.org/10.1016/0040-4020\(95\)00598-3](https://doi.org/10.1016/0040-4020(95)00598-3).
- (36) Hill, J. R.; Robertson, A. A. B. Fishing for Drug Targets: A Focus on Diazirine Photoaffinity Probe Synthesis. *J. Med. Chem.* **2018**, *61* (16), 6945–6963. <https://doi.org/10.1021/acs.jmedchem.7b01561>.
- (37) Wang, J.; Kubicki, J.; Peng, H.; Platz, M. S. Influence of Solvent on Carbene Intersystem Crossing Rates. *J. Am. Chem. Soc.* **2008**, *130* (20), 6604–6609. <https://doi.org/10.1021/ja711385t>.

Chapter 2: Ferguson analysis of protein electromigration during single-cell electrophoresis in an open microfluidic device

Adapted with permission from K.Y. Tan and A.E. Herr, “Ferguson analysis of protein electromigration during single-cell electrophoresis in an open microfluidic device”, *Analyst*, 2020

2.1 Introduction

In contrast to ‘enclosed’ microfluidic systems that utilize microchannel networks and pneumatic control of fluid flow, open microfluidic systems are emerging as an alternative format that is scalable, compatible with standard wet laboratory handling processes, and integrates with straightforward fluidic interfacing. Diverse lines of inquiry have benefitted from open microfluidic formats including the study of differentiating cells¹, secreted proteins^{2,3}, nucleic acids⁴, and single-cell electrophoresis to study DNA damage⁵, protein expression^{6–8}, and protein sub-cellular localization^{9,10}. These single-cell electrophoresis assays involve incorporating multiple steps, from cell capture to in-gel detection, on a single substrate, usually a hydrogel matrix^{5,6}. The hydrogel serves as a sieving matrix to differentiate molecules based on migration through the gel enabling identification and quantification of specific molecules of interest.

For protein electrophoresis, electromigration of proteins denatured by sodium dodecyl sulfate (SDS) can be described by an empirical relationship determined by Shapiro et al.¹¹. Under these conditions, the protein electromigration distance varies linearly with the log value of protein molecular mass, across a series of uniform gel concentrations^{6,8,11–13}. However, the Shapiro et al. relationship is only valid for a limited range of molecular masses at a given gel concentration; outside of the observed linear range, the relationship is sigmoidal^{11,14,15}. Furthermore, the analysis assumes that SDS linearizes protein structure and binds to the protein at a constant ratio of 1.4g of SDS per gram of protein. Under these conditions, most proteins are linearized with similar charge-to-mass-ratios and thus, protein size is solely a function of molecular mass^{16,17}.

Ferguson analysis is used to assess the electrophoretic mobility, rather than migration, of proteins during electrophoresis. This analysis can verify if the assumptions required for the Shapiro analysis are met. According to the Ferguson relation (Equation 2.1)

$$\log(\mu) = \log \mu_0 - K_r T \quad 2.1$$

where μ (cm²/V·s) is the protein electrophoretic mobility, μ_0 is the protein electrophoretic mobility in free solution, K_r is the retardation coefficient and T is the total acrylamide concentration (%T)^{18,19}, the relationship between protein mobility and gel concentration is log-linear¹⁸. Combined with Ogston’s model for molecular sieving through polymer matrices (which assumes that gel fiber properties do not vary with gel concentration and that the migrating species does not interact with the gel fibers)²⁰, Ferguson plots are generated by measuring the electrophoretic mobilities of protein targets in a set of gels, each comprised of a different gel concentration^{19,21}.

Ferguson analyses underpins creation of calibration curves for determining K_r , and hence molecular mass, of each protein target. K_r is related to the size and shape of the migrating protein and the sieving ability of the separation medium^{19,22}. Based on these assumptions, proteins migrate solely based on size in SDS-polyacrylamide gel electrophoresis (SDS-PAGE)¹⁷. Concomitantly, Ferguson analysis can identify anomalously migrating SDS-denatured proteins, which are observed when SDS is unable to bind as expected due to unusual charge²³, conformation^{15,24}, or chemical properties (i.e. glycoproteins with carbohydrate constituents^{25,26} or unreduced sulfhydryl groups²⁷)²⁸ or when alternate sample preparation conditions are utilized.

In addition to SDS-denaturing protein PAGE, researchers have scrutinized other protein preparation chemistries; both for the fundamental electromigration implications and for the utility in protein analysis. Non-denaturing buffers enable separations based on native protein conformation and charge, which is useful for isolation of functional proteins after separations. In equilibrium electrophoresis (i.e., isoelectric focusing, IEF; temperature gradient focusing, TGF), buffers are carefully designed to create a gradient in a key property under an applied electric field, causing proteins to electromigrate to the position where the protein has no net force. In IEF, buffers are designed to preserve protein native charge to facilitate migration along a gradient in pH, thus allowing identification of the isoelectric point (pI) of a protein at the location in the pH gradient where the protein focuses²⁹. In native PAGE, proteins migrate according to the net charge, size, and shape of the protein molecule. In Blue Native PAGE, proteins are treated with Coomassie blue stain which confers the necessary negative charge for electromigration without denaturing protein structure, thus allowing migration based on molecular mass while still preserving a functional protein³⁰. Taken together, the reagents used in both protein sample preparation and during electrophoresis (in its various forms) exert a substantial influence on the physicochemical property measured.

Use of open microwells for cell lysis and protein preparation prior to protein PAGE of single-cell lysates informs design of alternate, dual functionality buffers that combine lysis and electrophoresis functions into a single reagent^{6,31}. Bifunctional and multifunctional buffers reduce needed fluid handling in the open single-cell protein PAGE devices. The open microwell arrays used for cell isolation and sample preparation are fabricated in a thin (~45 μm) polyacrylamide (PA) gel layered on a glass microscope slide. The diameter of each microwell is sized to house an individual cell of each cell type to be assayed³¹. Owing to the open format, the bifunctional lysis and electrophoresis run buffer contains ionic detergents to lyse cells and denature proteins and is applied synchronously to the entire array of cells. Both cell lysis and protein solubilization have been designed to be as fast as possible^{6,7}. To achieve this action, the composition of the buffer must balance protein solubility with electrophoretic performance. Higher concentrations of ionic detergents may improve cell lysis and protein solubilization, but can increase buffer conductivity, concomitantly increase Joule heating and protein loss due to diffusion³². Given the open microfluidic design and unique bifunctional buffer system, we hypothesize that the sample preparation (cell lysis, protein solubilization, and denaturation) affects the downstream protein PAGE separation.

Consequently, we first sought to apply the analysis of Shapiro et al. to understand the relationship between electromigration and molecular mass, across three different gel concentrations. We then performed Ferguson analysis to validate electrophoretic mobility of endogenous proteins across the different gel densities in the open microfluidic device. Finally, we analyzed the impact of the gel concentration, and thus gel matrix pore size, on measurements from our in-gel immunoassay.

2.2 Materials and Methods

Reagents

30%T, 3.3%C acrylamide/bis-acrylamide (29:1) (A3574, Sigma), ammonium persulfate (APS, A3678), and tetramethyl- ethylenediamine (TEMED, T9281) for gel polymerization, dichlorodimethylsilane (440272) and 3-(trimethoxysilyl)propyl methacrylate (440159) for wafer and glass silanization, respectively, bovine serum albumin (BSA, A7638), fetal bovine serum (FBS, F2442) and urea (U5378) were purchased from Sigma-Aldrich. Triton X-100 (BP-151), phosphate buffered saline (PBS, 10010023), RPMI 1640 medium (11875), penicillin–streptomycin (15070063) were purchased from Thermo Fisher Scientific. 1.5 M Tris-HCl, pH 8.8 (T1588) was purchased from Teknova, 10x tris-glycine buffer (1610734) was purchased from Biorad, and 10x Tris buffered saline with Tween 20 (TBST, 9997S) was purchased from Cell Signaling Technologies. Deionized water (18.2 M Ω) was obtained using an Ultrapure water system from Millipore. N-[3-[(3-Benzoylphenyl)formamido]propyl] methacrylamide (BPMAC) was custom synthesized by PharmAgra Laboratories^{6,7}.

Antibodies.

The primary protein antibodies to GAPDH (goat pAb; SAB2500450, Sigma), β -tubulin (rabbit pAb; ab6046, Abcam), α -Actinin (rabbit mAb, 6487S, Cell Signaling Technology), ER- α (rabbit mAb; RM9101S, Thermo Fisher Scientific), and mTOR (rabbit,2983S, Cell Signaling Technologies) were used. Secondary antibodies to goat IgG prelabelled with Alexa Fluor 647 (A21447), rabbit IgG pre-labelled with Alexa Fluor 555 or 647 (A31572 and A31573) were purchased from Invitrogen. All primary antibodies were used at a 1:10 dilution in 2% TBST/BSA from stock concentrations and incubated for 2 hours at room temperature, except for anti-GAPDH and anti-ER- α , which were incubated for 3 hours at room temperature. Secondary antibodies were diluted to a 1:20 working concentration in 2% TBST/BSA from stock and incubated for 1 hour at room temperature, protected from light.

SU8 and PA gel fabrication.

SU8 fabrication to generate the master and PA gel fabrication were performed as described previously^{6,31}. 5%T, 6%T, and 8%T PA gels were fabricated to all have microwell diameter and depth of 30 μ m and 45 μ m respectively on wafers (WaferPro C04009) microfabricated with SU-8 3050 photoresist (Kayaku Advanced Materials

Y311075) and coated with dichlorodimethylsilane. All PA gels on the single-cell PAGE slides were chemically polymerized with 0.08% APS and 0.08% TEMED.

Cell lines and cell harvesting.

MCF-7 cells were obtained from the American Type Culture Collection (ATCC) and authenticated (Promega). The MCF-7 cell line was maintained in RPMI 1640 supplemented with 1% penicillin/streptomycin and 10% FBS. Cells were kept in a 37 °C incubator at 5% CO₂. For single-cell PAGE, cells were harvested using a cell scraper (Falcon, 353085), and resuspended in 4 °C 1X PBS at a concentration of ~10⁶ cells per mL.

Single-cell PAGE.

Single-cell PAGE was performed as described previously^{6,31}. Briefly, cells were pipetted over the PA gel and settled by gravity into the microwells patterned in the PA gel. Lysis buffer heated in a water bath to 55 °C was poured over the PA gel in order to lyse the cells in the microwells for 30 seconds. An electric field ($E = 40$ V/cm) was applied to inject and separate proteins for 30 seconds in the PA gel abutting the microwell. After separation, proteins were immobilized to the gel matrix via a 45 second exposure to UV (Lightningcure LC5, Hamamatsu) which activated the benzophenone methacrylamide cross-linked into the PA gel to immobilize proteins in the gel matrix^{6,31}. Immobilized proteins were probed in-gel by diffusing fluorescently labelled antibody probes into the PA. A fluorescence microarray scanner (Genepix 4300A, Molecular Devices) equipped with 4-laser lines ($\lambda = 488, 532, 594, 635$) acquired fluorescence readout. Subsequent rounds of antibody stripping were performed over the course of 9 months following the protocols for multiplexed protein analysis, as detailed previously^{6,31}. Because all proteins from a single-cell are sieved in the gel matrix simultaneously and subsequently immobilized in-gel, additional targets can be immunoprobed months after the separation is performed. Previous work has demonstrated the long-term stability of single-cell PAGE slides demonstrating the ability to detect protein after 4 months of storage and the ability to strip immunoprobed protein signal after 7 months of storage⁷.

Chemical Stripping and Reprobing.

Harsh stripping buffer was made with 62.5 mM Tris-HCl (pH 6.8), 2% SDS, and 0.8% β -mercaptoethanol. Wash buffer consisted of 1x TBST. Gels were incubated in stripping buffer at 55–57 °C for ≥ 1 hr. Gels were subsequently washed in 1x TBST for ≥ 1 hr, before the next round of immunoprobing.

Immunoblot signal quantification and statistical analysis.

The images were first processed in Fiji^{33,34} by applying a median filter using the “Remove Outliers” macro with a 2-pixel radius and a threshold value of 50 AFU to remove punctate noise. Then quantification of fluorescence signal from immunoblots was processed by in-house scripts written in MATLAB (R2018b) as previously

described³¹. Gaussian curves were fit to fluorescence intensity profiles in MATLAB (R2018b, Curve Fitting Toolbox) in order to obtain the mean μ (used to describe the protein migration distance) and the variance σ^2 (used to calculate peak width as 4σ). Area-under-the-curve (AUC) analysis of the intensity profiles was performed to quantify immunoblot signal 4σ from the fitted-curve peak location. The signal-to-noise ratio was calculated by taking the peak value of the Gaussian fit curve and dividing by the standard deviation of the background region from the 4σ region surrounding the peak. Only protein peaks with $\text{SNR} \geq 3$ were included in downstream quantification of AUC and σ comparisons. Plots and statistical tests were generated and performed with R (version 3.6.1).

Ferguson Analysis

To generate the Ferguson plots (Figure 2-3), first the average velocity for each protein band was calculated by dividing the migration distance of the protein peak by the electrophoresis time of 30 seconds. Mobility (μ) was then calculated by dividing the average velocity by the applied electric field of 40 V/cm. The final plot was produced by plotting the logarithm (base 10) of the mobility against gel concentration and fitting a linear relationship for each protein. The slope of the linear fit is the retardation coefficient, K_r , for each protein.

Calculation for percent of protein peaks that pass quality control metric $\text{SNR} \geq 3$

To compare the percentage of detected protein peaks that can be analyzed ($\text{SNR} \geq 3$), the percentage of detected protein peaks that pass all quality control steps was calculated. The in-house MATLAB (R2018b) scripts used to quantify fluorescence signal from immunoblots identifies all the peaks that are detected and pass initial QC (Gaussian fit R^2 -value ≥ 0.7 and visual inspection). Further screening is then performed to only accept intensity profiles containing peaks with $\text{SNR} \geq 3$ (the numerator). The percent of peaks with an $\text{SNR} \geq 3$ was calculated using Equation 2.2:

$$\text{Percent that Pass } \text{SNR} \geq 3 = \frac{\text{Peaks with } \text{SNR} \geq 3}{\text{All Peaks that Pass QC } (R^2 \geq 0.7 \text{ and visual})} \quad 2.2$$

for each replicate device across all protein targets for the highest and lowest gel concentration

The mean and standard deviation of the three replicate devices is plotted to show that in general, we are able to recover a higher percent of detected peaks for the 8%T gel condition across all five protein targets. However, with a small n we cannot make significant conclusions.

2.3 Results and Discussion

Linearity of log-linear relationship between molecular mass and protein migration distance is sensitive to gel concentration

We assessed the electrophoretic mobility of proteins from single cells that were lysed on-chip and separated based on molecular mass. The bifunctional buffer used here contains SDS, sodium deoxycholate, 8M urea and is heated to 55 °C. Urea aids protein denaturation by breaking noncovalent bonds that hold protein structures together enabling the unfolding of protein such that SDS is able to fully bind to all protein residues³⁵. Furthermore, heating the lysis buffer is known to enhance protein solubilization leading to improved electrophoretic injection and separation resolution⁷.

We performed Ferguson analysis of the nine protein targets: GAPDH (36 kDa), β – tubulin (50 kDa), PTBP1 (57 kDa), ER- α (66 kDa), HSP90 (90 kDa), SFPQ (95 kDa), α -Actinin (103 kDa), Vinculin (124 kDa), and mTOR (289 kDa) as are relevant to single-cell analysis of breast cancer cells (MCF-7). (SFPQ has a reported molecular mass of 76 kDa, however based on migration distance, the manufacturer's product information page, and previously reported western blot analysis from bulk cell lysate, we hypothesize detection of a higher molecular mass species of ~95 kDa^{36–40}.) SDS-PAGE was performed in 1.5-mm separation lengths for three gel concentrations (5, 6, and 8%T) across 3 replicate devices for each gel concentration. Aggregating the single-cell data point taken from the 3 replicate devices for each condition, we measured the relationships $y_{5\%T}=2876-1109x$ ($R^2 = 0.93$), $y_{6\%T}=2552-1017x$ ($R^2 = 0.85$), and $y_{8\%T}=2100-908x$ ($R^2 = 0.84$) (Figure 2-1, dashed lines). As the gel concentration increased, we observed reduced R^2 values, indicating decreasing accuracy of the linear-fit model. This trend suggests that the smaller pore-size gels (8%T) are less suitable for separating a wide range of molecular mass protein targets due to the smaller pore size limiting the injection and mobility of higher molecular mass proteins.

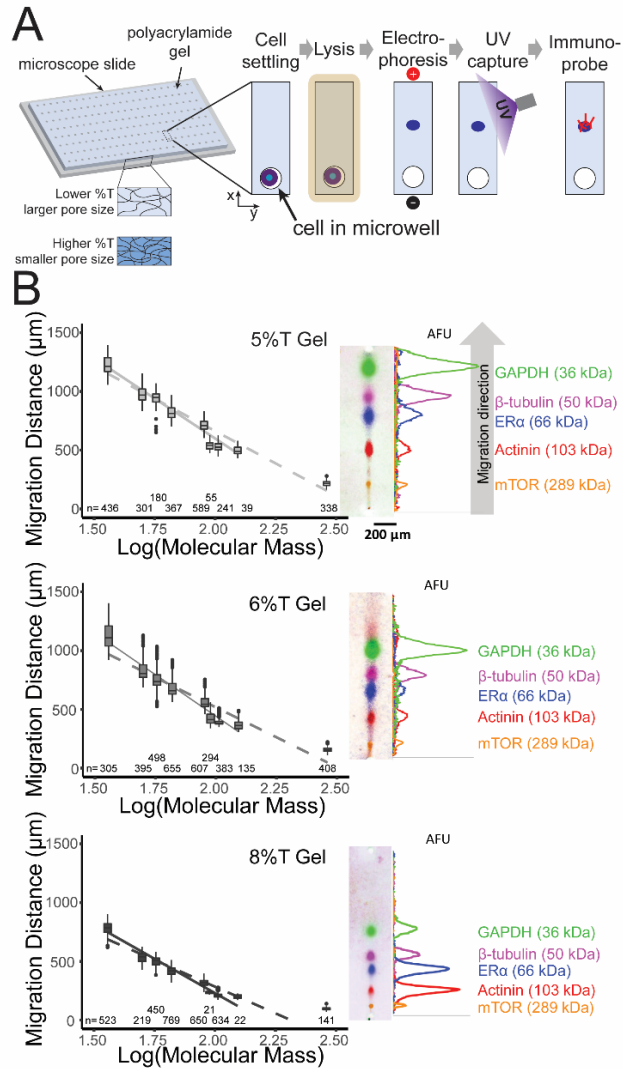


Figure 2-1: Dependence of migration distance on protein molecular mass in three different gel compositions.

A) Open microfluidic device for single-cell PAGE immunoassay. Single-cells are gravity settled into an array of microwells for subsequent cell lysis and protein solubilization, protein PAGE, and in-gel immobilization of separated proteins. Protein targets are immunoprobed with fluorophore-conjugated antibodies. B) (Left) Relationship between electromigration distance and the logarithm value (base 10) of molecular mass of nine different protein targets (GAPDH, 36 kDa; β -tubulin, 50 kDa; PTBP1, 57 kDa (above limit of detection in 6/9 gels tested); ER- α , 66 kDa; HSP90, 90 kDa; SFPQ, 95 kDa; α -Actinin, 103 kDa; Vinculin, 124 kDa; and mTOR, 289 kDa) from lysed MCF-7 cells. Three different gel composition conditions (5%T, 6%T and 8%T) were used to analyze the differing electrophoretic migration distances. Boxplots represent aggregation of single-cell data points taken from 3 replicate devices with the number of individual cells assayed at the bottom of each plot. Dashed lines (---) represent linear fits including mTOR, while solid lines (—) indicate fits excluding mTOR. (Right) Representative false-color fluorescence micrographs and intensity plots as examples of protein electromigration in each gel condition. (See Figure 2-2 for additional targets)

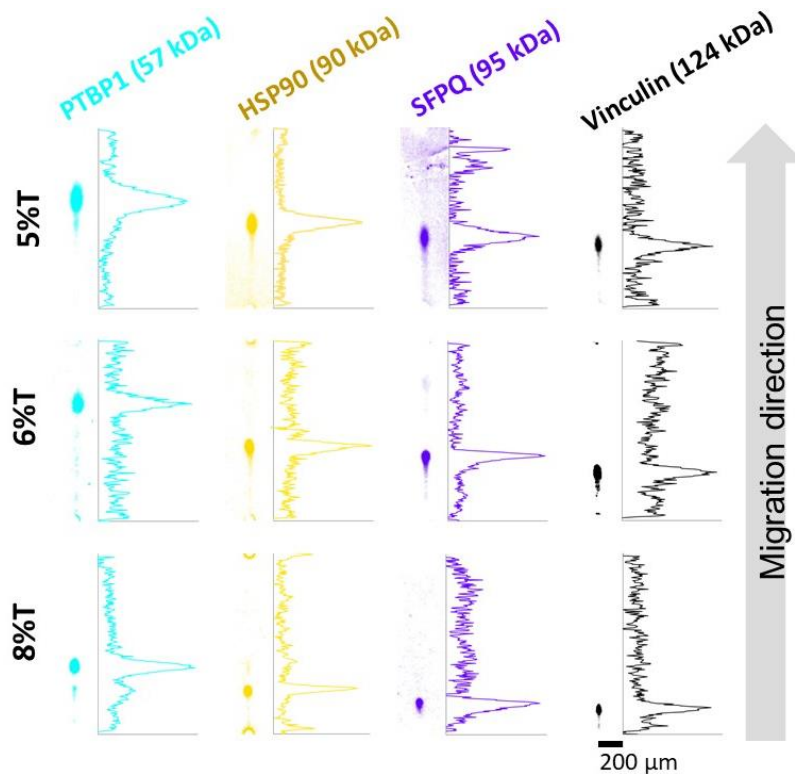


Figure 2-2: Additional false-color fluorescence micrographs and intensity plots of electromigration for PTBP1, HSP90, SFPQ, and Vinculin protein targets.

False-color fluorescence micrographs and corresponding intensity plots of additional protein targets: PTBP1 (57 kDa, above limit of detection in 6/9 gels tested), HSP90 (90 kDa), SFPQ (95 kDa), and Vinculin (124 kDa) from lysed MCF-7 cells assayed in all three gel conditions (5%, 6%, and 8%T).

Previous studies have reported that the expected linear relationship holds true for a sub-set of protein masses as determined by the design of the sizing assay (e.g., gel pore size, lysis buffer and run buffer compositions). Shapiro et al. originally demonstrated linearity for proteins ranging from 15 – 165 kDa in molecular mass in 5%T gels¹¹. When Weber et al. measured protein mobility for polypeptide chains up to 200 kDa, they obtained a hyperbolic curve in 10%T gels but had used half the amount of normal crosslinker concentration¹⁴. Dunker et al. obtained linearity for the following conditions: 10 – 60 kDa for 15%T gels, 10 – 100 kDa for 10%T gels and 20 – 350 kDa for 5%T gels, using 3.3% crosslinker in all gel conditions⁴¹. Westerhuis et al. later re-evaluated performance across multiple gel concentrations and performed Ferguson analysis, and reported for < 15%T gels, there was “ideal migration” of SDS-protein complexes when protein targets were between 14 – 65 kDa but there was some nonlinearity observed for larger proteins (>65 kDa)¹⁵. Other studies characterizing protein electrophoretic mobility and utilizing the linear relationship put forth by Shapiro et al. have limited analysis to proteins with molecular masses < 200 kDa^{28,42–44}. In order to separate higher-molecular mass proteins, ranging from 220 – 4000 kDa, Warren et al. developed a vertical agarose gel electrophoresis system, taking advantage of the larger pore sizes in agarose gels⁴⁵.

Here, we sized 9 protein targets ranging in molecular mass from 36-289 kDa. Corroborating the findings of the literature reviewed in the previous paragraph, we observed appreciable linearity over the 36 – 289 kDa range, across all 3 pore-size gels scrutinized using linear-fit models to calculate the predicted molecular mass of each target (Table 2-1).

Table 2-1. Predicted Size of mTOR from Migration Distance

%T Gel	mTOR Predicted Molecular Mass (kDa)	% Deviation
5%	250.0	13.5
6%	227.3	21.4
8%	160.5	44.5

Also, in line with the reports outlined, we scrutinized the median migration distance for the largest protein target (mTOR, 289 kDa) and found good agreement for the largest pore size gel (< 14% deviation). Corroborating the work of Neville and others, we observed a larger (>44%) deviation between expected and measured molecular mass for this large mass target for the smallest pore size gel (8%T)^{14,15,46,47}. When considering the linear relationship between electromigration distance and the logarithm value of molecular mass with mTOR removed from consideration, the 8 protein targets assayed yielded the relationships to be $y_{5\%T}=3327-1364x$ ($R^2 = 0.92$), $y_{6\%T}=3269-1413x$ ($R^2 = 0.86$), and $y_{8\%T}=2566-1168x$ ($R^2 = 0.94$) (Figure 2-1, solid lines) and all three gel compositions had R^2 values ≥ 0.86 .

Ferguson analysis of protein molecular mass standards from single-cell lysate

To further scrutinize electromigration of endogenous protein targets from single-cell lysate, we performed Ferguson analysis (Figure 2-3A) to validate the assumptions for SDS-protein complex migration in our system. Because Ferguson analysis does not rely on the assumption that protein surface charge density is uniform across all molecules, it can be performed on native and denatured proteins to elucidate information about the size, shape and net charge of the migrating protein¹⁹.

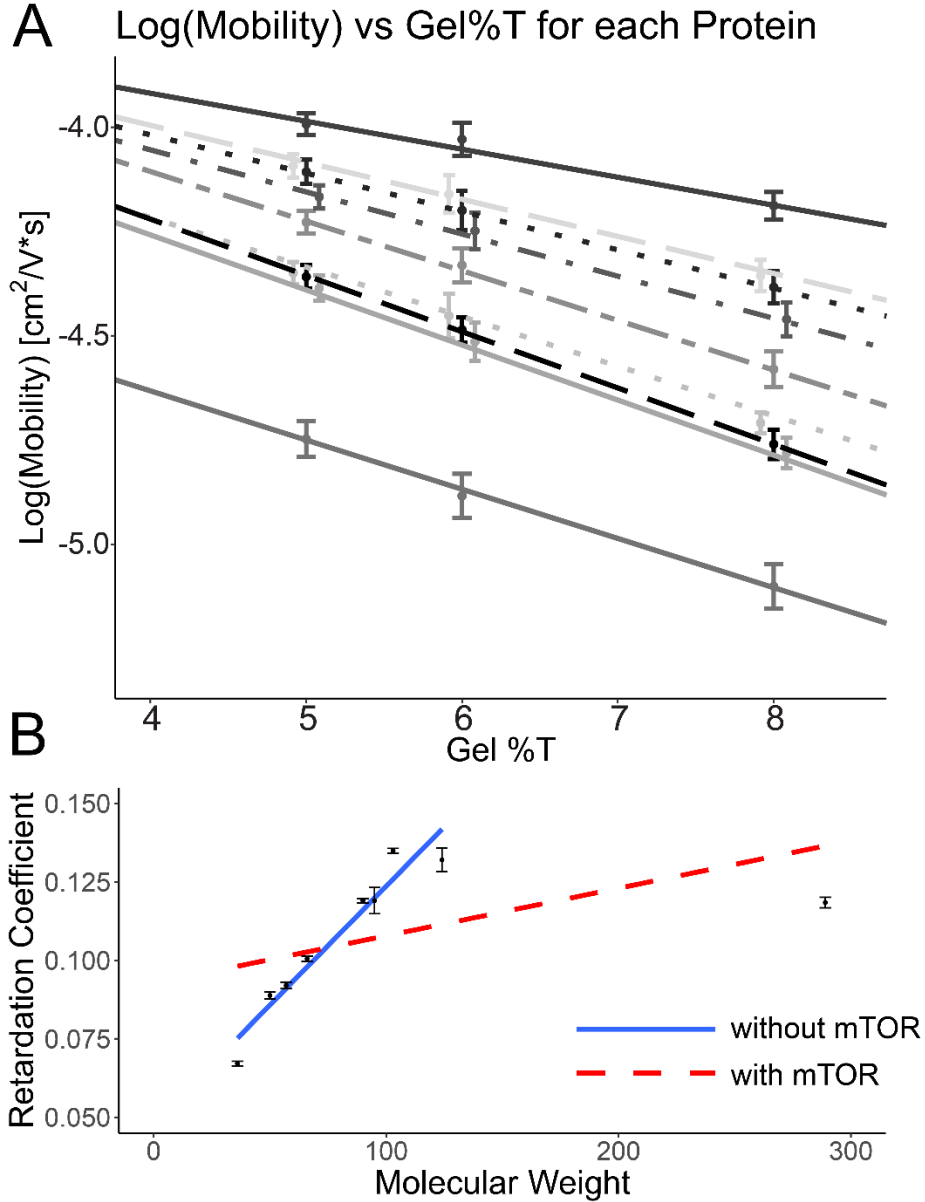


Figure 2-3. Ferguson and calibration plots for 5 protein targets detected from single cells that were lysed on-chip.

A) Ferguson plot of the logarithm value of the mobility vs gel concentration for each protein target. Ferguson plot equations: $y_{\text{GAPDH}} = -3.65 - 0.067x$ ($R^2 = 0.87$), $y_{\beta\text{-tubulin}} = -3.64 - 0.089x$ ($R^2 = 0.86$), $y_{\text{PTBP1}} = -3.65 - 0.092x$ ($R^2 = 0.87$), $y_{\text{ER-}\alpha} = -3.65 - 0.101x$ ($R^2 = 0.90$), $y_{\text{HSP90}} = -3.63 - 0.119x$ ($R^2 = 0.94$), $y_{\text{SFPQ}} = -3.74 - 0.119x$ ($R^2 = 0.69$), $y_{\alpha\text{-Actinin}} = -3.68 - 0.135x$ ($R^2 = 0.96$), $y_{\text{Vinculin}} = -3.73 - 0.132x$ ($R^2 = 0.87$), and $y_{\text{mTOR}} = -4.16 - 0.118x$ ($R^2 = 0.85$). B) Plot of the retardation coefficient (K_r , the slope of the linear fits from the Ferguson plot), vs the protein molecular mass. The calibration curve from all nine protein targets (dashed line) is described by the equation $y = (1.5 \times 10^{-4})x + 0.093$ ($R^2 = 0.26$). The equation for the calibration curve excluding mTOR (solid line) $y = (7.6 \times 10^{-4})x + 0.048$ ($R^2 = 0.93$).

Because our bifunctional lysis and electrophoresis run buffer contained 1% SDS with 8M urea to denature the native protein structure and normalize the overall protein charge-to-mass ratio, we expect K_r to depend only on the molecular size. Thus, K_r should increase linearly with protein molecular mass. Using the linear relationship

between K_r and molecular mass, we can generate a calibration curve to predict molecular mass of unknown protein targets based on their K_r (Figure 2-3B)¹⁷.

By extrapolating the y-intercept from the Ferguson plot, we determine if mobility is solely a function of molecular mass. The y-intercept corresponds to the electrophoretic mobility in free solution (μ_0 ; without a sieving matrix) of each SDS-protein complex¹⁹. Under SDS-denaturing conditions, all proteins should have the same μ_0 . We observe that eight of the targets (GAPDH, β -tubulin, PTBP1, ER α , HSP90, SFPQ, α -Actinin, and Vinculin) have similar y-intercepts (Table 2-2). For the largest molecular mass protein considered, mTOR (289 kDa), we note that the lower than expected y-intercept yields a calculated K_r that is lower than the K_r for α -Actinin (103 kDa) (Figure 2-3B). Compared to Ferguson analysis of mTOR electromigration data from single-cell protein PAGE previously published from our group using similar assay conditions (e.g. lysis buffer and gel pore sizes), we observe the same trend of a lower than expected y-intercept value and K_r for mTOR relative to the other smaller-molecular mass proteins assayed¹².

Table 2-2. Extrapolated y-intercepts (free solution mobility) from Ferguson Plot

Protein	Molecular mass (kDa)	Free-solution mobility ($\text{cm}^2/\text{V}\cdot\text{s}$) (y-intercept)
GAPDH	36	-3.65
β -tubulin	50	-3.64
PTBP1	57	-3.65
ER- α	66	-3.65
HSP90	90	-3.63
SFPQ	95	-3.74
α -Actinin	103	-3.68
Vinculin	124	-3.73
mTOR	289	-4.16

As a corollary, we make two observations regarding the largest molecular mass protein analyzed here. First, the lower than predicted K_r suggests that (given the low lysis duration) mTOR may partially retain its native conformation, preventing SDS from binding uniformly along the protein^{15,48,49}. SDS-denatured proteins have higher K_r values than native proteins due to size¹⁵. Second, despite mTOR's lower K_r value, mTOR did not migrate as far into the gel as α -Actinin and Vinculin (Figure 2-1, Figure 2-2), especially in the small gel pore-size condition, again suggesting potentially incomplete solubilization. As a result of incomplete solubilization and linearization during the on-chip cell lysis step, molecular properties (e.g., charge, hydrophobicity) are expected to affect how the molecule interacts with the PA gel matrix and thus how well the protein injects and migrates. We conclude that the assay conditions developed here are not suitable for the largest molecular mass species, and omit mTOR from further development of this assay, and consider in the future with a sizing assay suited for large molecular mass species. The resulting calibration curve between K_r and the molecular masses of the other 8 protein targets, yields a linear relationship $y = (7.6 \times 10^{-4})x + 0.048$ ($R^2 = 0.93$) ($n = 3$ replicate devices) as expected for separations based on size alone.

Determining size-exclusion limit for different gel concentrations

We next used μ_0 to plot the logarithm of molecular mass against normalized mobility (μ/μ_0) in each gel concentration (Figure 2-4). From this linear relationship, we can determine the size-exclusion limit of each gel composition by calculating the molecular mass that has zero mobility (the y-axis intercept). An understanding of limitations for different gel concentrations is necessary to design optimal assay parameters for single-cell PAGE, based on the protein targets of interest. Based on the preceding analysis, mTOR was excluded from the analysis to determine the size-exclusion limits.

The resulting linear fits between the logarithm of molecular mass and (μ/μ_0) had $R^2 \geq 0.84$ for all gel concentrations (Figure 2-4). From these models, we predict the size-exclusion limits listed in Table 2-3.

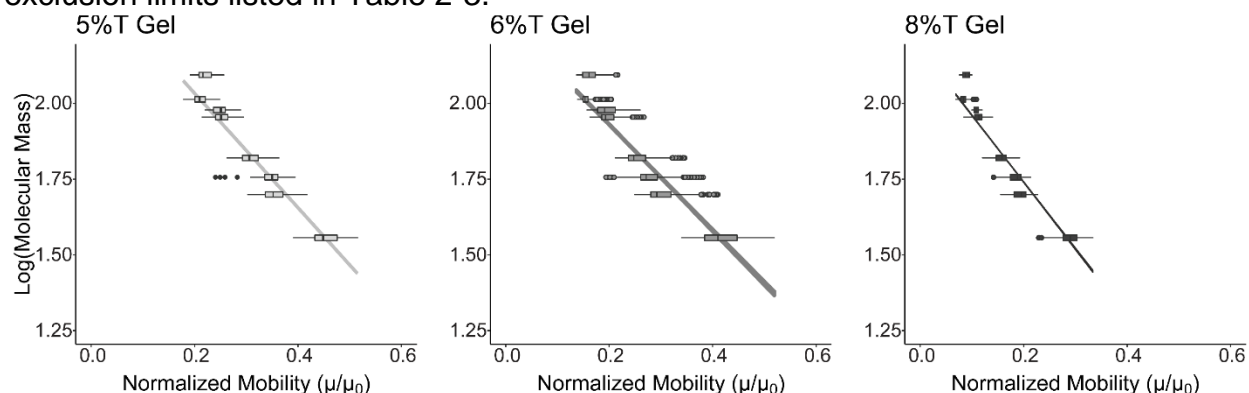


Figure 2-4. Standard curves of logarithmic molecular mass vs normalized migration for single-cell SDS-PAGE in an open microfluidic device.

Standard curves are shown for 5, 6, and 8%T gels and 8 different protein targets (GAPDH, 36 kDa; β -tubulin, 50 kDa; PTBP1, 57 kDa; ER- α , 66 kDa; HSP90, 90 kDa; SFPQ, 95 kDa; α -Actinin, 103 kDa; and Vinculin, 124 kDa, excluding mTOR). Calibration equations: $y_{5\%T} = 2.41 - 1.89x$ ($R^2 = 0.92$), $y_{6\%T} = 2.28 - 1.75x$ ($R^2 = 0.84$), and $y_{8\%T} = 2.18 - 2.20x$ ($R^2 = 0.93$).

Table 2-3. Predicted Size-Exclusion limits

%T	y-intercept	Molecular mass (kDa)
5	2.41	257.0
6	2.28	190.5
8	2.18	151.4

In addition to protein migration performance in different gel concentrations, we also sought to evaluate how – as pore size decreases (%T increases) – the diffusivity of protein peaks change, which impacts two different steps of the assay. First, during the cell lysis and protein separations, proteins from the lysate diffuse in all directions. At higher gel concentrations, less diffusion occurs and protein band width decreases, thus resulting in an increase in the local concentration of protein. On the other hand, as pore size decreases, we anticipate reduced antibody partitioning into the gel when immunoprobings is performed after electrophoresis⁵⁰. The size-exclusion phenomenon could prevent sufficient antibody from reaching its separated protein target and adversely impact binding, compromising the lower limits of detection for an immunoprobings assay (area-under-the-curve, AUC).

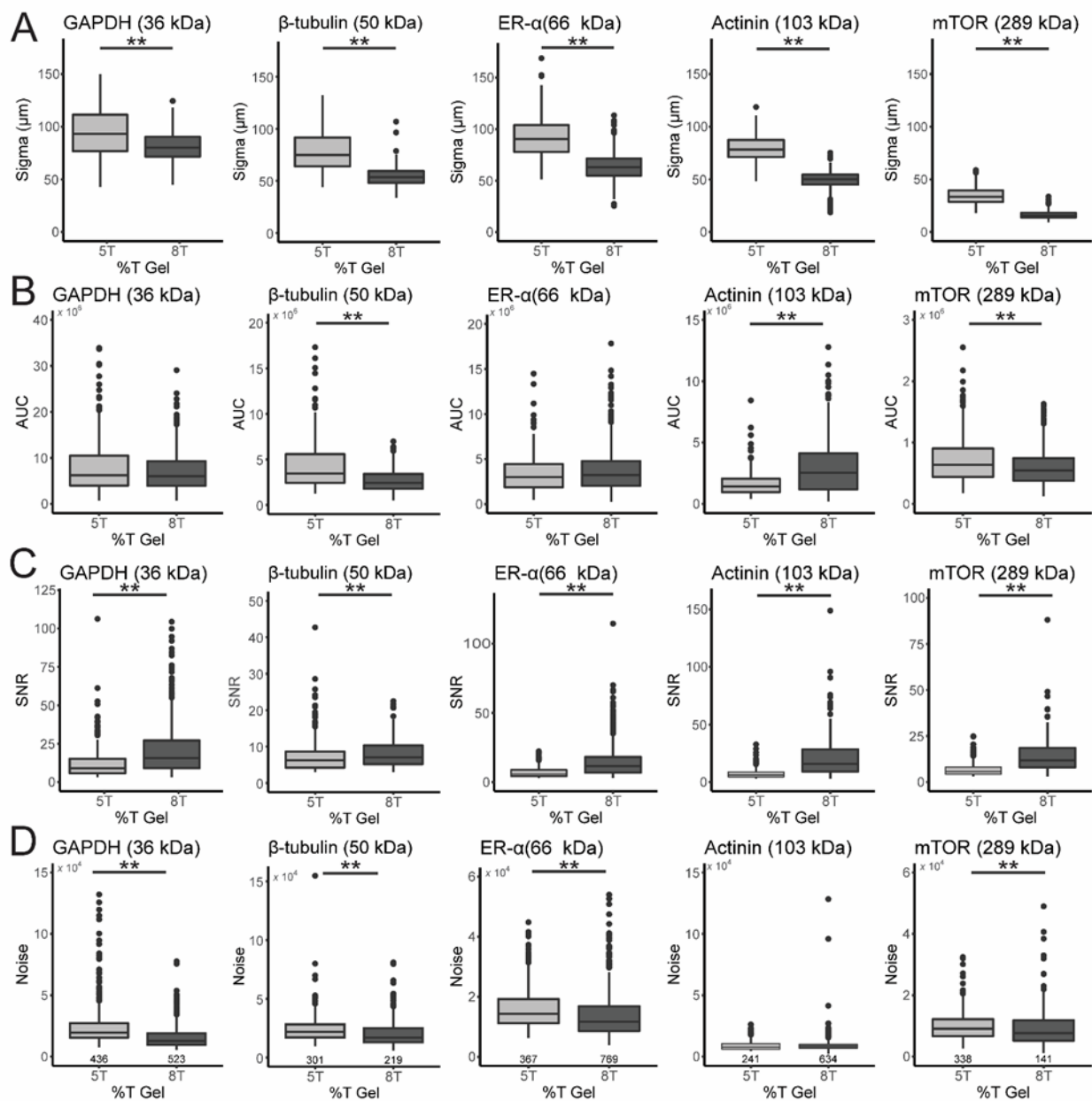


Figure 2-5: Comparisons of different fluorescent protein signal characteristics between 5%T and 8%T gels for all five immunoprobed protein targets.

A) As the concentration of acrylamide increases, the pore size in the gel matrix decreases. Thus, for the 8%T gels, we observe less diffusion of protein out of the gel during the lysis and electrophoresis steps of the assay. B) However, we do not consistently observe the expected trade-off with pore size and diffusion of immunoprobes to detect protein targets. The relative protein signal (AUC measurement), is only significantly lower in two of the five protein targets probed. C) We observe that the SNR in smaller pore gels (8%T) are significantly greater than the SNRs measured in the larger pore gels (5%T) across all 5 protein targets. D) Further analysis of SNR, looking specifically at the noise of the background revealed significantly higher noise for most protein in the lower %T condition. Number of cells analyzed is shown at the bottom of 4D and was consistent across all metrics. Statistical analysis performed using Mann Whitney U tests, where ‘***’ represent p-values <0.01.

As expected from diffusion theory, we observed a significant decrease in the width of the protein target (σ) in the smaller-pore-size gels vs. the σ of each respective target in the larger-pore-size gels ($\sigma_{8\%T}$ vs. $\sigma_{5\%T}$; GAPDH, 36 kDa, β -tubulin, 50 kDa; ER- α , 66 kDa; Actinin, 103 kDa; and mTOR, 289 kDa; $n = 3$ replicate devices, Mann Whitney U tests, p-values of < 0.01 , Figure 2-5A). In comparing across protein targets, the value of σ decreases with increasing molecular mass.

When analyzing the AUC results, only three of the five proteins analyzed have a significant difference between the different gel concentrations, of which two proteins have a smaller AUC value in the smaller-pore-size (higher %T) gel (Mann Whitney U tests, p-values of < 0.01 , Figure 2-5B). These results indicate that the AUC measurement is not solely a result of diffusion trade-off between the protein target diffusing out and the antibody probe diffusing in. There are other factors, such as the partitioning and binding kinetics of each individual antibody, that influence AUC in addition to the change in PA concentration of the gel. Partitioning behavior is influenced by a number of factors in addition to size, such as overall charge and surface properties (hydrophobicity) of the molecule and gel, which can counteract diffusion. The binding kinetics (K_D) of each antibody and its target protein, and the secondary antibody binding kinetics to the primary antibody also impact the total amount of protein that can be detected in the final AUC measurement.

To more definitively determine the effect of pore size on protein detection, measuring the signal-to-noise ratio (SNR) of detected protein peaks is useful. AUC measures the total amount of protein in each protein band, but only for proteins peaks that have an $SNR \geq 3$. Across the five protein targets studied, we observe a significant increase in the SNR of protein signals detected in the smaller-pore-size gel (8%T), particularly with the larger molecular mass proteins (Mann Whitney U tests, p-values of < 0.01 , Figure 2-5C). Higher SNR values indicate enhanced target detection. In general, we are also able to recover a higher percentage of protein peaks that pass our quality control steps and have an $SNR \geq 3$ in the higher %T gels (Figure 2-6). The increased local concentration of protein in the 8%T gels results in larger peak amplitudes in the corresponding intensity profiles, increasing the calculated SNR. Further analysis specifically of the noise (Figure 2-5D), revealed that there was higher background noise in the lower %T gel. Higher noise could be due to increased antibody partitioning into the larger-pore-size gel and becoming trapped in the gel matrix. Thus, our ability to detect protein is dependent on the trade-off between protein and immunoprobe diffusion in the

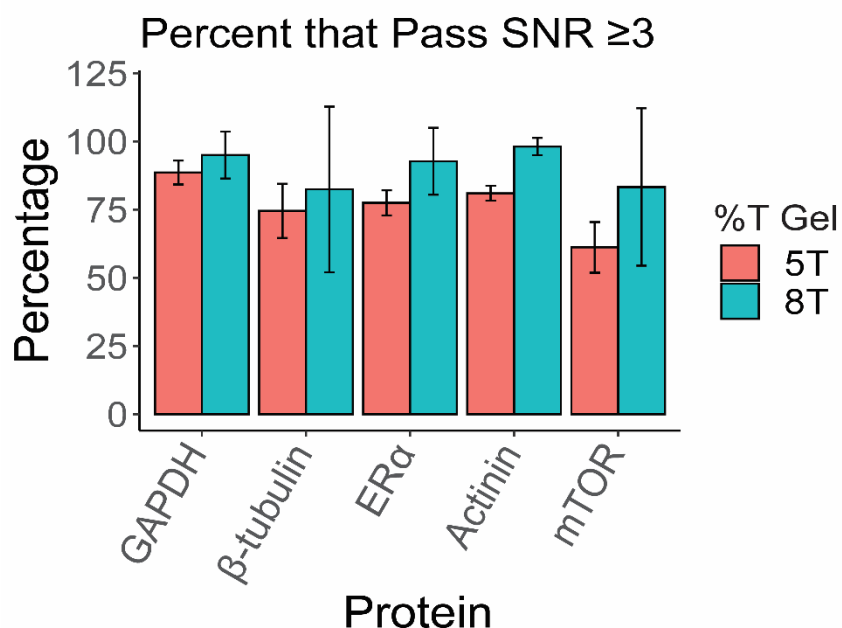


Figure 2-6. Percent of the peaks that pass QC in the MATLAB scripts and have SNR ≥ 3 . Percentage of protein peaks that have SNR ≥ 3 out of total number of protein peaks that passed initial quality control in the custom MATLAB scripts and for each protein comparing large pore size gel (5%T) to small pore size gel (8%T). Each bar represents the average percentage of 3 replicate devices with the error bars representing standard deviation.

2.4 Conclusions

Microscale protein separations of single cells enable the detection of endogenous proteins across a heterogeneous cell population. This is particularly useful in detecting rare proteins and their isoforms in dynamic cell populations, such as differentiating or cancerous cells. In order to fully utilize these systems, it is imperative to understand system capabilities. In this work we have analyzed the electrophoretic mobility of endogenous protein lysed from single-cells on-chip immediately prior to performing electrophoretic separations. Specifically, we analyzed the differences in electrophoretic mobility as the gel concentration changes.

Initially, we fit the log-linear relationship between migration distance and molecular mass proposed by Shapiro et al. of nine protein targets in each of the three gel concentrations tested. However, the models' predictions for the largest molecular mass protein were inaccurate by 13.5 – 44.5%. Upon further analysis of protein electrophoretic mobility, we identified that the migration distance for the largest protein, mTOR (289 kDa) deviated from linear-fit models by $>44\%$ for the smaller pore-size gel (8%T). Furthermore, the free-solution mobility of mTOR was lower than the other proteins examined, indicating that the current assay conditions are not optimized for this large molecular mass species. As a result, we did not include mTOR when drawing conclusions from the Ferguson analysis.

In addition to migration, we also investigated the effect of gel concentration, and thus pore size, on the immunoassay performance and our ability to detect protein in different gel concentrations. As expected, with an increase in gel concentration, the spread (peak width, σ) of the protein band decreases, indicating that diffusion of the protein molecules decreases. Thus, we predicted that antibody diffusion into the gel would decrease as well, which would be measured by lower protein abundance in higher %T gels. However, we did not observe a significant difference in AUC across all protein targets, indicating that the AUC measurement is not sensitive to changes in pore size alone and there are other factors impacting the measurement. Therefore, to further understand the impact of gel concentration, we analyzed the SNR of detected proteins and observed significantly higher SNR values at higher gel concentrations. We concluded that the less diffuse, higher local concentration of proteins enables improved detection of protein targets.

As a result of this study, we observe that there are trade-offs when selecting the assay conditions for a particular experiment. While lower gel concentrations are more likely to follow the expected log-linear relationship between protein migration and molecular mass, there is a trade-off with signal detection capability due to increased diffusion and thus lower SNR values for the protein peaks detected. Moreover, the assay conditions developed here are not suitable for larger proteins. Future investigations into achieving complete solubilization and denaturation of larger molecular mass proteins by optimizing chemical lysis conditions (i.e. temperature, time) or by combining alternative lysis methods such as electrical lysis techniques⁵¹ may be able to overcome solubilization challenges with larger molecular mass proteins. Additionally, use of larger pore size gels or gradient gels for the electrophoretic separations of large molecular proteins will enable electromigration that adheres to the expected linear-fit models.

2.5 References

- (1) Cheng, J. W.; Chang, T. C.; Bhattacharjee, N.; Folch, A. An Open-Chamber Flow-Focusing Device for Focal Stimulation of Micropatterned Cells. *Biomicrofluidics* **2016**, *10* (2), 024122. <https://doi.org/10.1063/1.4946801>.
- (2) Casavant, B. P.; Berthier, E.; Theberge, A. B.; Berthier, J.; Montanez-Sauri, S. I.; Bischel, L. L.; Brakke, K.; Hedman, C. J.; Bushman, W.; Keller, N. P.; et al. Suspended Microfluidics. *Proc. Natl. Acad. Sci. U. S. A.* **2013**, *110* (25), 10111–10116. <https://doi.org/10.1073/pnas.1302566110>.
- (3) Berry, S. B.; Zhang, T.; Day, J. H.; Su, X.; Wilson, I. Z.; Berthier, E.; Theberge, A. B. Upgrading Well Plates Using Open Microfluidic Patterning. *Lab Chip* **2017**, *17* (24), 4253–4264. <https://doi.org/10.1039/c7lc00878c>.
- (4) Berry, S. M.; Alarid, E. T.; Beebe, D. J. One-Step Purification of Nucleic Acid for Gene Expression Analysis via Immiscible Filtration Assisted by Surface Tension (IFAST). *Lab Chip* **2011**, *11* (10), 1747–1753. <https://doi.org/10.1039/c1lc00004g>.
- (5) Ostling, O.; Johanson, K. J. Microelectrophoretic Study of Radiation-Induced DNA Damages in Individual Mammalian Cell. *Biochem. Biophys. Res. Commun.* **1984**, *123* (1), 291–298.
- (6) Hughes, A. J.; Spelke, D. P.; Xu, Z.; Kang, C.-C.; Schaffer, D. V.; Herr, A. E. Single-Cell Western Blotting. *Nat. Methods* **2014**, *11* (7), 749–755. <https://doi.org/10.1038/nmeth.2992>.
- (7) Kang, C.-C.; Lin, J. M. G.; Xu, Z.; Kumar, S.; Herr, A. E. Single-Cell Western Blotting after Whole-Cell Imaging to Assess Cancer Chemotherapeutic Response. *Anal. Chem.* **2014**, *86* (20), 10429–10436. <https://doi.org/10.1021/ac502932t>.
- (8) Kang, C.; Ward, T. M.; Bockhorn, J.; Schiffman, C.; Huang, H.; Pegram, M. D.; Herr, A. E. Electrophoretic Cytopathology Resolves ERBB2 Forms with Single-Cell Resolution. *npj Precis. Oncol.* **2018**, No. October 2017, 1–10. <https://doi.org/10.1038/s41698-018-0052-3>.
- (9) Yamauchi, K. A.; Herr, A. E. Subcellular Western Blotting of Single Cells. *Microsystems Nanoeng.* **2017**, *3* (1), 1–9. <https://doi.org/10.1038/micronano.2016.79>.
- (10) Sinkala, E.; Rosàs-Canyelles, E.; Herr, A. E. Single-Cell Mobility Shift Electrophoresis Reports Protein Localization to the Cell Membrane. *Analyst* **2019**, *144* (3), 972–979. <https://doi.org/10.1039/C8AN01441H>.
- (11) Shapiro, A. L.; Vinuela, E.; Maizel Jr., J. V. Molecular Weight Estimation of Polypeptide Chains by Electrophoresis in SDS-Polyacrylamide Gels. *Biochem. Biophys. Res. Commun.* **1967**, *28* (5), 815–820.
- (12) Duncombe, T. A.; Kang, C.-C.; Maity, S.; Ward, T. M.; Pegram, M. D.; Murthy, N.; Herr, A. E. Hydrogel Pore-Size Modulation for Enhanced Single-Cell Western Blotting. *Adv. Mater.* **2016**, *28* (2), 327–334. <https://doi.org/10.1002/adma.201503939>.
- (13) Kim, J. J.; Chan, P. P. Y.; Vlassakis, J.; Geldert, A.; Herr, A. E. Microparticle Delivery of Protein Markers for Single-Cell Western Blotting from Microwells. *Small* **2018**, *14* (48), 1802865. <https://doi.org/10.1002/sml.201802865>.
- (14) Weber, K.; Osborn, M. The Reliability of Molecular Weight Determinations by Dodecyl Sulfate-Polyacrylamide Gel Electrophoresis. *J. Biol. Chem.* **1969**, *244* (16), 4406–4412.

- (15) Westerhuis, W. H. J.; Sturgis, J. N.; Niederman, R. A. Reevaluation of the Electrophoretic Migration Behavior of Soluble Globular Proteins in the Native and Detergent-Denatured States in Polyacrylamide Gels. *Anal. Biochem.* **2000**, *284* (1), 143–152. <https://doi.org/10.1006/abio.2000.4684>.
- (16) Reynolds, J. A.; Tanford, C. Binding of Dodecyl Sulfate to Proteins at High Binding Ratios. Possible Implications for the State of Proteins in Biological Membranes. *Proc. Natl. Acad. Sci. U. S. A.* **1970**, *66* (3), 1002–1007. <https://doi.org/10.1073/pnas.66.3.1002>.
- (17) Reynolds, J. A.; Tanford, C. The Gross Conformation of Protein-Sodium Dodecyl Sulfate Complexes. *J. Biol. Chem.* **1970**, *245* (19), 5161–5165.
- (18) Ferguson, K. A. Starch-Gel Electrophoresis-Applications to the Classification of Pituitary Proteins and Polypeptides. *Metabolism* **1964**, *13* (10), 985–1002.
- (19) Rodbard, D.; Chrumbach, A. Estimation of Molecular Radius, Free Mobility, and Valence Using Polyacrylamide Gel Electrophoresis. *Anal. Biochem.* **1971**, *40*, 95–134.
- (20) Ogston, A. G. The Space in a Uniform Random Suspension of Fibres. *Trans. Faraday Soc.* **1958**, *54*, 1754–1757.
- (21) Rodbard, D.; Chrumbach, A. Unified Theory for Gel Electrophoresis and Gel Filtration. *Proc. Natl. Acad. Sci.* **1970**, *65* (4), 970–977. <https://doi.org/10.1073/pnas.65.4.970>.
- (22) Morris, C. J. O R.; Morris, P. Molecular-Sieve Chromatography and Electrophoresis in Polyacrylamide Gels. *Biochem. J* **1971**, *124*, 517–528.
- (23) Tung, J.-S.; Knight, C. A. Effect of Charge on the Determination of Molecular Weight of Proteins by Gele Electrophoresis in SDS. *Biochem. Biophys. Res. Commun.* **1971**, *42* (6), 59–76.
- (24) Furthmayr, H.; Timpl, R. Characterization of Collagen Peptides by Sodium Dodecylsulfate-Polyacrylamide Electrophoresis. *Anal. Biochem.* **1971**, *41* (2), 510–516. [https://doi.org/10.1016/0003-2697\(71\)90173-4](https://doi.org/10.1016/0003-2697(71)90173-4).
- (25) Bretscher, M. S. Major Human Erthrocyte Glycoprotein Spans the Cell Membrane. *Nature* **1971**, *26* (138), 584–585.
- (26) Leach, B. S.; Collawn, J. F.; Fish, W. W. Behavior of Glycopolypeptides with Empirical Molecular Weight Estimation Methods. 1. In Sodium Dodecyl Sulfate. *Biochemistry* **1980**, *19* (25), 5734–5741. <https://doi.org/10.1021/bi00566a011>.
- (27) Trayer, H. R.; Nozaki, Y.; Reynolds, J. A.; Tanford, C. Polypeptide Chains from Human Red Blood Cell Membranes. *J. Biol. Chem.* **1971**, *246* (14), 4485–4488.
- (28) Banker, G. A.; Cotman, C. W. Measurement Coefficient Complexes of Free by Gel Electrophoretic Dodecyl Mobility Sulfate and Retardation of Protein-Sodium Electrophoresis. *J. Biol. Chem.* **1972**, *24* (18), 5856–5861.
- (29) Righetti, P. G. *Isoelectric Focusing : Theory, Methodology, and Applications*; Elsevier Biomedical Press, 1984.
- (30) Schägger, H.; Aquila, H.; Von Jagow, G. Coomassie Blue-Sodium Dodecyl Sulfate-Polyacrylamide Gel Electrophoresis for Direct Visualization of Polypeptides during Electrophoresis. *Anal. Biochem.* **1988**, *173* (1), 201–205. [https://doi.org/10.1016/0003-2697\(88\)90179-0](https://doi.org/10.1016/0003-2697(88)90179-0).
- (31) Kang, C.-C.; Yamauchi, K. A.; Vlassakis, J.; Sinkala, E.; Duncombe, T. A.; Herr, A. E. Single Cell-Resolution Western Blotting. *Nat. Protoc.* **2016**, *11* (8), 1508–

1530. <https://doi.org/10.1038/nprot.2016.089>.
- (32) Vlassakis, J.; Herr, A. E. Joule Heating-Induced Dispersion in Open Microfluidic Electrophoretic Cytometry. *Anal. Chem.* **2017**, *89* (23), 12787–12796. <https://doi.org/10.1021/acs.analchem.7b03096>.
- (33) Rueden, C. T.; Schindelin, J.; Hiner, M. C.; DeZonia, B. E.; Walter, A. E.; Arena, E. T.; Eliceiri, K. W. ImageJ2: ImageJ for the next Generation of Scientific Image Data. *BMC Bioinformatics* **2017**, *18* (1), 1–26. <https://doi.org/10.1186/s12859-017-1934-z>.
- (34) Schindelin, J.; Arganda-Carreras, I.; Frise, E.; Kaynig, V.; Longair, M.; Pietzsch, T.; Preibisch, S.; Rueden, C.; Saalfeld, S.; Schmid, B.; et al. Fiji: An Open-Source Platform for Biological-Image Analysis. *Nature Methods*. Nature Publishing Group July 28, 2012, pp 676–682. <https://doi.org/10.1038/nmeth.2019>.
- (35) Rabilloud, T. Solubilization of Proteins for Electrophoretic Analyses. *Electrophoresis* **1996**, *17* (5), 813–829. <https://doi.org/10.1002/elps.1150170503>.
- (36) Huang-Fu, N.; Cheng, J. S.; Wang, Y.; Li, Z. W.; Wang, S. H. Neat1 Regulates Oxidized Low-Density Lipoprotein-Induced Inflammation and Lipid Uptake in Macrophages via Paraspeckle Formation. *Mol. Med. Rep.* **2018**, *17* (2), 3092–3098. <https://doi.org/10.3892/mmr.2017.8211>.
- (37) Cai, Y.; Wee, S. Y. K.; Chen, J.; Teo, B. H. D.; Ng, Y. L. C.; Leong, K. P.; Lu, J. Broad Susceptibility of Nucleolar Proteins and Autoantigens to Complement C1 Protease Degradation. *J. Immunol.* **2017**, *199* (12), 3981–3990. <https://doi.org/10.4049/jimmunol.1700728>.
- (38) Nalvarte, I.; Schwend, T.; Gustafsson, J. Å. Proteomics Analysis of the Estrogen Receptor α Receptosome. *Mol. Cell. Proteomics* **2010**, *9* (7), 1411–1422. <https://doi.org/10.1074/mcp.M900457-MCP200>.
- (39) Bottini, S.; Hamouda-Tekaya, N.; Mategot, R.; Zaragosi, L. E.; Audebert, S.; Pisano, S.; Grandjean, V.; Mauduit, C.; Benahmed, M.; Barbry, P.; et al. Post-Transcriptional Gene Silencing Mediated by MicroRNAs Is Controlled by Nucleoplasmic Sfpq. *Nat. Commun.* **2017**, *8* (1), 1–16. <https://doi.org/10.1038/s41467-017-01126-x>.
- (40) Snijders, A. P.; Hautbergue, G. M.; Bloom, A.; Williamsom, J. C.; Minshull, T. C.; Phillips, H. L.; Mihaylov, S. R.; Gjerde, D. T.; Hornby, D. P.; Wilson, S. A.; et al. Arginine Methylation and Citrullination of Splicing Factor Proline- and Glutamine-Rich (SFPQ/PSF) Regulates Its Association with MRNA. *RNA* **2015**, *21* (3), 347–359. <https://doi.org/10.1261/rna.045138.114>.
- (41) Dunker, A. K.; Rueckert, R. R. Observations on Molecular Weight Determinations on Polyacrylamide Gel. *J. Biol. Chem.* **1969**, *244* (18), 5074–5080.
- (42) Werner, W. E. Ferguson Plot Analysis of High Molecular Weight Glutenin Subunits by Capillary Electrophoresis. *Cereal Chem.* **1995**, *72* (3), 248–251.
- (43) Tastet, C.; Lescuyer, P.; Diemer, H.; Luche, S.; van Dorsselaer, A.; Rabilloud, T. A Versatile Electrophoresis System for the Analysis of High- and Low-Molecular-Weight Proteins. *Electrophoresis* **2003**, *24* (11), 1787–1794. <https://doi.org/10.1002/elps.200305400>.
- (44) Guttman, A.; Nolan, J. Comparison of the Separation of Proteins by Sodium Dodecyl Sulfate-Slab Gel Electrophoresis and Capillary Sodium Dodecyl Sulfate-Gel Electrophoresis. *Analytical Biochemistry*. 1994, pp 285–289.

- <https://doi.org/10.1006/abio.1994.1413>.
- (45) Warren, C. M.; Krzesinski, P. R.; Greaser, M. L. Vertical Agarose Gel Electrophoresis and Electroblotting of High-Molecular-Weight Proteins. *Electrophoresis* **2003**, *24* (11), 1695–1702. <https://doi.org/10.1002/elps.200305392>.
- (46) Neville, David M., J. Molecular Weight Determination of Protein-Dodecyl Sulfate Complexes by Gel Electrophoresis in a Discontinuous Buffer System. *J. Biol. Chem.* **1971**, *246* (20), 6328–6334.
- (47) Bass, J. J.; Wilkinson, D. J.; Rankin, D.; Phillips, B. E.; Szewczyk, N. J.; Smith, K.; Atherton, P. J. An Overview of Technical Considerations for Western Blotting Applications to Physiological Research. *Scand. J. Med. Sci. Sport.* **2017**, *27* (1), 4–25. <https://doi.org/10.1111/sms.12702>.
- (48) Otzen, D. Protein – Surfactant Interactions: A Tale of Many States. *Biochim. Biophys. Acta* **2011**, *1814* (5), 562–591. <https://doi.org/10.1016/j.bbapap.2011.03.003>.
- (49) Rath, A.; Glibowicka, M.; Nadeau, V. G.; Chen, G.; Deber, C. M. Detergent Binding Explains Anomalous SDS-PAGE Migration of Membrane Proteins. *Proc. Natl. Acad. Sci. U. S. A.* **2009**, *106* (6), 1760–1765. <https://doi.org/10.1073/pnas.0813167106>.
- (50) Tong, J.; Anderson, J. L. Partitioning and Diffusion of Proteins and Linear Polymers in Polyacrylamide Gels. *Biophys. J.* **1996**, *70* (March), 1505–1513. [https://doi.org/10.1016/S0006-3495\(96\)79712-6](https://doi.org/10.1016/S0006-3495(96)79712-6).
- (51) Sims, C. E.; Allbritton, N. L. Analysis of Single Mammalian Cells On-Chip. *Lab Chip* **2007**, *7* (4), 423–440. <https://doi.org/10.1039/b615235j>.

Chapter 3: Comparison of Photoactivatable Crosslinkers for In-Gel Immunoassays

This work was performed in collaboration with Surbhi Desai, Ph.D.; Erum Raja, Ph.D.; Chris Etienne, Ph.D.; Brian Webb, Ph.D.; and Amy E. Herr, Ph.D.

3.1 Introduction

Beyond drug delivery vehicles¹ and cell² and tissue engineering scaffolds^{3,4}, functionalized hydrogels play an increasingly important role in measurement science. From biosensing⁵ to protein microarrays^{6,7}, immunoassays utilize hydrogel structures due to the higher capacity⁸ and sensitivity of hydrogel-based protein chips compared to surface-based chips⁹. For hydrogel-based immunoassays, proteins are immobilized in the hydrogel matrix for immunoprobng, often relying on fluorescence detection as the target signal read-out method.

When designing immunoassays with fluorescence detection, it is important to consider sources of background fluorescence that can obscure the target signal. Background can originate from instrumentation and environmental sources (e.g. the excitation source, camera or ambient light) as well as from the sample, which can include autofluorescence from the sample or hydrogel material, as well as fluorescence from non-specific antibody interactions.

Benzophenone is a photoactivatable molecule that has been utilized to crosslink protein into hydrogel matrices for immunoassays¹⁰. Upon UV activation, the benzophenone molecule is activated to a biradical, able to abstract hydrogens from nearby C-H bonds, such as those on the protein backbone, and recombine to form a covalent C-C bond¹¹. To functionalize hydrogels with benzophenone, benzophenone methacrylamide (BPMA) has been previously synthesized and incorporated into the hydrogel matrix during polymerization¹⁰. BPMA hydrogels have been used to perform in-gel immunoprobng of target antigens, including the probng step of single-cell immunoblotting following microscale protein separations¹².

However, with BPMA hydrogels, background fluorescence must be considered as the aromatic structure of benzophenone contributes to increase fluorescence immunoassay background signal. First, the aromatic ring structure on benzophenone contains conjugated double bonds, resulting in fluorescence in the visible spectrum and is a source of autofluorescence in the hydrogel¹³. Furthermore, upon photoactivation, a side product (benzopinacol) can be formed that also emits fluorescence^{13,14}. Second, the hydrophobic aromatic ring structures of both benzophenone and benzopinacol may facilitate non-specific hydrophobic interactions¹³ that lead to increased immunoassay background signal from non-specific retention of unbound fluorescent probes¹⁵. To boost in-gel immunoassay performance by reducing fluorescence background signal, we consider an alternative photoactivatable molecule utilized for protein crosslinking, diazirine. Diazirine is 1) more hydrophilic than benzophenone^{16,17} and thus less likely to non-specifically interact with hydrophobic immunoprobngs, and 2) lacks conjugated double bonds to emit photons in the visible spectra upon activation. The

chemical structure of diazirine consists of a three-membered ring comprised of two nitrogen atoms and one carbon atom. Upon UV activation (~ 350 nm), the diazirine ring breaks, irreversibly releasing N_2 and forming a reactive carbene species that can insert into nearby C-H or heteroatom-H bonds to form a covalent bond^{18,19}.

However, the highly reactive carbene species has a shorter half-life, in the pico- to nano-second range, compared to the benzophenone diradical half-life of $120 \mu s$ ¹⁹. Furthermore, while the benzophenone diradical can relax back to the original benzophenone molecule and is available for reactivation upon subsequent exposure to UV¹¹, carbenes can be quenched by the surrounding solvent, resulting in lower protein target crosslinking efficiency compared to benzophenone^{18,20}. We hypothesize that the hydrophilic structure of diazirine will allow a higher concentration diazirine to be solubilized in the hydrogel precursor to improve in-gel protein capture while the hydrophobic structure of benzophenone limits the concentration that can be solubilized in the hydrogel precursor.

Here, we seek to reduce in-gel fluorescence background signal utilizing diazirine functionalized to acrylamide, hypothesizing that diazirine exhibits both reduced autofluorescence and reduced non-specific hydrophobic interactions based on its chemical properties. We first synthesized diazirine methacrylamide (DZMA) to enable incorporation of diazirine into polyacrylamide (PA) hydrogels. We then utilized hydrogel functionalized with varying concentrations of DZMA to determine the optimal concentration that would enable comparable protein capture to standard benzophenone gels. Next, we compared the background signal from non-specific antibody interactions and autofluorescence in diazirine and benzophenone functionalized hydrogels. Finally, we utilized DZMA hydrogels to quantify single-cell protein expression in an in-gel immunoassay and compared signal-to-noise ratios of detected protein targets to BPMA hydrogels. Our findings indicate that initial results with diazirine demonstrated comparable signal-to-noise ratios with BPMA hydrogels due to lower background signal, however further investigation into diazirine chemistry may be necessary for its use to specific immunoassay applications.

3.2 Materials and Methods

Antibodies

The primary antibody to GFP (goat pAb; ab6673) was purchased from Abcam and the primary antibody to PTBP1 (mouse mAb; WH0005725M1) was purchased from Millipore Sigma. The secondary antibody to mouse IgG pre-labelled with Alexa Fluor 555 (A31570) was purchased from Thermo Fisher Scientific. All primary antibodies were used at a 1:10 dilution from stock concentrations and incubated for 2 hours at room temperature. Secondary antibodies were diluted to a 1:20 working concentration from stock and incubated for 1 hour at room temperature, protected from light.

Reagents

30%T, 3.3%C acrylamide/bis-acrylamide (29 : 1) (A3574), ammonium persulfate (APS, A3678), and tetramethyl-ethylene- diamine (TEMED, T9281) for gel polymerization, dichlorodimethylsilane (440272) and 3-(trimethoxysilyl)propyl methacrylate (440159) for wafer and glass silanization, respectively, bovine serum albumin (BSA, A7638), fetal

bovine serum (FBS, F2442), Triton X-100 (X100-100ML), and urea (U5378) were purchased from Sigma-Aldrich. Phosphate buffered saline (PBS, 10010023), RPMI 1640 medium (11875), penicillin–streptomycin (15070063) were purchased from Thermo Fisher Scientific. 1.5 M Tris-HCl, pH 8.8 (T1588) was purchased from Teknova, 10× tris-glycine buffer (1610734) was purchased from Biorad, and 10× Tris buffered saline with Tween 20 (TBST, 9997S) was purchased from Cell Signaling Technologies. Deionized water (18.2 MΩ) was obtained using an Ultrapure water system from Millipore. N-[3-[(3-Benzoylphenyl)formamido]propyl]methacrylamide (BPMA) was custom synthesized by PharmAgra Laboratories^{12,21}.

SU8 and polyacrylamide (PA) gel fabrication

SU8 fabrication to generate the master wafer and PA gel fabrication were performed as described previously.¹² Diazirine methacrylamide and N-[3-[(3-Benzoylphenyl)formamido]propyl]methacrylamide (BPMA) were each solubilized in DMSO in a stock concentration before being added to the 8%T PA precursor in equal volumes. For the negative control, a blank vehicle control gel containing an equal volume of only DMSO was fabricated. Gels for protein capture and background fluorescence experiments were polymerized on a silanized glass slide using wafers (WaferPro C04009) microfabricated with SU-8 3050 (Kayaku Advanced Materials Y311075) to have ~40 μm “rails”. Gels for single-cell immunoblotting were polymerized on a silanized glass slide using wafers (WaferPro C04009) microfabricated with SU-8 3050 (Kayaku Advanced Materials Y311075) to have 30 μm diameter “posts” to form microwells that were ~45 μm in height. All PA gel precursor was degassed and chemically polymerized with 0.08% APS and 0.08% TEMED. BPMA gels were polymerized for 15-20 minutes, covered and protected from light and DZMA gels were polymerized for 1.5 hours, covered and protected from light.

Protein and Antibody Labelling

His-tag green fluorescent protein (GFP) was labelled in-house with DyLight 633 using the described protocol in the DyLight 633 Antibody Labeling Kit, resulting in a degree-of-labelling of 0.46 fluorophores per molecule of protein. Anti-GFP antibody was labeled in-house using the described protocol in the Alexa Fluor 555 Antibody Labeling Kit, resulting in a degree-of-labeling of 4.16.

Evaluating diazirine methacrylamide protein capture

To quantify in-gel protein capture, we fabricated diazirine gels with increasing concentration of DZMA and used a gasket system (ArrayIt Microarray Gasket, ArrayIt Corporation, Sunnyvale, CA) to physically isolate regions of the gels and selectively incubate regions with a protein or blank solution as previously described²². Purified 0.01 mg/mL of His-GFP protein labeled with DyLight 633 (DOL: 0.4-0.5) diluted in 1x PBS were loaded into pre-selected 1cm x 1cm regions while the remaining regions were loaded with 1x PBS buffer. After a 1-hour incubation, gels were exposed to collimated UV light under a mercury arc lamp (365 nm, at ~18.0 mW/cm², Optical Associates, Inc.) for 100 s activate protein capture molecules to form covalent bonds with diazirine or benzophenone moieties and the protein species. Following UV exposure, gels were subsequently washed in 1x TBST before being dried with N₂ air and imaged on a microarray scanner using the 635 laser channel. After imaging on the laser microarray scanner, 6 ROI regions with immobilized protein were measured for each replicate hydrogel and the integrated intensity of each immobilized protein region was analysed. Background subtraction was

performed using the integrated signal from an adjacent blank (no protein) region to account for any fluorescent signal from the hydrogel itself.

Evaluating Antibody probe contribution to background fluorescence following in-gel immunoprobng

To assess background fluorescence from the antibody probe, 40 μm -thick hydrogels were fabricated for the endpoint range concentrations of DZMA (3mM and 12mM) to compare to a blank vehicle control and 3mM BPMA positive control gel. Protein was loaded and captured into gels following the same protocol for evaluating DZMA protein capture. After dehydration, gels were imaged using a 532 nm excitation laser on the microarray scanner, corresponding to the immunoprobe fluorophore to obtain a “before immunoprobng” baseline measurement of the gel. After imaging, the gel was then rehydrated in 1x TBST before immunoprobng the entire gel (both protein and non-protein containing regions) by diffusing fluorescently labelled anti-GFP primary antibody labeled in-house with Alexa Fluor 555 into the PA gel. Gels were subsequently washed in 1x TBST to remove unbound antibody before being dried with N_2 air and re-imaged on a microarray scanner using the 532 laser channel with same imaging settings to obtain an “after immunoprobng” measurement. The Immunoprobng Target Signal was quantified as the integrated fluorescence signal from protein-region on the probed gel, using the integrated fluorescence signal from the same probed gel of an adjacent blank (non-protein) region for background subtraction. To measure the Immunoprobng Background Signal, the integrated fluorescence signal from the blank region on the gel before immunoprobng was subtracted from the integrated signal from the blank region on the gel after immunoprobng to account for any fluorescence signal from the gel itself.¹²

Evaluating autofluorescence in BPMA and DZMA gels

40 μm -thick hydrogels were fabricated on silanized glass slides. Half of the bottom of the glass slide was covered with Kapton tape and surrounded with aluminum foil to block any light from reaching the gel during UV-exposure, which illuminates from below. The fluorescence signal of the half of the gel that was exposed to UV relative to the fluorescence of the non-UV exposed region was compared across conditions in all four laser channels of the microarray scanner ($\lambda = 488, 532, 594, 635$).

Cell lines and cell harvesting

MDA-MB-231 cells were obtained from the American Type Culture Collection (ATCC) and authenticated (Promega). The MDA-MB-231 cell line was maintained in RPMI 1640 supplemented with 1% penicillin/streptomycin and 10% FBS. Cells were kept in a 37 °C incubator at 5% CO_2 . For single-cell immunoblotting, cells were harvested using 0.05% Trypsin-EDTA (Gibco, 25300-054), and resuspended in 4 °C 1x PBS at a concentration of $\sim 10^6$ cells per mL.

Single-cell Immunoblotting

Single-cell Immunoblotting was performed as described previously²¹. Briefly, cells were pipetted over the PA gel and settled by gravity into the microwells patterned in the PA gel. Lysis buffer heated in a water bath to 55 °C was poured over the PA gel in order to lyse the cells in the microwells for 30 seconds. An electric field ($E = 40\text{Vcm}^{-1}$) was applied to inject and separate proteins for 30 seconds in the PA gel abutting the microwell. After separation, proteins were immobilized in the gel matrix via a 45-second exposure to UV

light (Lightningcure LC5, Hamamatsu) which activated the benzophenone methacrylamide or diazirine methacrylamide functional group (incorporated during gel fabrication) to cross-link proteins to the gel matrix²¹. The UV light guide was held ~25 cm above the gel across all experiments. Immobilized proteins were probed in-gel by diffusing fluorescently labelled antibody probes into the PA gel. A fluorescence microarray scanner (Genepix 4300A, Molecular Devices) equipped with 4-laser lines ($\lambda = 488, 532, 594, 635$) acquired fluorescence readout.

Area under the curve (AUC) and signal-to-noise ratios (SNR) purified protein native separations

Purified Ova was labelled in-house using the described protocol in the DyLight 633 Antibody Labeling Kit, resulting in a degree-of-labelling of 0.28 fluorophores per molecule of protein. Labelled Ova was diluted to 2 μM concentration in 1x PBS. Gels for purified protein native microscale separations were polymerized on a silanized glass slide using wafers microfabricated with SU-8 3050 to have 100 μm diameter “posts” to form microwells that were ~60 μm in height. To run purified protein separations, 250 μL of protein solution was pipetted on the top of gels with 100 μm diameter microwells and 1 mm separation lane. The gel was incubated in protein solution for 90 seconds ($>3\tau$ diffusion timescale for protein to partition into the microwell but not the hydrogel). After incubation, the slide was transferred to the electrophoresis chamber and 17 mL of room-temperature non-denaturing run buffer (1x Tris-Glycine) was poured into the chamber and an electric field ($E = 40\text{Vcm}^{-1}$) was immediately applied to inject and separate proteins for 27 seconds in the PA gel abutting the microwell. After separation, proteins were immobilized in the gel matrix via a 45-second exposure to UV light (Lightningcure LC5, Hamamatsu) which activated the BPMA or DZMA functional group (incorporated during gel fabrication) to cross-link proteins to the gel matrix²¹. The UV light guide was held ~25 cm above the gel across all experiments. Immobilized proteins were probed in-gel by diffusing fluorescently labelled antibody probes into the PA gel. A fluorescence microarray scanner (Genepix 4300A, Molecular Devices) equipped with 4-laser lines ($\lambda = 488, 532, 594, 635$) acquired fluorescence readout.

Immunoblot signal quantification and statistical analysis

The images were first processed in Fiji^{23,24} by applying a median filter using the “Remove Outliers” macro with a 2-pixel radius and a threshold value of 50 AFU to remove punctate noise. Quantification of fluorescence signal from immunoblots was processed by in-house scripts written in MATLAB (R2018b) as previously described²¹. Gaussian curves were fit to fluorescence intensity profiles in MATLAB (R2018b, Curve Fitting Toolbox) in order to obtain the mean μ (used to describe the protein migration distance) and the variance σ^2 (used to calculate peak width as 4σ). Area-under-the-curve (AUC) analysis of the intensity profiles was performed to quantify immunoblot signal 4σ from the fitted-curve peak location. The signal-to-noise ratio was calculated by taking the peak value of the Gaussian fit curve and dividing by the standard deviation of the background region from the 4σ region surrounding the peak. Only protein peaks with $\text{SNR} \geq 3$ were included in

downstream comparisons. Plots and statistical tests were generated and performed with R (version 3.6.1).

Hydrogel swelling ratios in water and 70% IPA

Polyacrylamide precursor was prepared with 12 mM DZMA, 3 mM BPMA, or blank DMSO vehicle control. 1 mm thick gels were fabricated by pipetting polyacrylamide precursor solution between a clean glass plate and a ¼ of a standard microscope glass slide (18.75 x 25 cm), separated by gel casting spacers (C.B.S. Scientific GelWrap, 1 mm thickness) and polymerized for 1 hour. Gels were released from glass to create free-standing 1mm-thick hydrogels. To dose with UV, immediately after fabrication, gels were placed on a glass slide and exposed to collimated UV light under a mercury arc lamp (365 nm, at ~18.0 mW/cm²; Optical Associates, Inc.) for 100 s activate protein capture molecules. Gels were then placed back in MilliQ water to wash overnight (12-18 hours) to remove any salts from the gel. After washing, gels were dehydrated in a 70°C oven until completely dehydrated (~4-6 h). Dehydrated gels were weighed on a scale (Mettler Toledo ME204E) to obtain the gel “dry weight”. Gels were rehydrated by incubating in either MilliQ H₂O or 70% isopropyl alcohol. After 24 h of incubation, swollen gels were weighed again for the “swollen” weight. The swelling ratio (Q) was calculated as

$$Q = \frac{Weight_{swollen}}{Weight_{dry}}. \quad 3.1$$

3.3 Results and Discussion

Comparing Protein Capture in BPMA and DZMA Hydrogels

After synthesizing diazirine methacrylamide (DZMA) (Appendix A1), we incorporated varying concentrations of DZMA into the hydrogel precursor to measure protein capture. Due to the 1) shorter half-life of activated diazirine (ps-ns range) compared to activated benzophenone (80-120 μs)¹⁹, 2) potential quenching of the diazirine reaction by water whereas benzophenone can be repeatedly reactivated^{19,25}, and 3) formation of a relatively stable diazo isomer side product upon diazirine activation¹⁸, we hypothesize that in-gel protein capture will be lower with diazirine compared to benzophenone. However, due to lower hydrophobicity of diazirine molecules compared to benzophenone molecules (based on predicted and experimental logP values^{16,17}) we hypothesize that we can incorporate a higher concentration of diazirine in the hydrogel precursor to increase the protein capture efficiency.

To assess protein-capture ability of DZMA gels, we labeled GFP protein with DyLight 633 (GFP*) to immobilize in the hydrogel. We utilized the signal from the small fluorophore label to quantify protein capture instead of relying on the native GFP fluorescence which is dependent on the secondary protein structure and may be disrupted during in-gel immobilization and alter fluorescence readout. For each gel condition, we incubated physically isolated regions of the gel with either GFP* protein solution or a blank 1x PBS solution (Figure 3-1A). After UV exposure to activate protein crosslinking, we washed the gels to remove uncaptured GFP* before scanning on a microarray scanner to measure the DyLight 633 fluorescence signal. We quantified protein capture from gel regions incubated with GFP* protein (Protein ROI), using blank gel regions (Blank ROI) incubated with 1x PBS, for background subtraction:

$$\text{Protein Capture Signal} = \text{Fluorescence}_{\text{Protein ROI}} - \text{Fluorescence}_{\text{Blank ROI}}$$

3.2

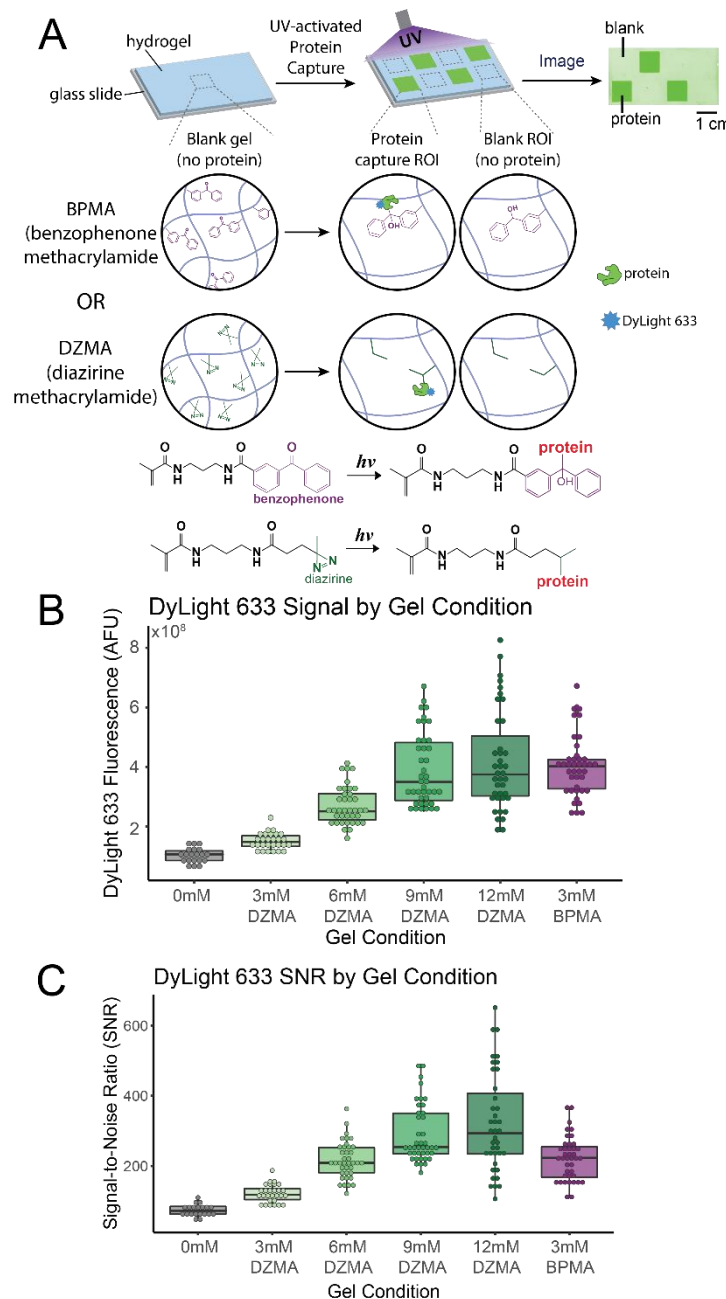


Figure 3-1 In-gel protein capture of DyLight 633 labelled protein target in DZA and BPMA functionalized hydrogels.

(A) Schematic of hydrogels functionalized with BPMA or DZA and protein capture. Hydrogels are fabricated with either BPMA or DZA functional group. Specific regions of the gel are incubated with protein and protein capture is initiated by exposure to UV light. (B) Integrated fluorescence of protein regions in hydrogels with varying concentration of DZA compared to 0 mM negative control and standard 3 mM BPMA gels. Integrated DyLight 633 signal increases as DZA concentration increases, indicating greater protein capture at higher DZA concentrations. (C) Corresponding signal-to-noise ratios of protein capture.

When DZMA was added at the same concentration as standard BPMA gels (3 mM)^{12,21} to the gel precursor, DZMA gels had significantly lower fluorescence signal (Kruskal-

Wallis with Holm correction, $p < 0.01$, $n = 3$ slides, 9-11 ROI regions) (Figure 3-1B). Increasing the concentration of DZMA up to 12 mM in the PA precursor resulted in comparable protein capture signal and higher signal-to-noise ratios (SNR) than the standard 3 mM BPMA gels. However, as we increased the concentration of DZMA, we observed that the time for hydrogel polymerization increased, despite using equivalent volume of the DMSO solvent.

Our results support our hypothesis that DZMA hydrogels have lower capture efficiency than BPMA hydrogels, evidenced by lower protein target signal in 3 mM DZMA gels compared to the protein target signal from the equivalent concentration 3 mM BPMA gels. However, by increasing the concentration of diazirine in the gel precursor, we were able to achieve greater protein capture compared to lower DZMA concentrations. The longer polymerization times associated with higher DZMA concentrations potentially indicate that higher concentrations of photoactivatable molecules interfere with the hydrogel polymerization reaction. Diazirines can serve as carbon radical traps²⁶ and at higher concentrations may be trapping radicals necessary for gel polymerization thus impeding and slowing the polymerization process down. Furthermore, if a portion of the diazirine molecules are quenched during gel polymerization, this could explain why we do not observe equal scaling between concentration of DZMA and fluorescence signal as well as a leveling off of signal at 9 mM and 12 mM DZMA.

Measuring Sources of Background in Hydrogel-based Immunoassays

Upon demonstrating that diazirine can be used for in-gel protein capture, we investigated the background signal from each functionalized hydrogel. We investigated background signal from each molecule due to 1) non-specific antibody retention in gels due to any potential non-specific interactions between the gel matrix and antibody probe and 2) autofluorescence from the photoactive molecule itself. We hypothesize that the aromatic rings in benzophenone serve as a hydrophobic attraction force for immunoprobes to partition into the gel and be non-covalently retained in-gel. Furthermore, the conjugated double bonds in benzophenone result in fluorescence in the visible spectrum upon UV activation, contributing to gel autofluorescence.

To measure background fluorescence from non-specific immunoprobe retention, the same hydrogels used to quantify protein capture in DZMA hydrogels and BPMA hydrogels were used. Following UV protein capture, the gels were imaged before and after immunoprobation using the laser channel corresponding to the fluorescent immunoprobe. Thus, we can measure the fluorescence signal directly due to immunoprobe introduction.

To quantify the immunoprobed target signal (antibody binding to its protein target), we analysed the protein regions in the gel after immunoprobation, using the adjacent non-protein blank regions of the gel after immunoprobation to perform background subtraction. The background subtraction removes any signal due to gel autofluorescence as well as the non-specific antibody retention in the gel (Figure 3-2A).

$$\text{Immunoprobed Target Signal} = \text{Protein ROI}_{\text{probed}} - \text{Blank ROI}_{\text{probed}} \quad 3.3$$

To specifically measure the background signal solely due to non-specific antibody interactions with the gel, we measured the fluorescence signal from the blank, non-protein regions before and after immunoprobation. The signal from the blank regions before immunoprobation was used to mitigate contribution from gel autofluorescence and was subtracted from the fluorescence signal after immunoprobation. Thus, the immunoprobe

background signal only accounts for antibody signal in the gel that is not specifically bound to any protein target (Figure 3-2A).

$$\text{Immunoprobed Background Signal} = \text{Blank ROI}_{\text{after immunoprobng}} - \text{Blank ROI}_{\text{before immunoprobng}} \quad 3.4$$

To quantify the autofluorescence background signal between diazirine and BPMA, we fabricated negative control gels, 12 mM DZMA gels, and 3 mM BPMA gels, and only activated half of the gel with UV light (Figure 3-2B). We compared the fluorescence signal to the non-activated half across the 4 laser channels (488, 532, 594, and 635) of the microarray scanner. We quantified relative autofluorescence as the fluorescence signal from the UV-activated gel normalized by the intensity of the non-activated gel.

$$\text{Relative Autofluorescence} = \frac{\text{Blank ROI}_{\text{UV-activated}}}{\text{Blank ROI}_{\text{non-activated}}} \quad 3.5$$

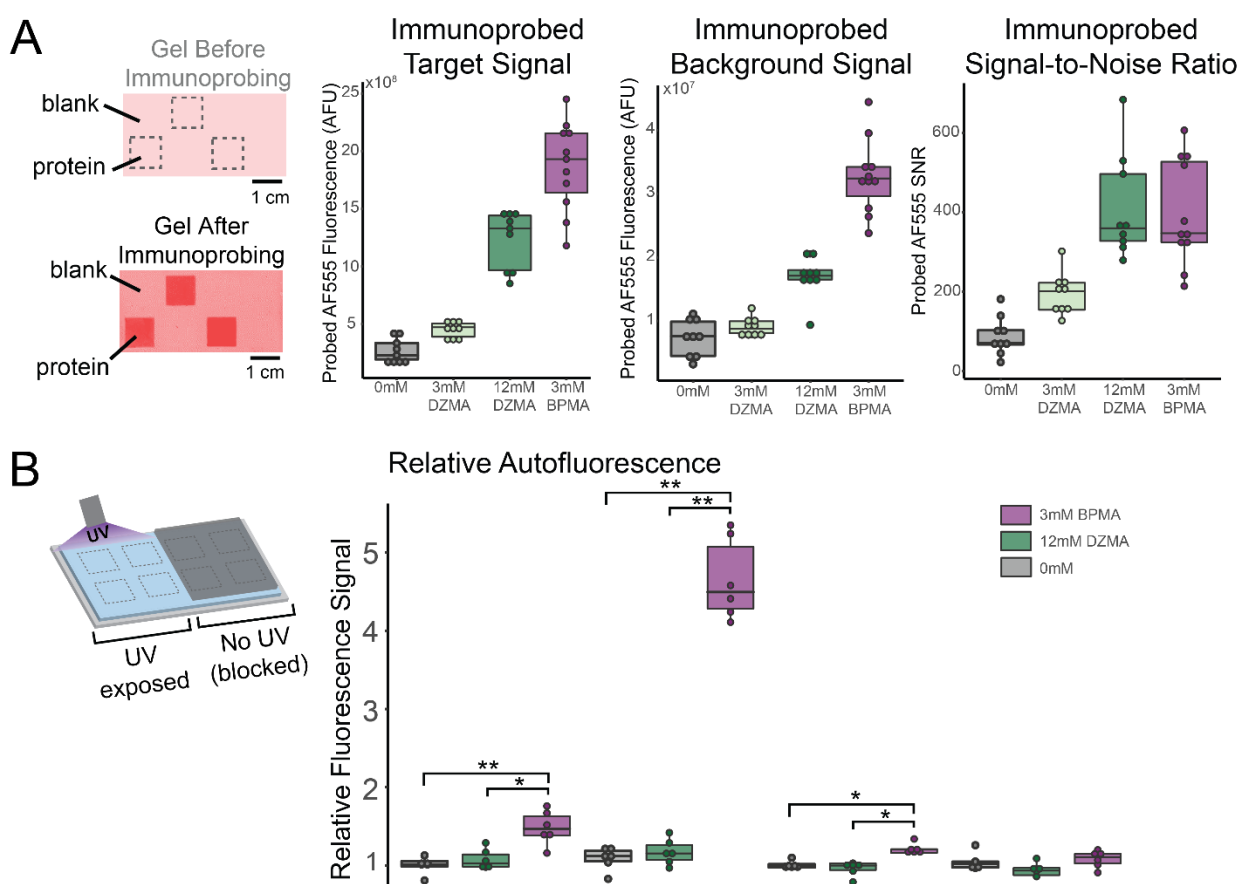


Figure 3-2 Measuring sources that contribute to increased background fluorescence for in-gel immunoassays.

(A) Analysis of the immunoprobed target from fluorescently labelled primary antibody in gel regions incubated with protein (Immunoprobed Target Signal) and blank (no protein) regions (Immunoprobed Background Signal), and corresponding SNR of Immunoprobed Target Signal. While Immunoprobed Target Signal is higher in 3mM BPMAC gels, Immunoprobed Background Signal which corresponds to non-specific antibody retention in the hydrogel is also higher, resulting in comparable SNR between 3 mM BPMAC and 12 mM DZA. (B) Analysis of relative background autofluorescence between 3mM BPMAC gels, 12 mM DZA gels and blank (0mM) negative control gels across four excitation laser channels in the microarray scanner. * $p < 0.05$; ** $p < 0.01$; Kruskal-Wallis with Holm multiple pairwise correction

Compared to 12 mM DZMA gels, 3mM BPMA gels had significantly higher (~1.5x) immunoprobed target signal (Kruskal–Wallis test with Holm pairwise correction, $p < 0.01$, $n = 9-11$ Protein ROIs) (Figure 3-2A), and ~1.9x higher immunoprobed background signal (Kruskal–Wallis test with Holm pairwise correction, $p < 0.01$, $n = 9-11$ Blank ROIs). Despite lower immunoprobed signal in the 12 mM DZMA gels, the SNR of the probed protein was comparable with the SNR in the 3 mM BPMA gels (Kruskal–Wallis test with Holm pairwise correction, $p = 1.0$, $n = 9-11$ Protein ROIs). Blank UV-activated BPMA hydrogels also emitted significant relative autofluorescence compared to negative controls gels (Kruskal-Wallis with Holm correction, $p < 0.01$, $n = 6$ ROIs) (Figure 3-2B), particularly in the 488, 532 nm laser channels, having ~ 1.5x and ~4.7x the relative autofluorescence signal as non-UV-activated BPMA gels, respectively. In contrast, across all laser channels, UV-activated DZMA gels had 0.9x – 1.2x the relative autofluorescence signal of non-activated DZMA gels, comparable to the vehicle control gels ($p > 0.05$, Kruskal–Wallis test with Holm pairwise correction).

The higher immunoprobed background in 3 mM BPMA gels indicates more non-specific interactions retaining probe in the BPMA gels than in DZMA gels, supporting our hypothesis that the aromatic rings in benzophenone are a source of hydrophobic attraction to retain immunoprobes in the gel. As a result, the higher immunoprobed background signal in BPMA gels adversely affected the SNR of the immunoprobed target signal such that SNR was comparable between 12 mM DZMA gels and 3 mM BPMA gels, despite the lower probe signal with 12 mM DZMA gels. Additionally, our relative autofluorescence results demonstrate that the conjugated double bonds in benzophenone adequately absorb electrons to emit autofluorescence, particularly in the 488 and 532 laser channels, which corresponds to benzophenone and benzopinacol emission when activated by UV light¹.

Utilizing diazirine hydrogels to quantify single-cell protein expression

Finally, we investigated diazirine protein capture and SNR when applied to a more complex protein sample (i.e., from single-cell lysate) in an open microfluidic device. We hypothesize that with equivalent protein capture to BPMA hydrogels, the lower background signal in DZMA gels would enable improved detection of low abundance protein targets from single cells. We performed size-based separation single-cell immunoblotting^{12,21}, using the same polyacrylamide concentration (8%T) for BPMA and DZMA hydrogels and SDS-denaturing conditions. Compared to unmodified PA hydrogels, BPMA hydrogels have been shown to slow down protein electrophoretic migration due to smaller pore size²⁷. However an alternatively tetrazole-functionalized polyacrylamide gel was reported to have similar pore size to the unmodified PA gel²⁷ demonstrating that different hydrogel modifications have different impacts on the hydrogel matrix. Thus, we also investigated how diazirine functionalized gels would impact electrophoretic mobility for single-cell immunoblotting, using the same experimental conditions (lysis and electrophoresis buffers and time scales) for BPMA and DZMA hydrogels.

Following single-cell lysis, the protein target PTBP1 migrated 1.3x faster in DZMA gels (electrophoretic mobility (μ) = 0.53 ± 0.03 mm²/V·s, $n = 688$ cells) than in BPMA gels (μ = 0.38 ± 0.02 mm²/V·s, $n = 1322$ cells) ($p < 0.01$; Mann-Whitney U Test) (Figure 3-3D). In addition, protein capture, measured by area under the curve (AUC) of the immunoprobed protein peak, and SNR in the DZMA gels was observed to be much lower, compared to protein peaks in BPMA gels (Figure 3-3C). Protein signal in 12 mM DZMA gels was significantly lower, only 15% of the protein signal (AUC) of the signal measured in the 3 mM BPMA gels and SNR in DZMA gels was 20% of the SNR in BPMA gels ($p < 0.01$; Mann-Whitney U Test, $N = 5$ gels).

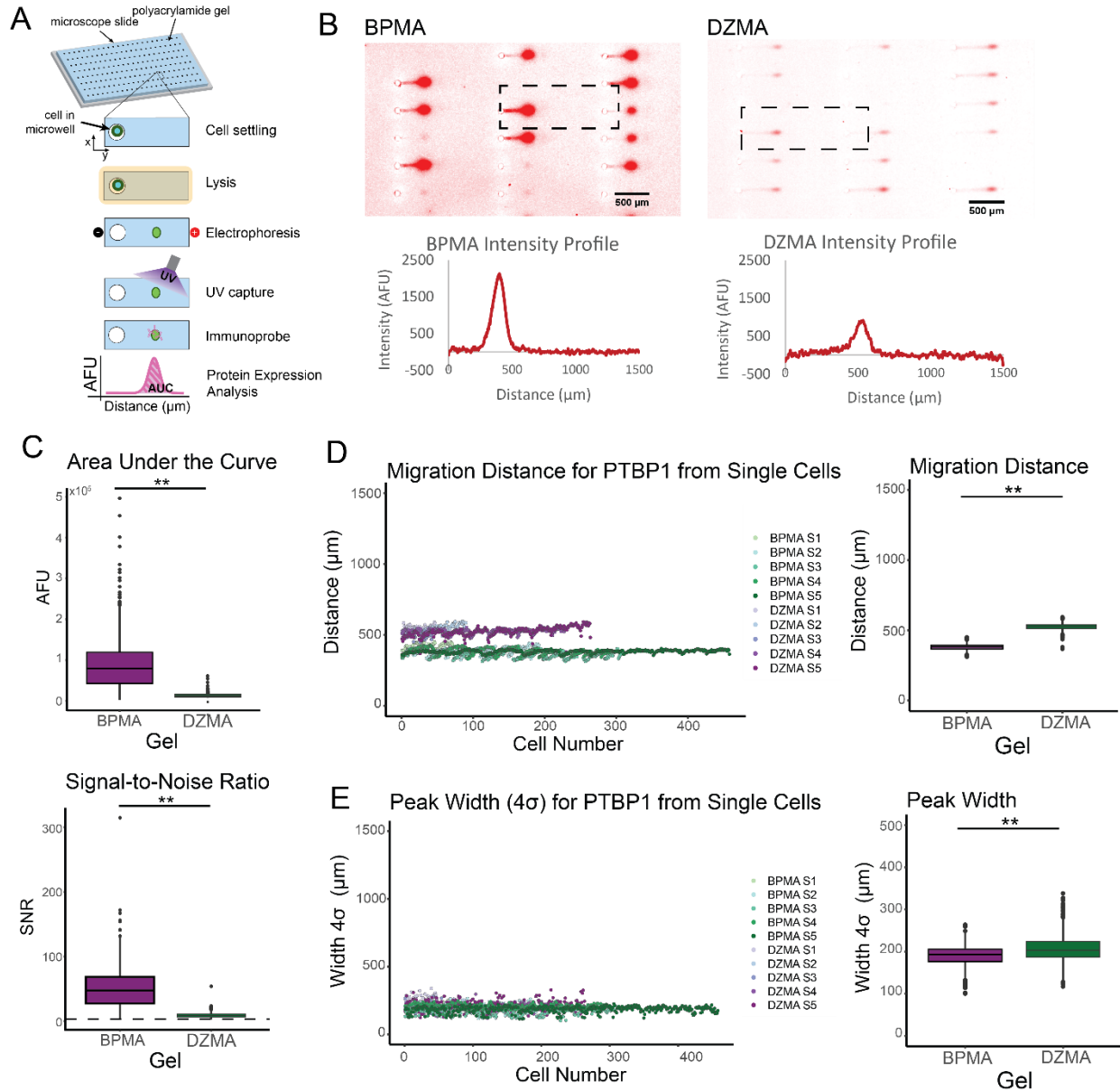


Figure 3-3 Utilizing DZMA hydrogels for single-cell immunoblotting to detect PTBP1 from MDA-MB-231 breast cancer cells

(A) Schematic of single-cell immunoblotting workflow: Single-cells are gravity settled into an array of microwells for subsequent cell lysis and protein solubilization, protein polyacrylamide gel electrophoresis, and in-gel immobilization of separated proteins. Protein targets are immunoprobed with fluorophore-conjugated antibodies. (B) Representative false-color fluorescence micrographs and intensity plots as examples of protein electromigration (PTBP1, 55 kDa) in each gel condition. (C) Analysis of PTBP1 protein area under curve (AUC) signal and SNR following immunoprobing. The AUC and SNR is much higher in BPMA gels indicating higher protein capture efficiency. (D) Analysis of peak migration distance for PTBP1 (57 kDa) in a BPMA gel (purple) and DZMA gel (green) indicating faster protein migration in the diazirine methacrylamide gels. Each dot corresponds to a single-cell and each shade represents a distinct device. (E) Analysis of PTBP1 protein and peak width (4σ) in both gels indicating slightly larger peak width is larger in DZMA gels. $N = 5$ replicate devices per gel, ** $p < 0.01$; Mann-Whitney U Test.

Based on the faster protein electrophoretic mobility in DZMA gels, we posit that DZMA gels have a larger pore size compared to BPMA gels, resulting in faster protein

electromigration. During the hydrogel fabrication, DZMA gels took longer (1.5 hours) to polymerize than the BPMA gels (15-20 min). We hypothesize that the slower polymerization rate of the DZMA gels indicates that the higher concentration of diazirine acting as a carbon radical trap that inhibits the complete gel polymerization reaction and results in larger pore sizes in the final hydrogel matrix. To test gel pore size, we measured the gel equilibrium swelling ratio of each functionalized hydrogel compared to a negative control gel in deionized water (Figure 3-4A) and found that DZMA gels had significantly greater swelling compared to both BPMA and the negative control gel ($p < 0.01$ Kruskal-Wallis, Holm correction). Because gel swelling depends on both the pore size as well as any interactions between the hydrogel matrix and solvent²⁸, we also measured the swelling ratio in a more polar solvent of 70% isopropyl alcohol (IPA) to better assess hydrogel hydrophobicity²⁹ (Figure 3-4B). However, as polyacrylamide is a hydrophilic polymer, the swelling ratios in 70% IPA were not significantly different between diazirine and BPMA gels. Thus, the significantly higher swelling ratios of DZMA gels in water compared to BPMA hydrogels are more likely to indicate a larger pore size.

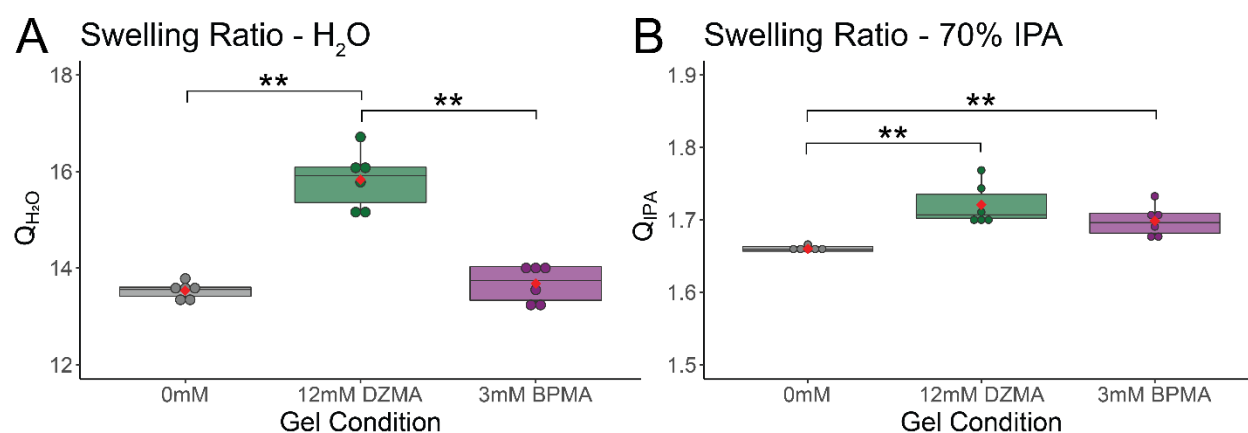


Figure 3-4 Swelling ratios (Q) of 0 mM, 12mM DZMA hydrogels and 3 mM BPMA hydrogels in a polar solvent, water (A) and nonpolar solvent 70% IPA (B).

(A) 12 mM DZMA gels had significantly higher swelling ratio in water compared to both 3 mM BPMA and the 0mM negative control. (B) Both 12 mM DZMA and 3 mM BPMA had significantly higher swelling ratios than the 0 mM negative control, but there was no significant difference between 12 mM DZMA and 3 mM BPMA gels. ** $p < 0.01$; Kruskal-Wallis with Holm multiple pairwise correction.

The lower signal following electrophoretic separations is unexpected when compared to the earlier protein incubation experiments. We investigated how the denatured protein structure would influence protein capture efficiency. Previously, it has been observed that benzophenone protein capture efficiency was significantly higher with denatured protein compared to native protein likely due to greater exposure of hydrophobic residues that favor interaction with benzophenone³⁰. Given the lower hydrophobicity of diazirine, the increased exposure of protein hydrophobic residues may result in less interaction with the diazirine molecule. To investigate the effect of protein structure, we ran native separations with purified protein diluted in 1x PBS and 1x Tris-glycine run buffer (non-denaturing conditions) and still observed higher AUC and SNR in 3mM BPMA gels compared to 12 mM DZMA gels (Figure 3-5). Thus indicating that the denatured protein structure does not account for the difference in protein capture observed between the two experimental systems.

We hypothesize that larger gel pore size results in faster diffusion of protein loss out of the gel. Greater diffusional losses combined with the lower reaction efficiency of diazirine

could explain the lower protein signal observed with single-cell immunoblotting and requires further investigation to validate.

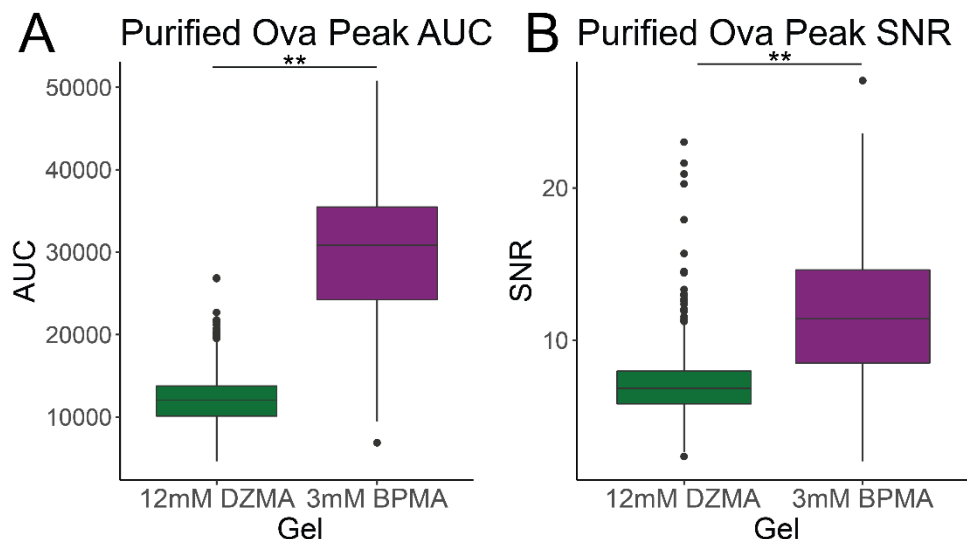


Figure 3-5 AUC and SNR analysis of purified labelled ovalbumin after native microscale separations using 1x Tris-glycine run buffer.

Both AUC and SNR are much higher in BPMA gels indicating higher protein capture efficiency even in non-denaturing conditions. N = 3 devices per gel condition, ** p < 0.01; Mann-Whitney U Test.

3.4 Conclusions and Future Directions

While photoactivatable protein crosslinking molecules are a critical way to enable hydrogels as immunoassay substrates, they can be sources of background fluorescence that impair immunoassay sensitivity. Here, we have determined that diazirine, which lacks conjugated double bonds, has significantly lower non-specific non-covalent interactions with fluorescent immunoprobes and significantly lower autofluorescence compared to benzophenone, resulting in overall lower in-gel immunoassay background signal in DZMA hydrogels compared to BPMA-based hydrogels. However, when DZMA hydrogels were used for single-cell immunoblotting, the alternative diazirine chemistry resulted in faster protein electromigration and lower protein capture following the electrophoretic separations compared to BPMA gels, even though a higher concentration of diazirine capture molecules was utilized. Furthermore, increasing the concentration of DZMA appears to interfere with polyacrylamide gel polymerization reaction, increasing polymerization completion times and affecting the gel pore size. We conclude that while diazirine has lower background signal, the lower capture efficiency and larger pore size of diazirine-modified hydrogels reduces its utility in open microfluidic systems susceptible to sample losses and does not effectively improve in-gel immunoassay sensitivity to detect low abundance protein targets.

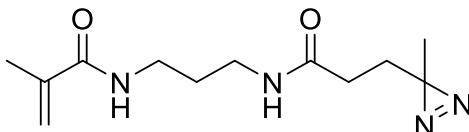
Further investigation into other photoreactive molecules with higher protein capture efficiency than diazirines and lower background fluorescence than benzophenone may be of interest to functionalize hydrogels as immunoassay substrates. For example, aryl azides are another alternative photoreactive molecule used for protein crosslinking. Upon UV activation, aryl azides generate a reactive nitrene species that reacts with nearby C-H and heteroatom-H bonds to

form covalently bound products. The absorption maximum of aryl azides is 250 nm, within the protein-damaging wavelength range, however substituted aryl azides can have higher absorption maximums³¹. Furthermore, the singular aromatic ring on aryl azides may reduce the hydrophobicity and autofluorescence compared to the double aromatic rings on benzophenone.

3.5 Appendix

A1 Synthesis of Diazirine Methacrylamide

Actual IUPAC name: N-(3-(3-(3-methyl-3H-diazirin-3-yl)propanamido)propyl)methacrylamide



Diazirine Methacrylamide

Chemical Formula: C₁₂H₂₀N₄O₂

Molecular Weight: 252.32

Materials: NHS-diazirine (26167), Triethylamine (25108) and Dimethylformamide (20673) were purchased from Thermo Fisher Scientific. N-(3-Aminopropyl)methacrylamide hydrochloride (21200) was purchased from Polysciences. All commercially purchased materials were used without further purification unless stated otherwise. Bruker 400MHz Spectrometer was used for NMR analysis.

Procedure: A 250 mL, round bottom flask was equipped with a magnetic stir bar and charged with N-(3-Aminopropyl)methacrylamide hydrochloride (29.2 mmol, 1.0 eq.), DMF (80 mL) and triethylamine (32.2 mmol, 1.1 eq.) under N₂ atmosphere. NHS-diazirine (29.2 mmol, 1.0 eq) was added and reaction was stirred for 18-24 hours under N₂ at ambient temperature. Solids were removed by filtration and the filtrate was concentrated using a rotary evaporator. The concentrate was dissolved in dichloromethane (200 mL), washed with H₂O (2 x 100 mL), brine (2 x 100 mL) and dried over MgSO₄. The solvent was evaporated and the crude product was triturated using heptane (100 mL). Solids were filtered and dried in a vacuum oven overnight at 50 °C giving a white solid in 85% yield (99% purity via quantitative ¹H NMR using an internal standard (DIB, Diiodobenzene)).

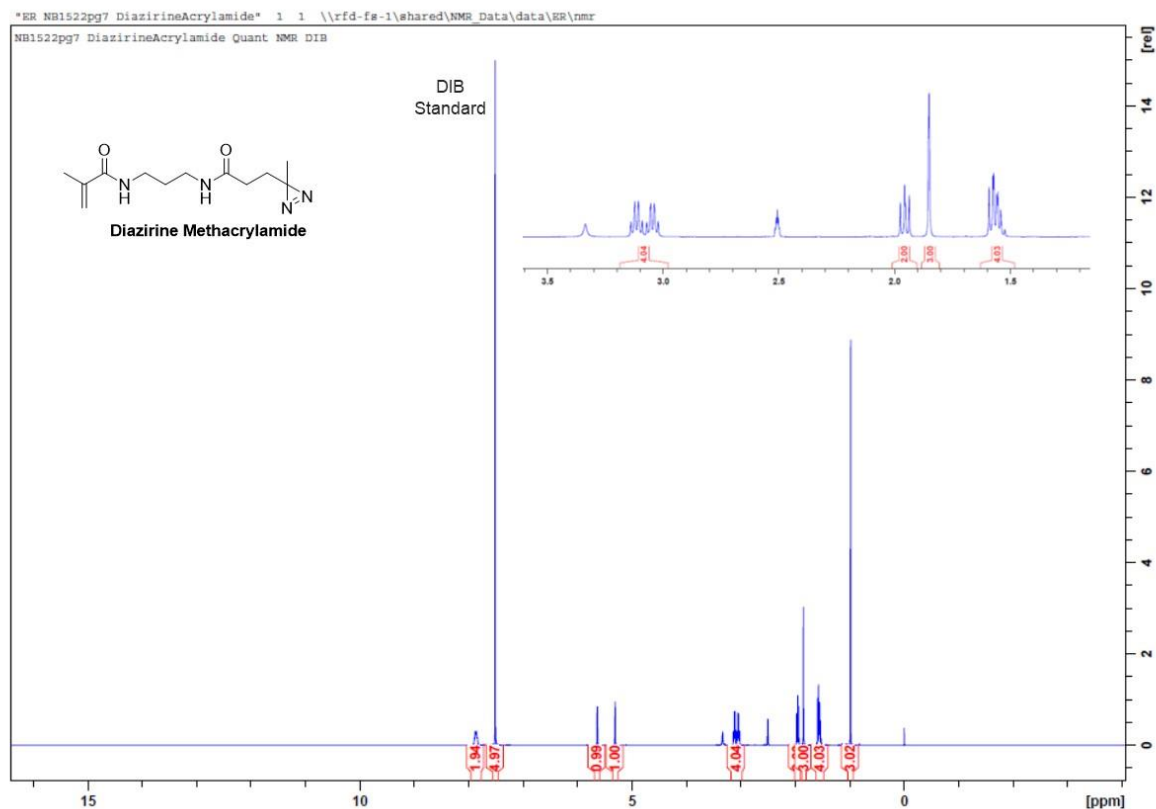


Figure 3-6: Confirmation of diazirine identity and purity.

^1H NMR (DMSO- d_6 , 400 MHz): 7.8 (m, 2H), 5.7 (s, 1H), 5.3 (s, 1H), 3.15 (q, $J = 4$ Hz, 2H), 3.05 (q, $J = 4$ Hz, 2H), 1.95 (t, $J = 4$ Hz, 2H), 1.85 (s, 3H), 1.55 (m, 4H), 1.00 (s, 3H).

3.6 References

- (1) Gupta, M. K.; Martin, J. R.; Dollinger, B. R.; Hattaway, M. E.; Duvall, C. L. Thermogelling, ABC Triblock Copolymer Platform for Resorbable Hydrogels with Tunable, Degradation-Mediated Drug Release. *Adv. Funct. Mater.* **2017**, *27* (47), 1–14. <https://doi.org/10.1002/adfm.201704107>.
- (2) Negishi, R.; Iwata, R.; Tanaka, T.; Kisailus, D.; Maeda, Y.; Matsunaga, T.; Yoshino, T. Gel-Based Cell Manipulation Method for Isolation and Genotyping of Single-Adherent Cells. *Analyst* **2019**, *144* (3), 990–996. <https://doi.org/10.1039/c8an01456f>.
- (3) Batalov, I.; Stevens, K. R.; DeForest, C. A. Photopatterned Biomolecule Immobilization to Guide Three-Dimensional Cell Fate in Natural Protein-Based Hydrogels. *Proc. Natl. Acad. Sci. U. S. A.* **2021**, *118* (4). <https://doi.org/10.1073/pnas.2014194118>.
- (4) Ling, Y.; Rubin, J.; Deng, Y.; Huang, C.; Demirci, U.; Karp, J. M.; Khademhosseini, A. A Cell-Laden Microfluidic Hydrogel. *Lab Chip* **2007**, *7* (6), 756–762. <https://doi.org/10.1039/b615486g>.
- (5) Le Goff, G. C.; Srinivas, R. L.; Hill, W. A.; Doyle, P. S. Hydrogel Microparticles for Biosensing. *Eur. Polym. J.* **2015**, *72*, 386–412. <https://doi.org/10.1016/j.eurpolymj.2015.02.022>.

- (6) Dementieva, E. I.; Rubina, A. Y.; Darii, E. L.; Dyukova, V. I.; Zasedatelev, A. S.; Osipova, T. V.; Ryabykh, T. P.; Baryshnikov, A. Y.; Mirzabekov, A. D. Protein Microchips in Quantitative Assays for Tumor Markers. *Dokl. Biochem. Biophys.* **2004**, 395 (1–6), 88–92. <https://doi.org/10.1023/B:DOBI.0000025553.98757.be>.
- (7) Brambilla, D.; Chiari, M.; Gori, A.; Cretich, M. Towards Precision Medicine: The Role and Potential of Protein and Peptide Microarrays. *Analyst* **2019**, 144 (18), 5353–5367. <https://doi.org/10.1039/c9an01142k>.
- (8) Sharafeldin, M.; McCaffrey, K.; Rusling, J. F. Influence of Antibody Immobilization Strategy on Carbon Electrode Immunoarrays. *Analyst* **2019**, 144 (17), 5108–5116. <https://doi.org/10.1039/c9an01093a>.
- (9) Zubtsov, D. A.; Savvateeva, E. N.; Rubina, A. Y.; Pan'kov, S. V.; Konovalova, E. V.; Moiseeva, O. V.; Chechetkin, V. R.; Zasedatelev, A. S. Comparison of Surface and Hydrogel-Based Protein Microchips. *Anal. Biochem.* **2007**, 368 (2), 205–213. <https://doi.org/10.1016/j.ab.2007.04.040>.
- (10) Hughes, A. J.; Lin, R. K. C.; Peehl, D. M.; Herr, A. E. Microfluidic Integration for Automated Targeted Proteomic Assays. *Proc. Natl. Acad. Sci.* **2012**, 109 (16), 5972–5977. <https://doi.org/10.1073/pnas.1108617109>.
- (11) Dormán, G.; Nakamura, H.; Pulsipher, A.; Prestwich, G. D. The Life of Pi Star: Exploring the Exciting and Forbidden Worlds of the Benzophenone Photophore. *Chem. Rev.* **2016**, 116 (24), 15284–15398. <https://doi.org/10.1021/acs.chemrev.6b00342>.
- (12) Hughes, A. J.; Spelke, D. P.; Xu, Z.; Kang, C.-C.; Schaffer, D. V.; Herr, A. E. Single-Cell Western Blotting. *Nat. Methods* **2014**, 11 (7), 749–755. <https://doi.org/10.1038/nmeth.2992>.
- (13) Schneider, M. H.; Tran, Y.; Tabeling, P. Benzophenone Absorption and Diffusion in Poly(Dimethylsiloxane) and Its Role in Graft Photo-Polymerization for Surface Modification. *Langmuir* **2011**, 27 (3), 1232–1240. <https://doi.org/10.1021/la103345k>.
- (14) Dormán, G.; Nakamura, H.; Pulsipher, A.; Prestwich, G. D. The Life of Pi Star: Exploring the Exciting and Forbidden Worlds of the Benzophenone Photophore. *Chemical Reviews*. 2016, pp 15284–15398. <https://doi.org/10.1021/acs.chemrev.6b00342>.
- (15) Su, A.; Smith, B. E.; Herr, A. E. In Situ Measurement of Thermodynamic Partitioning in Open Hydrogels. *Anal. Chem.* **2019**, 92 (2), 875–883. <https://doi.org/10.1021/acs.analchem.9b03582>.
- (16) CSID:10629329 <http://www.chemspider.com/Chemical-Structure.10629329.html> (accessed Jun 20, 2021).
- (17) CSID:2991 <http://www.chemspider.com/Chemical-Structure.2991.html> (accessed Jun 20, 2021).
- (18) Brunner, J.; Senn, H.; Richards, F. M. 3-Trifluoromethyl-3-Phenyldiazirine. A New Carbene Generating Group for Photolabeling Reagents. *J. Biol. Chem.* **1980**, 255 (8), 3313–3318. [https://doi.org/10.1016/s0021-9258\(19\)85701-0](https://doi.org/10.1016/s0021-9258(19)85701-0).
- (19) Tanaka, Y.; Bond, M. R.; Kohler, J. J. Photocrosslinkers Illuminate Interactions in Living Cells. *Mol. Biosyst.* **2008**, 4 (6), 473–480. <https://doi.org/10.1039/b803218a>.
- (20) A. Fleming, S. Chemical Reagents in Photoaffinity Labeling. *Tetrahedron* **1995**,

- 51 (46), 12479–12520. [https://doi.org/10.1016/0040-4020\(95\)00598-3](https://doi.org/10.1016/0040-4020(95)00598-3).
- (21) Kang, C.-C.; Yamauchi, K. A.; Vlassakis, J.; Sinkala, E.; Duncombe, T. A.; Herr, A. E. Single Cell–Resolution Western Blotting. *Nat. Protoc.* **2016**, *11* (8), 1508–1530. <https://doi.org/10.1038/nprot.2016.089>.
- (22) Gopal, A.; Herr, A. E. Multiplexed In-Gel Microfluidic Immunoassays: Characterizing Protein Target Loss during Reprobing of Benzophenone-Modified Hydrogels. *Sci. Rep.* **2019**, *9* (1), 1–12. <https://doi.org/10.1038/s41598-019-51849-8>.
- (23) Rueden, C. T.; Schindelin, J.; Hiner, M. C.; DeZonia, B. E.; Walter, A. E.; Arena, E. T.; Eliceiri, K. W. ImageJ2: ImageJ for the next Generation of Scientific Image Data. *BMC Bioinformatics* **2017**, *18* (1), 1–26. <https://doi.org/10.1186/s12859-017-1934-z>.
- (24) Schindelin, J.; Arganda-Carreras, I.; Frise, E.; Kaynig, V.; Longair, M.; Pietzsch, T.; Preibisch, S.; Rueden, C.; Saalfeld, S.; Schmid, B.; et al. Fiji: An Open-Source Platform for Biological-Image Analysis. *Nature Methods*. Nature Publishing Group July 28, 2012, pp 676–682. <https://doi.org/10.1038/nmeth.2019>.
- (25) Dormán, G.; Prestwich, G. D. Benzophenone Photophores in Biochemistry. *Biochemistry* **1994**, *33* (19), 5661–5673.
- (26) Barton, D. H. R.; Jaszberenyi, J. C.; Theodorakis, E. A.; Reibenspies, J. H. The Invention of Radical Reactions. 30. Diazirines as Carbon Radical Traps. Mechanistic Aspects and Synthetic Applications of a Novel and Efficient Amination Process. *J. Am. Chem. Soc.* **1993**, *115* (18), 8050–8059. <https://doi.org/10.1021/ja00071a017>.
- (27) Zhang, T.; Li, S.; Warden, A. R.; Ghalandari, B.; Li, H.; Zhi, X. A Photoclick Hydrogel for Enhanced Single-Cell Immunoblotting. **2020**, *1910739*, 1–8. <https://doi.org/10.1002/adfm.201910739>.
- (28) Gehrke, S. H.; Fisher, J. P.; Palasis, M.; Lund, M. E. Factors Determining Hydrogel Permeability. *Ann. N. Y. Acad. Sci.* **1997**, *831* (508), 179–207. <https://doi.org/10.1111/j.1749-6632.1997.tb52194.x>.
- (29) Munoz-Pinto, D. J.; Grigoryan, B.; Long, J.; Grunlan, M.; Hahn, M. S. An Approach for Assessing Hydrogel Hydrophobicity. *J. Biomed. Mater. Res. - Part A* **2012**, *100 A* (10), 2855–2860. <https://doi.org/10.1002/jbm.a.34289>.
- (30) Hughes, A. J.; Herr, A. E. Microfluidic Western Blotting. *Proc. Natl. Acad. Sci. U. S. A.* **2012**, *109* (52), 21450–21455. <https://doi.org/10.1073/pnas.1207754110>.
- (31) MacKinnon, A. L.; Taunton, J. Target Identification by Diazirine Photo-Cross-Linking and Click Chemistry. *Curr. Protoc. Chem. Biol.* **2009**, *1* (1), 55–73. <https://doi.org/10.1002/9780470559277.ch090167>.

Chapter 4: Western blotting using an offset electrode configuration during electrotransfer

This work was performed in collaboration with Andoni P. Mourdoukoutas, Amy E. Herr, Krishna Vattam, Brian Webb, Steve Crouse, Paul J. Haney, Kelli D. Feather-Henigan, and Carrie Clothier.

4.1 Introduction

Problem

Conventional western blotting protocols involve multiple hands-on steps that are time consuming. Furthermore, during the blotting step when proteins are transferred from the separation gel to the membrane, there is a risk of over transferring smaller molecular weight species such that they pass through the membrane¹. To address both of these concerns, Thermo Fisher Scientific designed a prototype electrotransfer system with an “offset” electrode configuration that would leverage electrotransfer of protein in both the vertical and lateral dimensions. The offset design has the potential to 1) prevent over transferring smaller-sized species, retaining smaller proteins laterally on the blotting membrane as larger proteins elute from the gel and 2) simplify the conventional western blot workflow by minimizing handling. However, due to the addition of the lateral dimension, non-uniformities arise in electric field and path length, as expected from theory, resulting in performance losses such as lower transfer efficiency, particularly with higher molecular weight targets and protein band dispersion². Thus, we determined the operational regimes and performance losses for gel-to-membrane electrotransfer of separated proteins using an ‘offset electrode configuration’ compared to conventional vertical electrotransfer.

Method

To investigate the impact of electrode placement on the electric field magnitude and electrical current path, we developed a finite element analysis model (COMSOL Multiphysics®) to predict the electric field magnitude and electrical current path in various electrotransfer system designs, and used the results to develop a modeling framework to approximate protein migration velocity (and thus electrotransfer transfer times) as functions of gel density, protein size, and E_z . We then experimentally validated the results of the model using the offset electrode configuration with standard 1 mm thick gels and thin (~100 μm) gels, comparing offset transfer performance to the standard vertical electrotransfer. Due to the losses observed in the offset electrode configuration system, we proposed and modeled alternative electrode designs to increase E_z magnitude and reduce non-uniformity of protein electrotransfer times.

Major Results

In the initial offset electrode configuration (Gen 1.0), modeling results indicated that the E_z magnitude is 10^{-1} - 10^{-4} lower than in conventional electrotransfer, which adversely impacts electrotransfer protein velocities of large molecule weight species in particular. These modeling results were experimentally confirmed, as poor electrotransfer of large molecular weight species was observed in the Gen 1.0 system. As predicted by the models, attempts to increase the E_z magnitude for the large molecular weight species

did not improve elution of larger molecular weight species from the gel. Furthermore, reducing gel thickness by a single order of magnitude did not make up for the $>10^2$ -fold difference in E_z to improve transfer performance. To increase the E_z magnitude, alternative 'offset' electrode assemblies were designed with the following modifications: reduced electrode spacing from 20 mm to 1 mm (Gen 1.1 system), inclusion of multiple anodes with one on either side of the cathode (Gen 2.0 system), and a wire mesh anode placed directly below the cathode (Gen 2.1 system). Investigation of the E_z magnitudes in the alternative systems was performed by modeling analysis: the Gen 1.1 system E_z ranges from 10^{-1} to 10^{-3} , the Gen 2.0 system E_z ranges from 10^{-1} to 10^{-2} , and the Gen 2.1 system E_z ranges from 10^0 to 10^{-1} , compared to conventional electrotransfer E_z magnitudes.

Outcome/Conclusions

The offset electrode configurations resulted in non-uniform, lower E_z magnitude compared to the conventional vertical electrode configuration. The reduced E_z magnitude adversely impacts protein transfer time, as protein migration velocity is linearly related to E_z and this is particularly detrimental for transfer of large molecular weight species. Experimentally, large molecular weight species were not able to transfer and adjustments to increase the electric field were not sufficient to improve transfer performance. Alternative geometries that maintain comparable E_z to the standard vertical electrotransfer geometry, such as the wire mesh electrode directly below the gel, may result in less performance loss during transfer and would require additional experimental investigation to assess efficacy of large molecular weight species transfer in such systems.

4.2 Results and Discussion

Investigation of E_z in Conventional and Gen 1.0 Electrotransfer Systems by Modeling Analysis

To investigate the impact of electrode placement on the electric field magnitude and electrical current path, we developed a finite element analysis model (COMSOL Multiphysics®) to predict the electric field magnitude and electrical current path in various electrotransfer system designs (Figure 4-1). We applied this modeling analysis to a conventional electrotransfer system (Figure 4-1A-C), as well as to an electrotransfer system involving an offset electrode arrangement (Gen 1.0 device; Figure 4-1D-F).

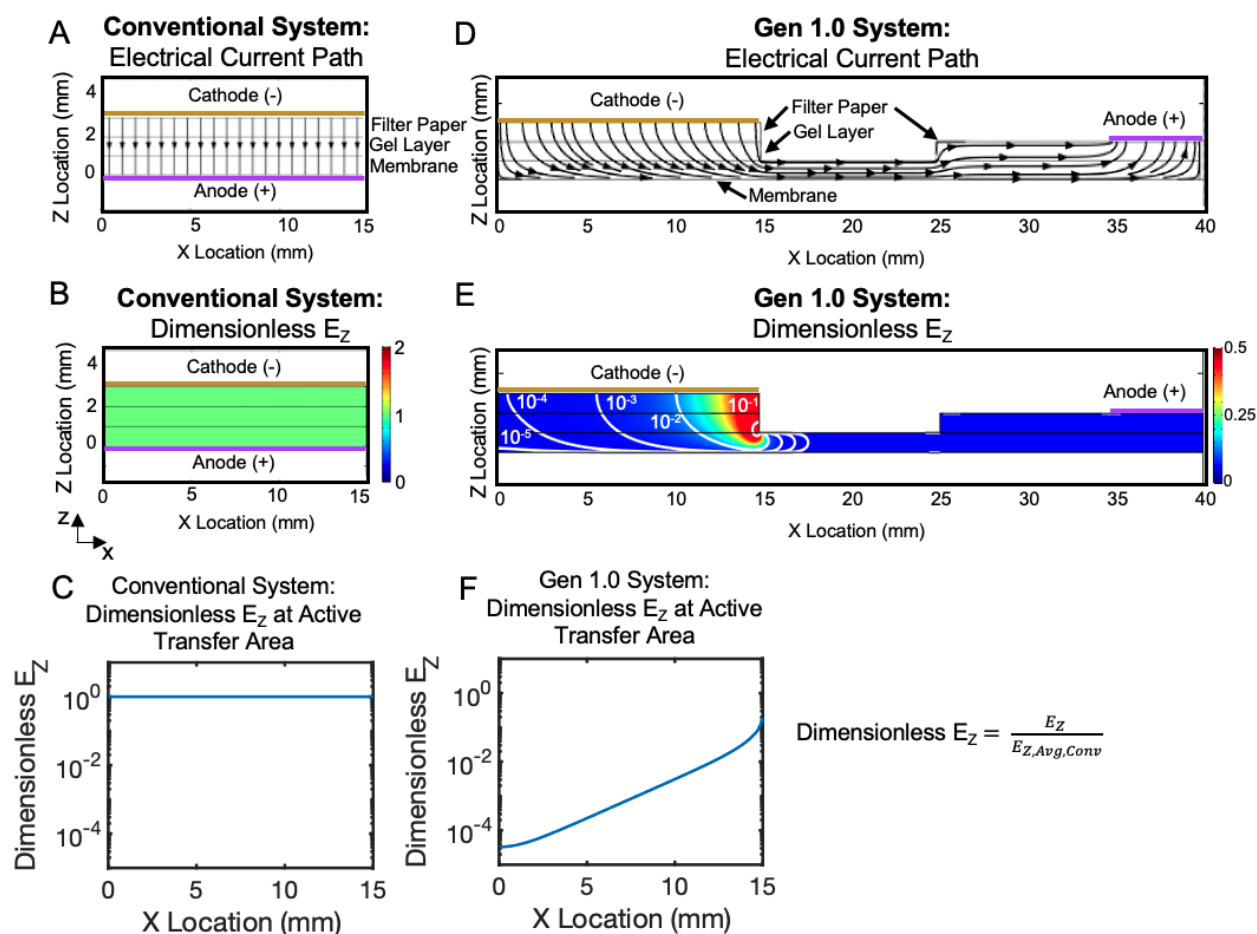


Figure 4-1: Finite element analysis model of electric field magnitude and electrical current path in various electrotransfer system designs.

In the conventional electrotransfer system, (A) the electrical current path is uniform and parallel to the Z-axis and (B) the electric field magnitude in Z, E_z , is uniform throughout the gel. (C) The E_z in the conventional system at the active transfer area is thus also uniform in X. In the Gen 1.0 electrotransfer system, (D) the electrical current path is non-uniform in Z and includes components in X and Z and (E) the E_z is non-uniform throughout the gel. (F) The E_z in the Gen 1.0 system at the active transfer area is non-uniform in X and increases with proximity to the anode (+).

As expected, modeling analysis in the conventional system indicates that current path is parallel to the Z-axis throughout the entire electrotransfer system (Figure 4-1A), and thus the magnitude of electric field that contributes to protein electrotransfer (parallel to the Z-axis, E_z ; V/cm) is uniform throughout the entire electrotransfer system (Figure 4-1). To specifically evaluate the magnitude of E_z in the active protein electrotransfer region in relation to the average magnitude of E_z in the entire electrotransfer system, we plotted a dimensionless E_z at the gel-membrane interface as a function of X-location (Figure 4-1C). The dimensionless E_z is determined by dividing the magnitude of the X-location specific E_z by the average magnitude of E_z in the entire electrotransfer system, facilitating direct comparison of E_z at the active protein electrotransfer region to the average E_z in the system. We observe dimensionless $E_z = 1$ at all X-locations, indicating uniform E_z

magnitude that is additionally equivalent to the average E_z magnitude in the electrotransfer system.

Application of our modeling analysis to the Gen 1.0 device shows that the electrical current path is non-uniform throughout the electrotransfer system and includes components in X and Z dimensions (Figure 4-1D). We additionally find that the E_z magnitude is non-uniform, particularly at the gel-membrane interface (Figure 4-1E). To compare the E_z magnitude in the Gen 1.0 device to the average E_z in the conventional system, we non-dimensionalized the E_z at the gel-membrane interface in the Gen 1.0 device by dividing E_z by the average E_z in the conventional system. The dimensionless E_z is plotted as a function of X-location, showing that the E_z magnitude is 10^{-1} - 10^{-4} lower than in conventional electrotransfer (Figure 4-1F).

Investigation of Protein Electrotransfer Timescale in Gen 1.0 System by Modeling Analysis

Using the results of our electric field modeling analysis, we sought to develop a modeling framework to approximate protein migration velocity (and thus electrotransfer transfer times) as functions of gel density, protein size, and E_z . Protein electromigration velocity (v ; cm/s) is linearly proportional to the electric field strength and the electrophoretic mobility (μ ; $\text{cm}^2/\text{V}\cdot\text{s}$)

$$v = \mu E \quad 4.1$$

The Ferguson relation³ describes protein electromigration in polyacrylamide gel electrophoresis as

$$\mu = 10^{-K_r * \%T} \quad 4.2$$

where K_r is the retardation coefficient, and $\%T$ is the total acrylamide concentration⁴. K_r is related to the size of the protein and the sieving quality of the separation matrix, and follows a linear relationship with molecular weight for most proteins^{3,5}

$$K_r = A + B * MW \quad 4.3$$

where A and B are empirically determined constants that are unique to a particular system. Ultimately, a governing equation for protein velocity that incorporates gel density, protein molecular weight, and electric field strength can be described as

$$\mu = 10^{-(A+B*MW)*\%T} \quad 4.4$$

$$v = E_z * 10^{-(A+B*MW)*\%T} \quad 4.5$$

As approximations of A and B in our system, we accepted values determined in previous studies using similar polyacrylamide gel electrophoresis systems ($A = -0.001$, $B = 2.2 * 10^{-3}$)⁶. To describe protein electromigration velocity in our electrotransfer systems, we can input E_z (from Figure 4-1 modeling analysis) and the range of MW and $\%T$ of interest.

We demonstrate this modeling framework as a tool to relate μ to any combination of MW and %T by plotting the μ for protein targets with MW ranging from 5 to 200 kDa in distinct, uniform %T gels from 4 to 14%T (Figure 4-2A). For protein targets that have undergone electrophoretic separations in a %T gradient gel, protein MW can be spatially encoded across the gradient gel such that a high to low MW distribution overlays a low to high %T gradient; large MW proteins exist in low %T gel regions, and small MW proteins exist in high %T gel regions. To model protein transfer velocity resulting from this combination of non-uniform spatial distributions of MW and %T, we plot protein transfer velocity as a function of a %T gradient gel (4 to 14%T, linearly increasing) and size separated protein MW distribution (200 to 5 kDa, linearly decreasing), considering the electric field profiles in a conventional electrotransfer system, the Gen 1.0 device, and a Gen 1.0 device with

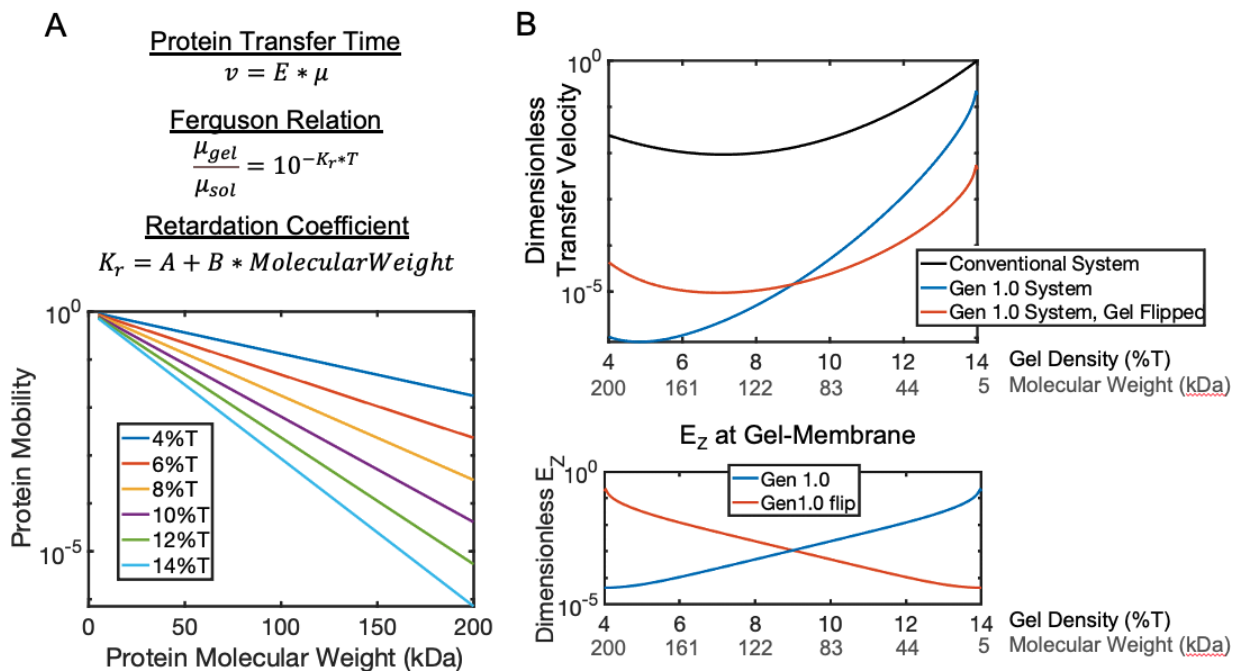


Figure 4-2: Relationship between μ to any combination of MW and %T

(A) Protein transfer time depends on the electric field and protein electrophoretic mobility. Electrophoretic mobility depends on the gel pore size, determined by %T, and the molecule's retardation coefficient which, in a denatured system, scales linearly with protein molecular weight. (B) Taking all these factors into account and modeling the dimensionless transfer time, the transfer time of the largest protein in the offset system (blue line) is 10^{-5} slower than the conventional vertical electrotransfer due to the lower electric field in that region of the gel (blue line). Reversing the orientation such that the higher molecular weight proteins are in the region with highest electric field, in the offset system (orange line), reduces the transfer time, but it is still 10^2 slower transfer than conventional system.

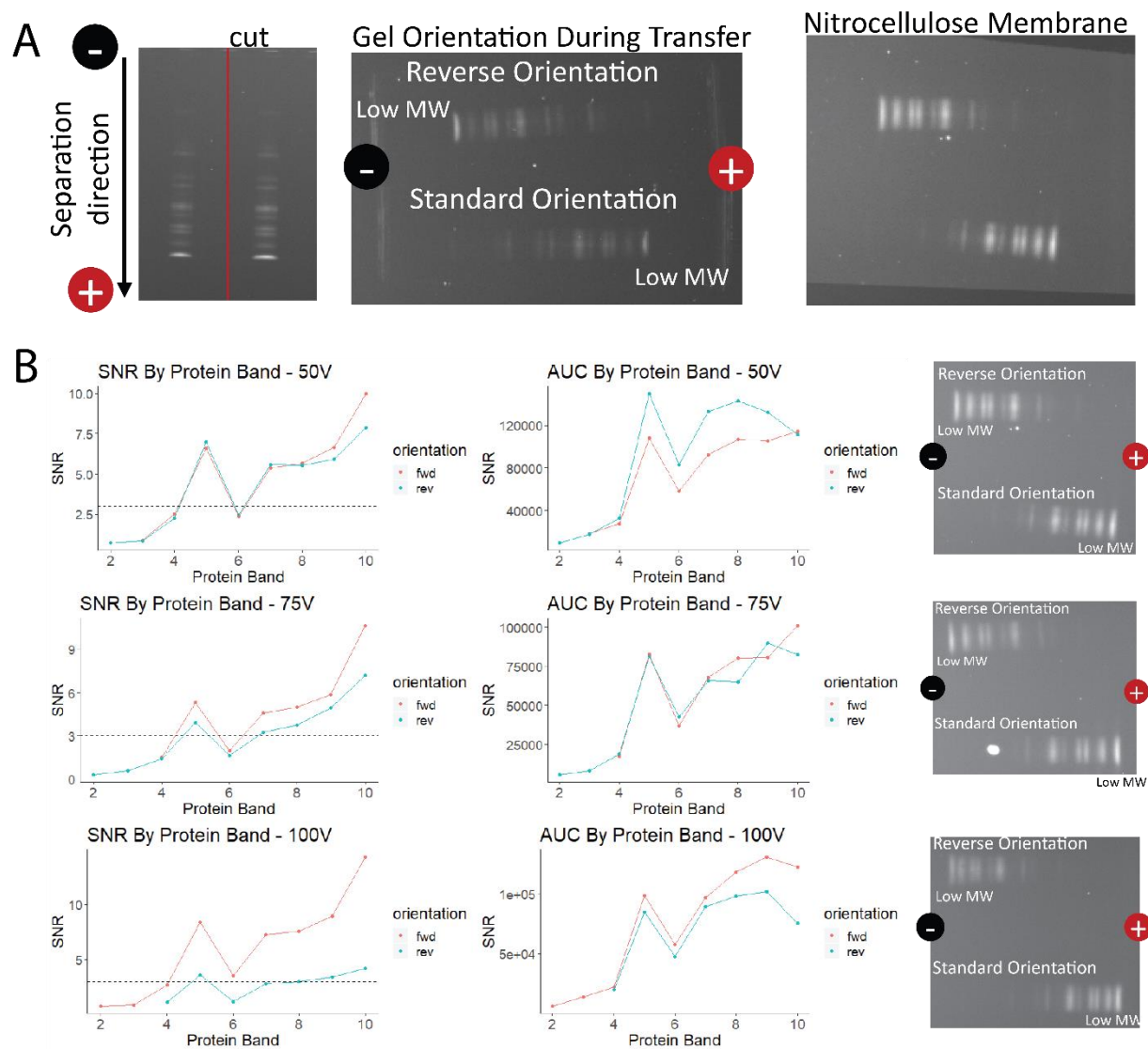
the gel orientation flipped with respect to the electrode arrangement (Figure 4-2B, top). Electric field profiles in the Gen 1.0 and Gen 1.0 with flipped gel orientation are shown in Figure 4-2B, bottom, with respect to the %T and MW distributions. In the conventional electrotransfer system, the electric field is spatially uniform. The transfer velocities are all non-dimensionalized by dividing all the transfer velocities by the fastest moving analyte (a 5 kDa protein in a 14%T gel under the electric field in the conventional electrotransfer system). We thus developed an analytical model to approximate protein transfer velocity

as functions of gel %T, protein MW and applied E_z . We applied this framework to determine transfer velocities of size separated proteins in a gradient gel with three different electrotransfer systems; a conventional system, the Gen 1.0 device, and a Gen 1.0 device with a flipped gel orientation. In the Gen 1.0 system, protein transfer velocities were 10^{-1} to 10^{-4} slower than in the conventional system. In the Gen 1.0 system with the gel orientation flipped, protein transfer velocities were 10^{-1} to 10^{-3} slower than in the conventional system. Our modeling analysis indicates that the Gen 1.0 device is a tool to shape non-uniform spatial distributions of E_z in an electrotransfer system, but adversely impacts protein electrotransfer velocities compared to conventional electrotransfer systems.

Experimental Investigation of Protein Transfer Efficiency using Offset Electrode Configurations

To experimentally validate the simulated models, we tested the offset transfer using standard 1mm-thick gels with standard semi-dry transfer buffer (Figure 4-3A). To improve transfer, we tested 1) increasing voltage to increase E-field and 2) reversing the gel orientation during electrotransfer to place larger molecular weight proteins closer to anode where there is higher magnitude E-field (Figure 4-3B). Based on the linear relationship between electrophoretic mobility and electric field strength, we hypothesize that increasing the electric field will improve transfer of larger MW proteins in the offset transfer geometry compared to the original offset set up.

To test the impact of gel orientation during transfer we ran two samples of iBright Protein Standard ladder via conventional PAGE using a 14%T Tris-glycine gel and 1x Tris-Glycine run buffer. After the separation, the gel was then cut in half, and one separation lane was reversed to have opposite orientation to the other lane. During the offset transfer, there was one lane with the original orientation with larger molecular weight proteins closer to the cathode (weaker E-field) and one lane with reverse orientation with larger molecular weight proteins closer to the anode (stronger E-field). Both gels were transferred to the same nitrocellulose membrane simultaneously using the offset electrode configuration transfer system. Pierce™ 1-Step Transfer Buffer was used for the transfer step. The nitrocellulose membrane was then imaged to compare protein transfer and signal of the two orientations. All gels were run using the same settings for the separation. We tested the reverse orientation at three different voltages during electrotransfer to determine if the combined effect of reverse orientation and higher electric fields would improve transfer. We tested three different voltages: 50V, 75V and 100V and electrodes were spaced 5 cm apart for all 3 conditions for average electric fields of 10 V/cm, 15V/cm and 20 V/cm. The nitrocellulose membranes post-transfer were imaged using the iBright using the same imaging settings (exposure time and optical zoom) and area under the curve and SNR of the proteins bands was quantified (Appendix S1). For analysis, protein band 10 refers to the smallest MW protein, regardless of orientation.



We observed that regardless of orientation, only the lower molecular weight proteins were eluted from the gel and transferred out of the gel to the nitrocellulose membrane. This aligns with the predicted results from the model indicating that the transfer velocity of smaller molecular weight species will always be higher than larger molecular weight species (Figure 4-2B). Furthermore, the relatively small increases in electric field, compared to the orders of magnitude difference in the models, did not substantially improve the detectable ($SNR > 3$) transfer of high molecular weight proteins. We note that faint bands corresponding to larger molecular weight proteins were visible by eye in the

reverse orientation compared to the standard orientation, but none of the additional bands had an SNR >3. This further verifies the modeling that the z-direction mobility of the high MW proteins is not high enough to leave the gel, even in the highest E-fields in the offset system. We also note that the higher voltage condition (100V), did not result in increased dispersion of smaller molecular weight bands as previously observed. there was not dispersion of the lower MW that had been previously observed. We hypothesize that the lower current in the current run (6-9 mA) compared to previous run (30-40 mA). To reduce variation, it will be important to standardize the protocol (e.g. cutting the wicks all to the same size, loading the same volume of buffer, cutting the NC membranes and gels to the same size).

Experimental Investigation of Protein Transfer Efficiency in Thin-Gel Assemblies

We next investigated if reducing gel thickness reduces transfer such that offset transfer of large molecular weight protein is feasible (Figure 4-4). We compared transfer of protein separation from a standard 1 mm thick gel and vertical semi-dry transfer (Figure 4-4A) to a thin-gel separation and offset electrode configuration transfer (Figure 4-4B). Protein transfer time scales linearly with distance and inversely with electric field. Based on the results of the models, the Z-direction electric field in the offset system varies by >10²-fold, however we can only reduce the distance (thickness of the gel) by a factor of 10 (from 1mm thick gels to 100 μm). To perform electrotransfer of protein using thin gels, we first fabricated thin (~125 μm) 8%T fsPAGE gels on top of NetFix (60 μm) to provide mechanical support for handling the gel during transfer. The total thickness of the thin gel was ~185 μm (Appendix S2). Purified BSA protein labeled with Alexa Fluor 555 was run using horizontal fsPAGE (Appendix S2). After running the separation, the blot transfer was run using the offset electrode configuration to transfer both the BSA monomer and dimer to a nitrocellulose membrane. The offset transfer was run for 3 minutes at 75V, with electrodes spaced 5 cm apart (15 V/cm).

We observed that the smaller BSA monomer (66 kDa) was successfully transferred to the nitrocellulose membrane, but the larger BSA dimer (132 kDa) was not. The thin gels do not appear to improve transfer of large molecular weight proteins out of the gel in the offset electrode configuration as the single order of magnitude reduction in transfer distance does not make up for the several orders of magnitude difference in transfer velocity between larger and smaller molecular weight species. Additionally, the post-transfer protein band of the BSA monomer on the nitrocellulose membrane had a greater band width than the protein band in-gel potentially indicating that protein travelled down and laterally from the gel to the membrane.

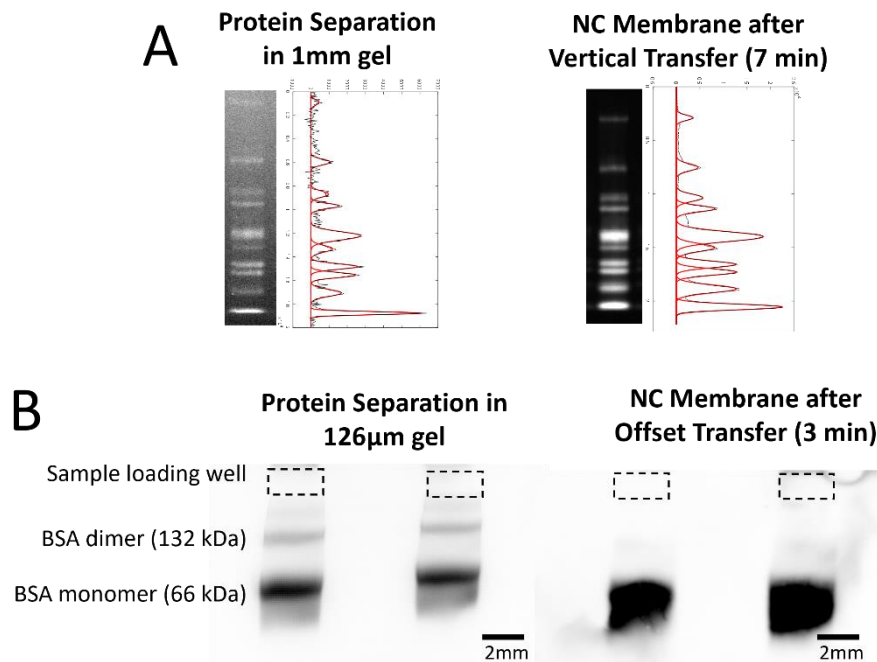


Figure 4-4: Experimental results of using offset electrode configuration to transfer protein out of thin gels

(A, Left) Protein ladder separation in 1mm gel prior to transfer using conventional vertical PAGE tank system. (A, Right) Nitrocellulose membrane post-transfer using standard vertical semi-dry transfer system. (B, Left) Purified protein (BSA monomer and dimer) in gel following fsPAGE horizontal separation using a $\sim 125 \mu\text{m}$ thick gel. (B, Right) Nitrocellulose membrane post-transfer using offset electrode configuration

Investigation of E_z in Gen 1.1 Electrotransfer System by Modeling Analysis

To increase E_z magnitude and reduce non-uniformity of protein electrotransfer times compared to the Gen 1.0 device, we sought to investigate new electrode configurations for reduced voltage loss across active transfer area (gel-membrane boundary). We first sought to increase E_z magnitude by reducing the electrode spacing in the Gen 1.0 system (Gen 1.1 system; Figure 4-5A,B). By reducing the electrode spacing from 20 mm (Gen 1.0) to 1 mm (Gen 1.1), we observe a 10^1 increase in E_z magnitude (Figure 4-5C). While this validates our assumptions of the design rule that minimizing electrode spacing can maximize E_z magnitude, E_z min the Gen 1.1 system is still 10^{-1} to 10^{-3} lower than in the conventional electrotransfer system.

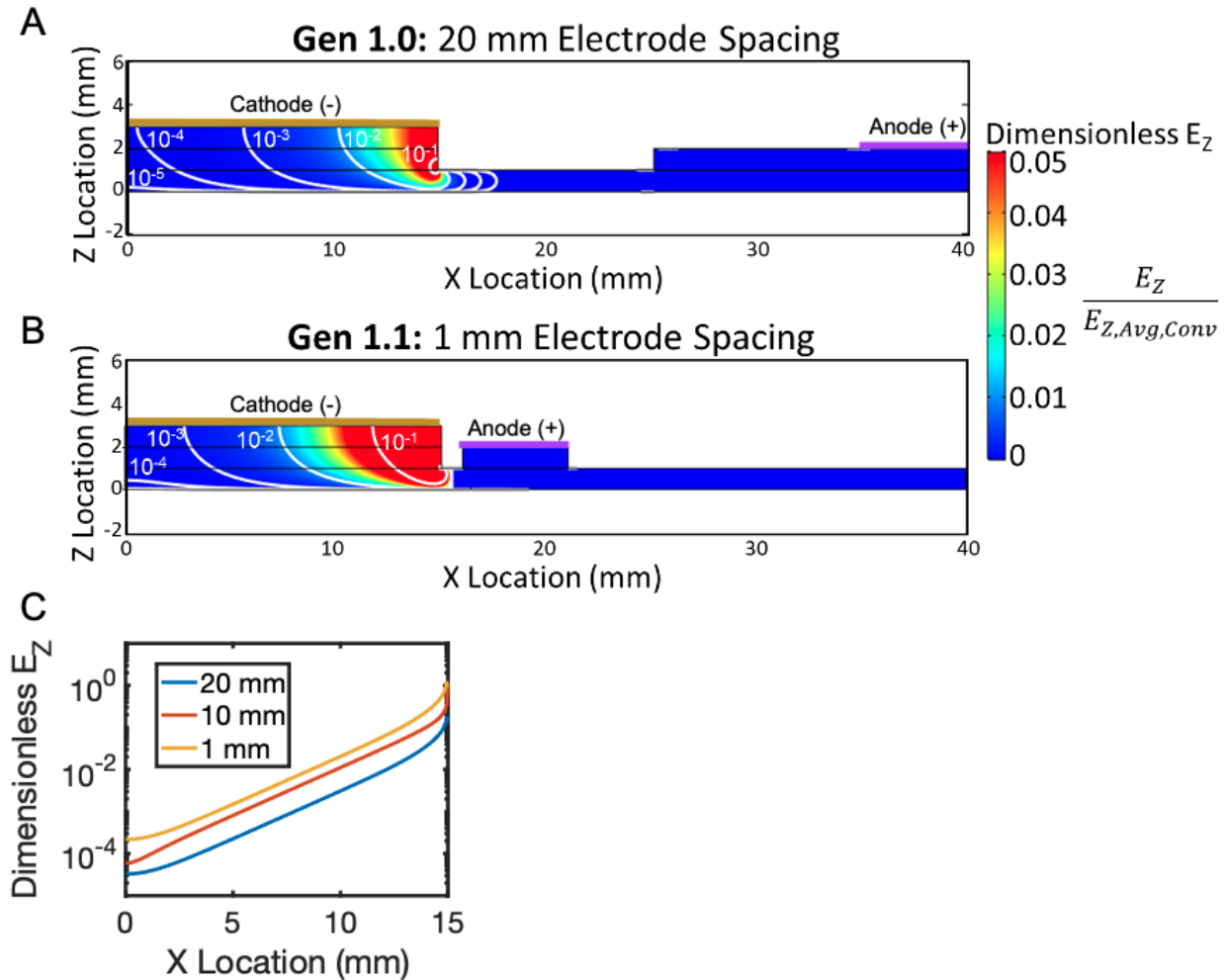


Figure 4-5: Finite element analysis model of electric field magnitude and electrical current path in Gen 1.1 design
 (A,B) The Gen 1.1 electrotransfer system aims to increase E_z magnitude at the active transfer area by reducing spacing between the cathode and anode from 20 mm in the Gen 1.0 system to 1 mm in the Gen 1.1 system. (C) E_z magnitude in the active transfer area is an order of magnitude larger in the Gen 1.1 system than Gen 1.0 system.

Investigation of E_z in Redesigned Gen 2.0 and 2.1 Electrotransfer Systems by Modeling Analysis

We next sought to increase E_z over the active transfer area by using multiple anodes as a method to reduce electrode spacing at both ends of the cathode (Gen 2.0 system; Figure 4-6A,B). In this Gen 2.0 assembly, we use learnings from the Gen 1.1 system to inform the Gen 2.0 electrode separation design and include 1 mm of spacing between cathode edges and each anode. We observe the E_z magnitude at each edge of the cathode in the Gen 2.0 design to be 10^{-1} lower than in the conventional electrotransfer system (Figure 4-6C). This represents an improvement over the Gen 1.1 system, where E_z at the edges of the cathode were 10^{-1} (proximal to lone anode) and 10^{-1} (distal to lone anode) lower than in the conventional electrotransfer system. Additionally, we observe

that in the Gen 2.0 system, the E_z minimum is 10^{-2} lower than the conventional system (instead of 10^{-3} in Gen 1.1) and occurs in the center of the gel.

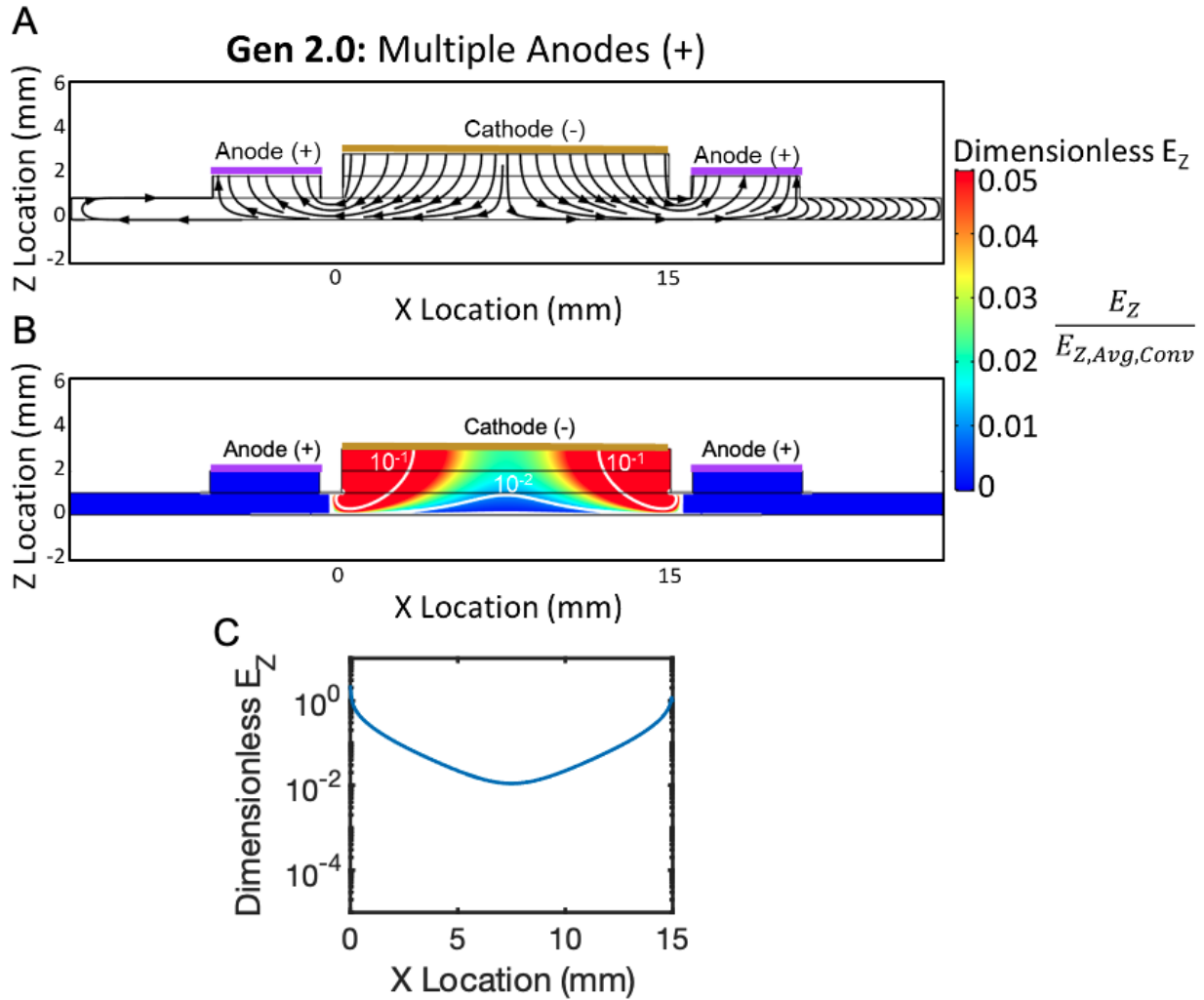


Figure 4-6: Finite element analysis model of electric field magnitude and electrical current path in Gen 2.0 design
 (A,B) The Gen 2.0 system aims to increase E_z magnitude at the active transfer area by including multiple anodes, one on either side of the cathode. (C) E_z magnitude at each edge of the active transfer area is has a value of 10^{-1} , but the gel center has a minimum E_z value of 10^{-2} .

Lastly, we sought to increase E_z over the active transfer area by using a wire electrode mesh placed directly below the electrotransfer assembly (Gen 2.1 system; Figure 4-7A,B). Use of a wire electrode mesh (as opposed to an electrode plate) would permit membrane visualization as well as access of fluid reagents to the membrane (critical for immunoprobings proteins immobilized in membrane) without disassembling the electrode arrangement. Using a wire electrode mesh with 1 mm diameter wires spaced 5 mm apart, we observe minimum E_z values 10^{-1} lower than in conventional systems (Figure 4-7C). The E_z minimums occur at the midpoint between each electrode wire. Maximum E_z values occur directly above each electrode wire and are 10^0 , indicating no difference between the Gen 2.1 system and the conventional electrotransfer systems at these locations. From our modeling analysis, we observe that the E_z magnitude is 10^{-1} to 10^{-4} lower at the active transfer area when using offset electrode assemblies as compared to the conventional electrotransfer system. Reduced magnitude of E_z adversely impacts protein transfer time, as protein migration velocity is linearly related to E_z . Thus, 10^{-1} - 10^{-4} lower

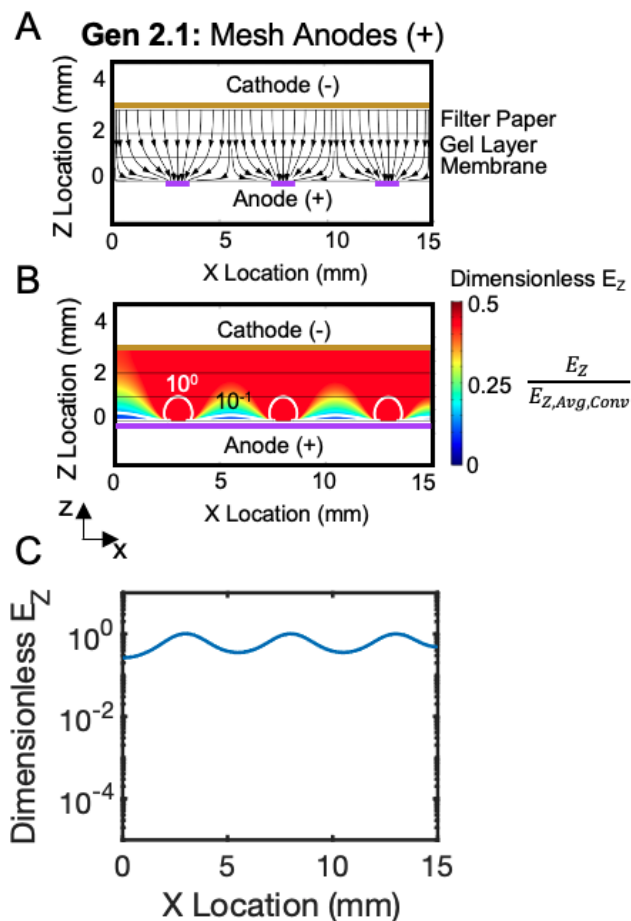


Figure 4-7: Finite element analysis model of electric field magnitude and electrical current path in Gen 2.1 design (A,B) The Gen 2.1 system aims to increase E_z magnitude at the active transfer area by including a mesh of wire electrodes directly below the capture membrane. (C) E_z magnitude is at minimums of 10^{-1} between each wire electrode, and E_z maximums of 10^0 directly above each wire.

E_z magnitude results in 10^1 - 10^4 longer electrotransfer times. The use of a wire mesh electrode introduces maximum E_z values of 10^0 , and minimum E_z values of 10^{-1} . Further investigation of the Gen 2.1 system would be required to determine its compatibility with protein electrotransfer, as limited buffer capacity and introduction of gas products via electrolysis may present additional challenges to protein migration. The results of the E_z magnitudes at the active transfer area for all electrotransfer systems are summarized for direct visual comparison in Figure 4-8.

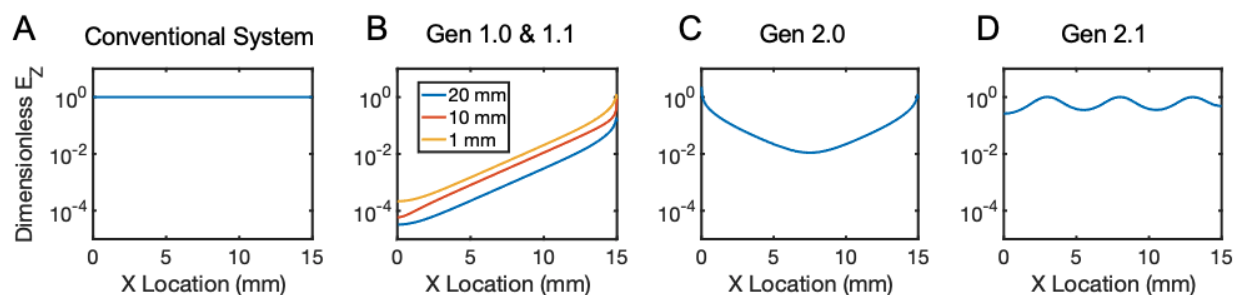


Figure 4-8: Comparison of the E_z magnitude at the active transfer area in all electrotransfer system.

(A) conventional system, (B) Gen 1.0 and Gen 1.1, (C) Gen 2.0, and (D) Gen 2.1.

4.3 Conclusion & Next Steps

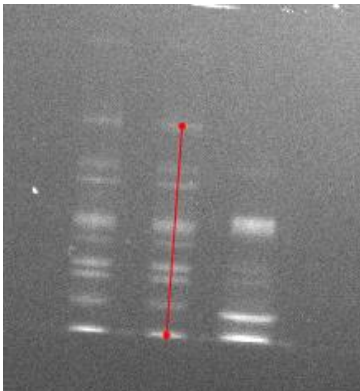
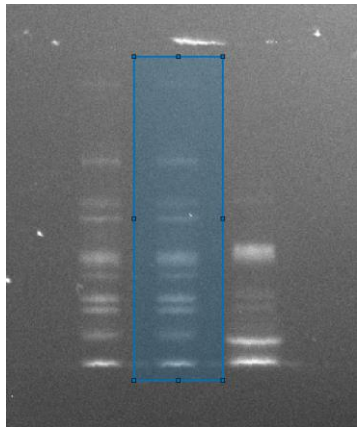
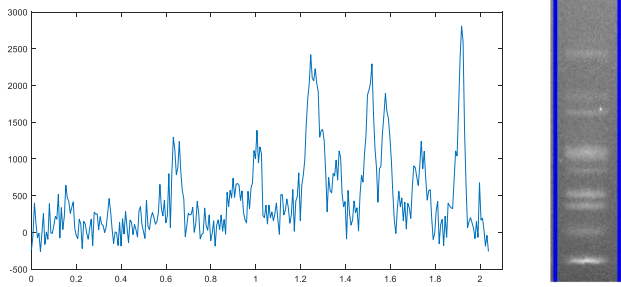
Here, we investigated an offset electrode configuration as a system for gel to membrane protein electrotransfer. Our investigation involved a modeling analysis of the electric field magnitude and electrical current path resulting from electrode placement, and an experimental investigation of protein electrotransfer transfer using the offset electrode arrangements with conventional 1mm and thin ($100\mu\text{m}$) gels. Our modeling analysis indicates that the electric field magnitude is 10^{-1} to 10^{-3} lower than in conventional electrotransfer systems, presenting a challenge to electrotransfer of large molecular weight proteins in the offset electrode system. The results of the modeling analysis are supported by our experimental investigation of protein electrotransfer, as we observed poor electrotransfer of large molecular weight species in the offset electrotransfer system (compared to conventional electrotransfer system) regardless of gel thickness. To mitigate voltage loss across active electrotransfer areas, we investigated the design of Gen 2.0 electrotransfer systems with alternative electrode configurations via a modeling analysis of the electric field magnitude and electrical current path in the Gen 2.0 systems.

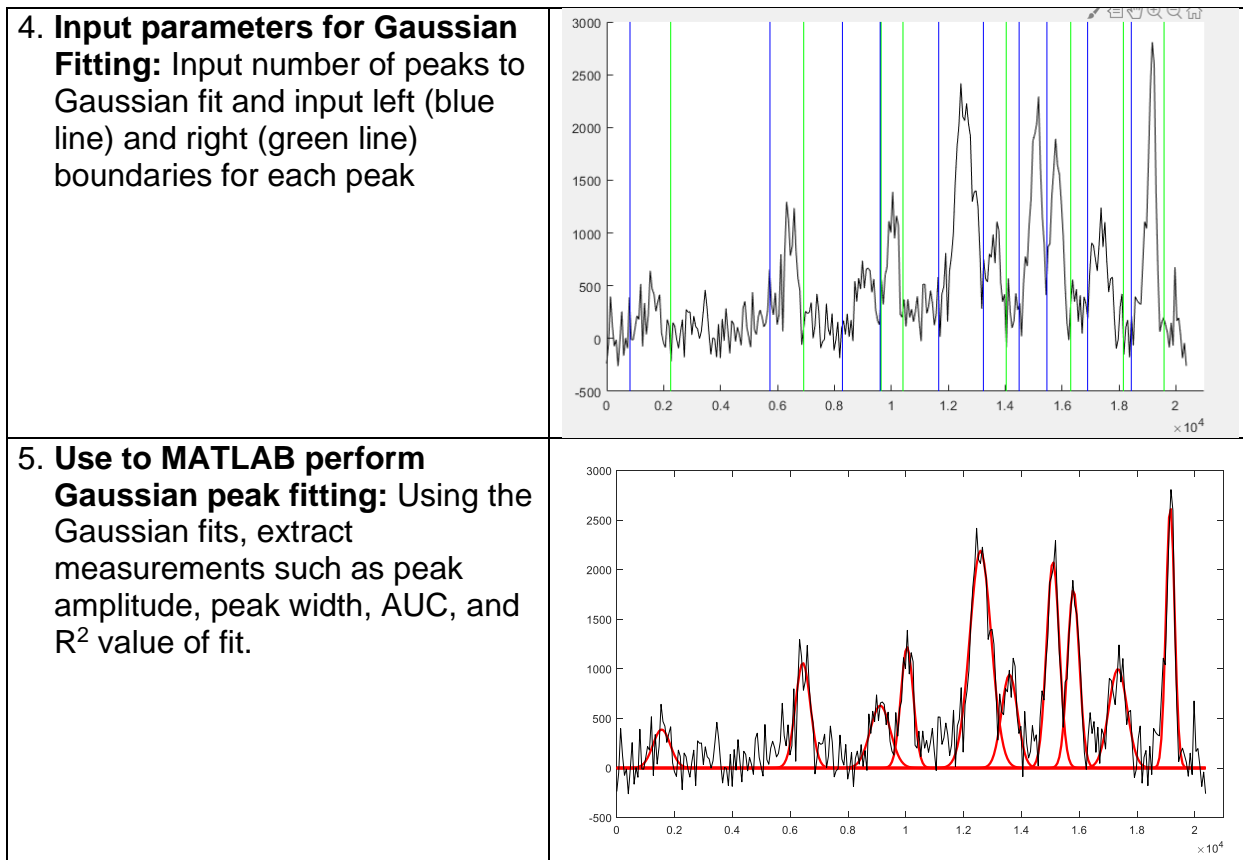
Our proposed next steps for this study involve continuing the investigation of Gen 2.0 electrotransfer systems beyond the initial modeling analysis. Specifically, we propose (i) investigation of the physical assembly of proposed Gen 2.0 electrotransfer systems and (ii) experimental investigation of gel to membrane protein electrotransfer in Gen 2.0 electrotransfer systems. We propose that the experimental investigation of gel to membrane protein electrotransfer in Gen 2.0 systems would be performed in thin ($\sim 100\mu\text{m}$ thick) gels using NetFix as a gel support material, and would include an analysis of protein dispersion during electrotransfer. Additional challenges to using thin gel systems include limited buffering capacity of the electrotransfer system. Conception of Gen 2.0

systems with sufficient buffering capacity during minimum electrotransfer time required for protein elution would thus be an additional next step.

4.4 Appendix

S1 MATLAB Image analysis script to quantify AUC and SNR from gels and nitrocellulose membranes imaged on the iBright

<p>1. Rotate and Align the Image: Import raw TIFF image into MATLAB. Select the middle of band near the top and bottom to draw a reference line to rotate the image to the straight.</p>	
<p>2. Select ROI: Manually draw box around lane to analyze.</p>	
<p>3. Generate Intensity Profile: Background subtraction performed using a gutter region on the left and right (blue lines). Then an average intensity profile is generated for peak fitting</p>	



S2 NetFix Gel Fabrication and fsPAGE protocol (adapted from T. A. Duncombe and A. E. Herr, Lab on a Chip, 2013)

To perform offset transfer with thin gels, we fabricated thin gels with NetFix to perform fsPAGE separation and then offset transfer. The fsPAGE separation system⁷ typically utilizes thin gels (100-200 μm tall) fabricated on a glass slide to perform horizontal protein separations. Here, we have adapted the system, fabricating thin gels on NetFix to run the horizontal protein separation.

NetFix Thin Gel Fabrication process:

First to adhere the NetFix to the glass slide, a ~20 μL drop of gel precursor solution (before adding APS and TEMED) was pipetted onto the glass slide and a Western Blot Roller was used to roll across the NetFix to adhere the NetFix to the glass slide and remove any bubbles. TEMED and APS were added to the remaining gel precursor before it was pipetted onto the SU-8 wafer mold. Then the glass slide with NetFix was placed on top of the wafer, with the NetFix side face down, to sandwich the gel precursor in between the

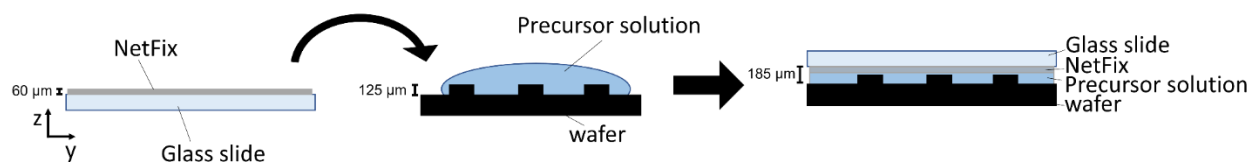



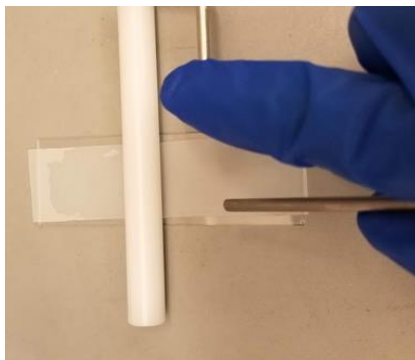
Figure 4-9: Schematic of step-by-step NetFix gel fabrication.

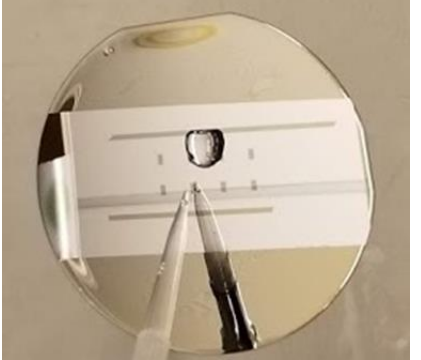
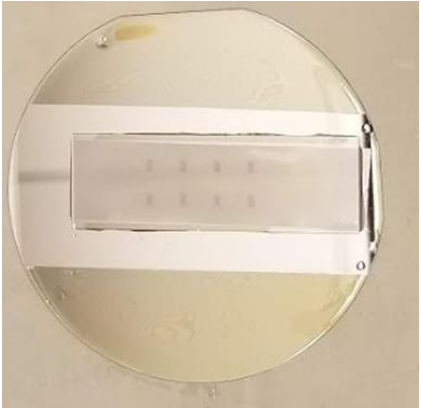
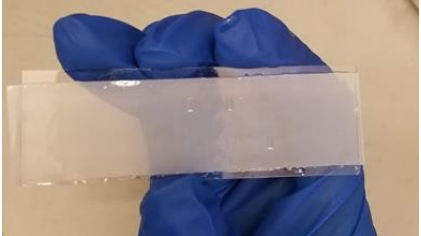
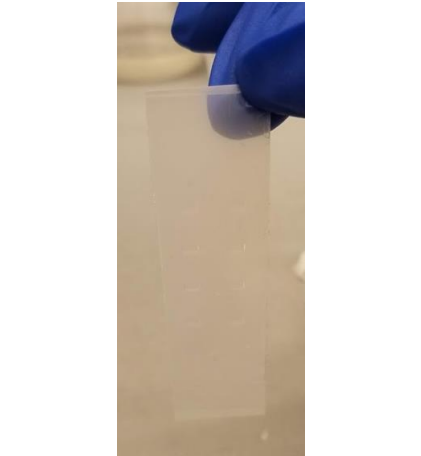
wafer and glass slide (**Error! Reference source not found.**). The NetFix sits on top of the SU-8 wafer posts that form the sample wells in the gel. NetFix add about 60 μm to the total gel thickness, which is primarily determined by the height of the SU-8 wafer features. Gels were polymerized for 20 minutes before lifting off of the wafer. With the NetFix support, gels can be removed from the glass slide to be free standing and easily handled without breaking. Gels were incubated in fsPAGE run buffer solution until sample loading and electrophoresis.

For standard fsPAGE, the run buffer is a 1x Tris-Glycine solution with 10% glycerol and 0.5% Triton X-100⁷. A purified protein solution containing 3 μM BSA-AF555 was prepared in the fsPAGE run buffer.

To perform the fsPAGE separation, the NetFix gel was gently dried with Kimwipe to remove excess buffer before being placed on a dry glass slide which provided a uniform flat surface. Serva electrode wicks were cut in half and pre-soaked in fsPAGE run buffer before being attached to carbon electrodes using rubber bands. The wicks were gently blotted on a Kimwipe to remove excess buffer before the carbon electrodes (with wicks facing downward toward the gel surface) were placed on the surface of the gel, 3 cm apart. Then 0.3-0.5 μL of protein solution was loaded into each well. The separation was run for 3 min at 300V (100V/cm) and protein migrated laterally through the gel. After separation, the electrophoresis chamber was disassembled and the NetFix gel was removed from the glass slide and transferred to the offset electrode configuration transfer system.

Detailed fsPAGE protocol

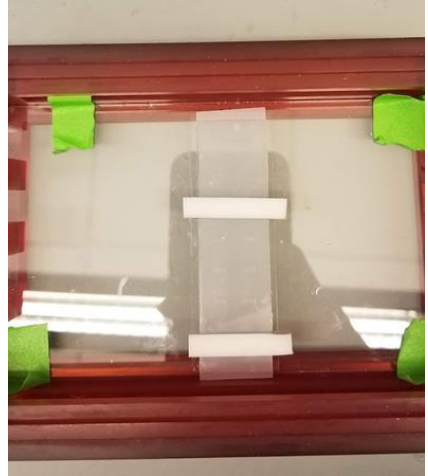
<p>1. Place NetFix on top of a drop of gel precursor on a clean unsilanized glass slide</p>	
<p>2. Use a Western blot roller to remove any air bubbles from the NetFix membrane and gel precursor solution</p>	

<p>3. Add TEMED and APS to remaining gel precursor and pipette ~250 μL on SU-8 wafer with posts. Be sure to treat SU-8 wafer with gel slick before gel fabrication so prevent gel from sticking to wafer.</p>	
<p>4. Place NetFix slide on top of gel precursor to sandwich (NetFix side facing the wafer). Let gel polymerize for ~15-20 minutes</p>	
<p>5. After gel polymerization, lift slide with polymerized gel off of wafer</p>	
<p>6. Gently peel the NetFix-gel off of the glass slide</p>	

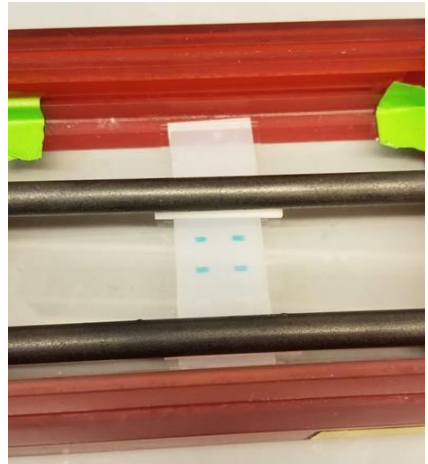
7. Place NetFix-gel on a glass slide and in the fsPAGE electrophoresis chamber. Place wicks soaked in run buffer on the surface of the gel



fsPAGE electrophoresis chamber



8. Place electrodes on top of the wicks and then fill the wells with 0.5 μ L of protein sample



9. Connect electrode to power source and run separation

4.6 References

- (1) *Protein Transfer Technical Handbook*; Thermo Fisher Scientific, 2015.
- (2) Molho, J. I.; Herr, A. E.; Mosier, B. P.; Santiago, J. G.; Kenny, T. W.; Brennen, R. A.; Gordon, G. B.; Mohammadi, B. Optimization of Turn Geometries for Microchip Electrophoresis. *Anal. Chem.* **2001**, *73* (6), 1350–1360.
<https://doi.org/10.1021/ac001127+>.
- (3) Rodbard, D.; Chrambach, A. Unified Theory for Gel Electrophoresis and Gel Filtration. *Proc. Natl. Acad. Sci.* **1970**, *65* (4), 970–977.
<https://doi.org/10.1073/pnas.65.4.970>.
- (4) Ferguson, K. A. Starch-Gel Electrophoresis-Applications to the Classification of Pituitary Proteins and Polypeptides. *Metabolism* **1964**, *13* (10), 985–1002.
- (5) Morris, C. J. O R.; Morris, P. Molecular-Sieve Chromatography and Electrophoresis in Polyacrylamide Gels. *Biochem. J* **1971**, *124*, 517–528.
- (6) Herr, A. E.; Singh, A. K. Photopolymerized Cross-Linked Polyacrylamide Gels for on-Chip Protein Sizing. *Anal. Chem.* **2004**, *76* (16), 4727–4733.
<https://doi.org/10.1021/ac049686u>.
- (7) Duncombe, T. A.; Herr, A. E. Photopatterned Free-Standing Polyacrylamide Gels for Microfluidic Protein Electrophoresis. *Lab Chip* **2013**, *13* (11), 2115–2123.
<https://doi.org/10.1039/c3lc50269d>.

Chapter 5: Developing Methods to Measure the Sub-Cellular Localization of Estrogen Receptor- α (ER α) Isoforms

5.1 Introduction

Approximately 70% of breast cancers (BCa) express the oncoprotein estrogen receptor- α (ER- α) which is a key mediator controlling cell proliferation¹. Common therapies to treat ER- α + tumors include hormone therapies, such as tamoxifen, which represses transcription of ER- α target genes to reduce tumor size¹. However, approximately 60% of patients who receive hormone therapy do not see an increased 5-year survival rate,^{2,3} and ~100% of late-stage and ~50% of early-stage BCa are resistant to hormone therapies.^{4,5} Furthermore, 5~10% ER-negative breast tumors have shown sensitivity to tamoxifen, but with current treatment guidelines would not be classified to receive hormone treatment^{1,6,7}. New tools capable of identifying mechanisms of hormone response in heterogenous BCa populations will help address a major challenge in developing targeted BCa treatments.

Contemporary clinical guidelines focus on the presence of ER in the nucleus using immunohistochemistry (IHC)⁸. However, there is evidence that ER- α and truncated isoforms are involved in non-classical signaling pathways outside of the nucleus. First, membrane-bound ER- α has been shown to result in rapid activation of MAPK and Akt kinase signaling to promote cell growth⁹. Second, resistant cells that had undergone long-term Tamoxifen (TAM) treatment exhibit greater ER- α localization to the cytoplasm and plasma membrane compared to untreated cells¹⁰. Third, the identification of ER- α sub-cellular localization alone is not enough to evaluate drug sensitivity. Truncated isoform ER- α 46 is also expressed in the plasma membrane and is known to dimerize with ER- α 66 to block downstream signaling¹¹. Transfection of the isoform into TAM-resistant cells has been shown to restore drug sensitivity¹². Intriguingly, triple negative breast cancer patients who either lack the full length ER- α protein or have very low expression levels, can exhibit truncated ER isoforms.^{13,14}

Consequently, to better understand ER- α isoform mechanisms, we investigated methods for specific measurement of ER- α isoforms and the sub-cellular localization of said isoforms. While differential fractionation assays utilize separations to detect truncated isoform localization, all of these assays are bulk assays, which are subject to averaging protein expression from a population of cells such that resolution of rare protein signals are obscured as well as subject to high sample loss. With single-cell resolution, available technologies to measure protein sub-cellular localization, such as immunocytochemistry, are unable to discern truncated isoforms due to lack of antibody specificity. In a second shortcoming, these single-cell assays can be subject to fixation artifacts that generate diffusion gradients during the fixation process that cause mis-localization of proteins^{15,16}. Single-cell genomic and transcriptomic measurements such as single-cell RNA and DNA FISH or single-cell sequencing provide great insight into which and how many genes and transcripts expressed, but has been shown to be poorly correlated to single-cell protein measurements and also do not provide spatial information regarding protein activity.¹⁷

We hypothesize that differential ER- α expression intracellularly versus on the plasma membrane indicates sensitivity to ligand activation (e.g. E2, tamoxifen). Localization of ER may offer an avenue for improved classification of drug efficacy as ER- α localized to the plasma membrane participates in ligand-independent non-classical ER- α signaling pathways¹⁸. Thus, we introduce a single-cell surface receptor pull-down assay (scPD) to quantify plasma membrane localized ER- α distinct from intracellular ER- α . Furthermore, we hypothesize that expression of ER- α isoforms, particularly truncated ER- α isoforms, is another measure of drug sensitivity. As a corollary hypothesis, we posit that the sub-cellular localization of these isoforms determines which signaling pathways are activated upon ER- α activation. Thus, we will advance, validate, and apply a single-cell resolution differential detergent fractionation assay (scDDF) suitable for breast cancer cells.

5.2 Materials and Methods

Reagents

30%T, 3.3%C acrylamide/bis-acrylamide (29:1) (A3574, Sigma), ammonium persulfate (APS, A3678), and tetramethyl- ethylenediamine (TEMED, T9281) for gel polymerization, dichlorodimethylsilane (440272) and 3-(trimethoxysilyl)propyl methacrylate (440159) for wafer and glass silanization, respectively, bovine serum albumin (BSA, A7638), β -Estradiol 6-(O-carboxy-methyl)oxime:BSA (E5630), Hoechst 33342 (B2261), digitonin (D141), and urea (U5378) were purchased from Sigma-Aldrich. Triton X-100 (BP-151), phosphate buffered saline (PBS, 10010023), RPMI 1640, no phenol red medium (11-835-030), penicillin–streptomycin (15070063), wheat germ agglutinin, AF488 (W11261), BSA-FITC (A23015), and fetal bovine serum, charcoal stripped (A3382101) were purchased from Thermo Fisher Scientific. 1.5 M Tris-HCl, pH 8.8 (T1588) was purchased from Teknova, 10x tris-glycine buffer (1610734) was purchased from Biorad, and 10x Tris buffered saline with Tween 20 (TBST, 9997S) was purchased from Cell Signaling Technologies. VA-086 (61551) was purchased from Wako Chemicals. Deionized water (18.2 M Ω) was obtained using an Ultrapure water system from Millipore. N-[3-[(3-Benzoylphenyl)formamido]propyl] methacrylamide (BPMAC) was custom synthesized by PharmAgra Laboratories^{19,20}.

Antibodies.

The primary protein antibodies to GAPDH (goat pAb; SAB2500450, Sigma), GFP (goat pAb; ab6673, Abcam), β -tubulin (rabbit pAb; ab6046, Abcam), α -Actinin (rabbit mAb, 6487S, Cell Signaling Technology), ER- α (rabbit mAb; RM9101S, Thermo Fisher Scientific), FITC (mouse mAb; MA5-14696, Thermo Fisher Scientific), PTBP1 (mouse mAb; WH0005725M1, Sigma-Aldrich), CK-8 (mouse mAb; C5301, Sigma-Aldrich), and mTOR (rabbit, 2983S; Cell Signaling Technologies) were used. Secondary antibodies to goat IgG prelabelled with Alexa Fluor 647 (A21447), rabbit IgG pre-labelled with Alexa Fluor 555 or 647 (A31572 and A31573), and to mouse IgG pre-labelled with Alexa Fluor 488 or 555 (A11001 and A21424) were purchased from Thermo Fisher Scientific. All primary antibodies were used at a 1:10 dilution in 2% TBST/BSA from stock concentrations and incubated for 2 hours at room temperature, except for anti-GAPDH

and anti-ER- α , which were incubated for 3 hours at room temperature. Secondary antibodies were diluted to a 1:20 working concentration in 2% TBST/BSA from stock and incubated for 1 hour at room temperature, protected from light.

SU8 and PA gel fabrication.

SU8 fabrication to generate the master mold and PA gel fabrication were performed as described previously^{19,21}. 5%T, 6%T, and 8%T PA gels were fabricated to all have microwell diameter and depth of 30 μm and 45 μm respectively on wafers (WaferPro C04009) microfabricated with SU-8 3050 photoresist (Kayaku Advanced Materials Y311075) and coated with dichlorodimethylsilane. All PA gels on the single-cell PAGE slides were chemically polymerized with 0.08% APS and 0.08% TEMED.

Cell lines, Drug Treatment, and Cell harvesting.

MCF-7 and MCF7-GFP cells were obtained from the American Type Culture Collection (ATCC) and authenticated (Promega). Both cell lines were maintained in RPMI 1640 supplemented with 1% penicillin/streptomycin and 10% FBS. Cells were kept in a 37 °C incubator at 5% CO₂. 48 hours prior to drug treatment of MCF-7 cells, cell media was changed to phenol red free RPMI1640 and charcoal stripped FBS with 1% P/S to eliminate any estrogen activity originating from serum steroids. E6-BSA-FITC was dissolved in 1x PBS to make 1 g/L stock concentration. The stock solution was spun down to remove free E6 or free FITC dye. 400 μL was added to a centrifugal filter unit with MW cut-off of 3000 and centrifuged at 14,000 x g until 50 μL of the retentate remains. The retentate was washed 3x with 350 μL of buffer to adjust to 400 μL . BSA-FITC was dissolved in 1x PBS to make 2 g/L stock concentration. Cells were either treated with 1 μM of E6-BSA-FITC or 1 μM BSA-FITC and incubated for 30 minutes at 37°C before washing twice with 1x PBS. For single-cell PAGE, drug-treated cells were harvested using a cell scraper (Falcon, 353085), and resuspended in 4 °C 1X PBS at a concentration of $\sim 10^6$ cells per mL. For single-cell DDF, cells were harvested using 0.05% Trypsin-EDTA (Gibco, 25300-054), and resuspended in 4 °C 1x PBS at a concentration of $\sim 10^6$ cells per mL.

Single-cell PAGE.

Single-cell PAGE was performed as described previously^{19,21}. Briefly, cells were pipetted over the PA gel and settled by gravity into the microwells patterned in the PA gel. Lysis buffer heated in a water bath to 55 °C was poured over the PA gel in order to lyse the cells in the microwells for 30 seconds. An electric field ($E = 40 \text{ V/cm}$) was applied to inject and separate proteins for 30 seconds in the PA gel abutting the microwell. After separation, proteins were immobilized to the gel matrix via a 45 second exposure to UV (Lightningcure LC5, Hamamatsu) which activated the benzophenone methacrylamide cross-linked into the PA gel to immobilize proteins in the gel matrix^{19,21}. Immobilized proteins were probed in-gel by diffusing fluorescently labelled antibody probes into the PA. A fluorescence microarray scanner (Genepix 4300A, Molecular Devices) equipped with 4-laser lines ($\lambda = 488, 532, 594, 635$) acquired fluorescence readout. Subsequent rounds of antibody stripping were performed over

the course of 9 months following the protocols for multiplexed protein analysis, as detailed previously^{19,21}. Because all proteins from a single-cell are sieved in the gel matrix simultaneously and subsequently immobilized in-gel, additional targets can be immunoprobed months after the separation is performed. Previous work has demonstrated the long-term stability of single-cell PAGE slides demonstrating the ability to detect protein after 4 months of storage and the ability to strip immunoprobed protein signal after 7 months of storage⁷.

Hydrogel lid fabrication

Hydrogel lids soaked in cell lysis differential detergent fractionation buffers were used to deliver buffer to single cells and fabricated as previously described using photopatterning methods^{22,23}. Briefly, a 15% polyacrylamide precursor solution (29:1 acrylamide/bis-acrylamide) with 1% VA-086 was prepared in water. The precursor solution was pipetted between two hydrophobic glass plates that had been coated with Gel Slick and were separated by 500 μm tall spacers. The glass plates were then placed on top of a photomask containing the pattern for the lids (rectangle measuring 50 \times 70 mm), and the polyacrylamide was polymerized with ultraviolet light ($\lambda = 365 \text{ nm}$) for 45 s at 20 $\text{mW}\cdot\text{cm}^{-2}$. The completed lids measured 50 \times 70 \times 0.5 mm. Following fabrication, the lids were soaked in the appropriate buffer for at least 1 hour before use.

Single-cell differential detergent fractionation (scDDF) assay

scDDF was performed as described previously²⁴. Briefly, cells were pipetted over the PA base gel and settled by gravity into the microwells patterned in the PA base gel. After 5-10 minutes of settling, excess cells were washed off of the surface of the base gel layer with PBS, leaving only the cells in the microwells. The PBS is exchanged out of the base layer by incubating in 1x Tris-glycine for 20 s. The cell-containing base layer is transferred to the electrophoresis chamber containing carbon electrodes spaced 3 cm apart. The gel lid containing the cytoplasm-specific buffer (1% v/v Triton X-100, 0.125 mg/mL digitonin, and 0.5x Tris-glycine buffer)²⁴ was placed on top of the base layer, initiating lysis. After lysis an electric field ($E = 40 \text{ V/cm}$) was applied to inject and separate cytoplasmic proteins in the PA gel abutting the microwell. After separation, cytoplasmic proteins were immobilized to the gel matrix via a 45 second exposure to UV (Lightningcure LC5, Hamamatsu) which activated the benzophenone methacrylamide cross-linked into the PA gel to immobilize proteins in the gel matrix^{19,21}. The lid containing the cytoplasm-specific buffer was removed and replaced with the lid containing the nucleus-specific buffer (1% SDS, 0.5% mg/mL sodium deoxycholate, 0.1% v/v Triton X-100, and 0.5x Tris-glycine buffer)²⁴, initiating lysis of the intact nuclei retained in the microwells. After nuclear lysis, PAGE on the nuclear fraction was performed by applying an electric field ($E = 40 \text{ V/cm}$) in the opposite polarity of the cytoplasmic PAGE step. Following the completion of the nuclear PAGE step, the nuclear proteins were immobilized to the gel matrix via a 45 second exposure to UV which re-activated the benzophenone methacrylamide cross-linked into the PA gel to immobilize proteins in the gel matrix^{19,21}.

Chemical Stripping and Reprobing.

Harsh stripping buffer was made with 62.5 mM Tris-HCl (pH 6.8), 2% SDS, and 0.8% β -mercaptoethanol. Wash buffer consisted of 1x TBST. Gels were incubated in stripping buffer at 55–57 °C for \geq 1 hr. Gels were subsequently washed in 1x TBST for \geq 1 hr, before the next round of immunoprobings.

Immunoblot signal quantification and statistical analysis.

The data sets reported here are available from the corresponding author on reasonable request. The images were first processed in Fiji^{25,26} by applying a median filter using the “Remove Outliers” macro with a 2-pixel radius and a threshold value of 50 AFU to remove punctate noise. Then quantification of fluorescence signal from immunoblots was processed by in-house scripts written in MATLAB (R2018b) as previously described²¹. Gaussian curves were fit to fluorescence intensity profiles in MATLAB (R2018b, Curve Fitting Toolbox) in order to obtain the mean μ (used to describe the protein migration distance) and the variance σ^2 (used to calculate peak width as 4σ). Area-under-the-curve (AUC) analysis of the intensity profiles was performed to quantify immunoblot signal 4σ from the fitted-curve peak location. The signal-to-noise ratio was calculated by taking the peak value of the Gaussian fit curve and dividing by the standard deviation of the background region from the 4σ region surrounding the peak. Only protein peaks with SNR \geq 3 were included in downstream quantification of AUC and σ comparisons. Plots and statistical tests were generated and performed with R (version 3.6.1).

Cell treatment with WGA-AF488 for real-time imaging of cytoplasmic cell lysis

Naïve MCF-7 cells were treated with wheat germ agglutinin and Hoechst for real-time imaging of cell membrane lysis and cytoplasmic protein electromigration and the cell nucleus. After harvesting cells, cells were resuspended in 1x PBS solution, containing 5 μ g/mL final concentration of wheat germ agglutinin conjugated to Alexa Fluor 488. Cells were incubated in staining solution for 10 minutes at 37°C. Following staining, cells were washed twice in 1x PBS (spun down at 500g and decanting the supernatant) before Hoechst staining. The Hoechst staining solution was prepared by diluting Hoechst stock solution 1:2000 in PBS. Sufficient staining solution was added to resuspend the cells and incubated, protected from light) for 30 minutes. After incubation, cells were washed 3x in 1x PBS. For imaging, cells were settled into microwells following the single-cell PAGE and scDDF protocols. The electrophoresis chamber was placed on the stage of an epifluorescence microscope with a 20x objective lens and set for time lapse imaging with the FITC filter set. The time-lapse was started and a gel lid that had been previously incubating in cytoplasmic lysis buffer was immediately placed on top of the base gel.

5.3 Results and Discussion

Quantifying plasma membrane localized ER- α distinct from intracellular ER- α

To differentiate membrane-bound from nuclear ER- α isoforms we build upon the current scWB assay by introducing a preliminary step where we specifically tag ER- α located on

the plasma membrane²⁷. We utilize an estrogen ligand (estradiol, E2) conjugated to a bulky, hydrophilic BSA-FITC molecule that is unable to permeate the cell membrane, thus binding only the ER- α localized to the cell surface. We then analyze the treated cells in a scWB assay, lysing the tagged cell and subjecting the protein to single-cell electrophoretic separations and immunoblotting. Due to the molecular weight (MW) of the BSA molecule (66 kDa) conjugated to E2, we alter the electrophoretic mobility of only the plasma membrane-localized ER- α that were bound by E2-BSA-FITC such that it does not migrate with intracellularly localized ER- α monomer protein peak (66 kDa). After electrophoretic separation, the proteins are immobilized in the gel via a UV-activated benzophenone moiety that was incorporated during gel fabrication to enable later detection via immunoprobings using antibodies specific to ER- α and FITC, to detect the monomer and complex, respectively.

The unconjugated ligand-receptor interaction has reported K_d values in the < 1 nM range as measured by multiple measurement techniques, SPR and FRET.^{28,29} SPR has also been used to measure k_{on} of the interaction to be on the orders of $1.3 \times 10^6 \text{ M}^{-1} \text{ s}^{-1}$ and k_{off} as $1.2 \times 10^{-3} \text{ s}^{-1}$. Using these values for the E2-BSA-FITC construct, we modeled the association for complex formation and determined that binding occurred within ~ 10 seconds, and well below the time of 30 minutes we currently use to treat the cells. We then modeled the dissociation rate to determine how much of the complex remained during the time it takes to run our scPD assay. The cell lysis and electrophoresis steps in the scPD assay are 30-40 seconds each and using our model we determined that at 80 seconds, $\sim 90\%$ of the complex is maintained in our system.

The limit of detection for our existing single-cell targeted proteomic tools has been previously reported to be 27,000 molecules.¹⁹ It is reported that that 10-20% of total ER- α protein is localized to the plasma membrane⁹ and protein abundances of ER- α range from 3.17 ppm to 34.5 ppm, depending on cell type.³⁰ Accounting for protein losses during the assay, the amount of remaining ER- α protein molecules in our system ranges from 4,000 to 95,000 molecules. Thus, we should be able to detect ER- α in cells that have abundant ER- α expression.

To investigate if the 264 kDa-complex receptor-ligand complex was beyond the exclusion limit of the gel matrix, we performed scWB assays, varying the total polyacrylamide percentage (%T) and probing for a set of 'ladder' proteins of known molecular weight to perform Ferguson analysis (Figure 5-1). As the %T increases the pore size of the gel decreases. At higher %T gels, there is a greater chance of size-excluding larger MW proteins from the matrix, however with lower %T gels that have a larger pore size, there is a trade-off with increased diffusional losses during the assay. Thus, we tested 3 different gel polyacrylamide concentrations: 5%T, 6%T, and 8%T, and immunoprobed for three 'ladder' proteins: mTOR (289 kDa), Actinin (103 kDa), and β -tubulin (50 kDa) (Figure 5-1). From this study, we observed that we were able to detect mTOR, a protein of larger MW (289 kDa) than our E2-ER α complex of interest, in both conditions. Thus, we concluded that the complex would not be size-excluded from either gel composition.

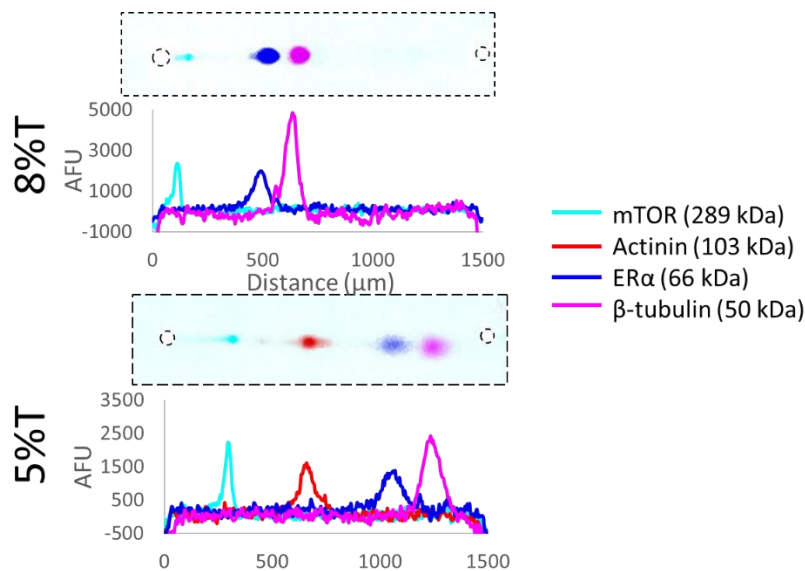


Figure 5-1. Internal 'ladder' protein controls of known molecular weight are used to predict migration distance of our complex of interest in different gel compositions.

False-colored micrographs of single-cell western blot performed with an 8%T gel (top) and 5%T gel (bottom), detecting ER- α and internal 'ladder' controls (mTOR, Actinin, and β -tubulin). For all conditions, a 30 second cell lysis step was followed by applying an electric field at 40 V/cm for 30 seconds to electrophorese proteins into the gel. With the lower %T gel, proteins had a greater electrophoretic mobility and migrated further into the gel.

Next, we investigated whether the scPD could distinguish protein lysates from individual cells with and without E2-BSA-FITC at the cell membrane. Before cell settling in the scPD assay, we treated MCF-7 cells with either 1 μ M E2-BSA-FITC or 1 μ M BSA-FITC. After performing lysis and electrophoresis with the ligand-stimulated cells, we assessed the presence of ER- α isoforms by probing with an anti-ER- α antibody. To specifically detect the ligand-receptor complex, we used an anti-FITC antibody. Similar to previous confocal data, we detected that multiple microwells that were positive for ER- α 66 also retained FITC signal at the edge of the microwell (Figure 5-2). As expected, we did not discern any FITC signal immobilized in the scPD separation lanes – implying that BSA-FITC does not bind to the cell.

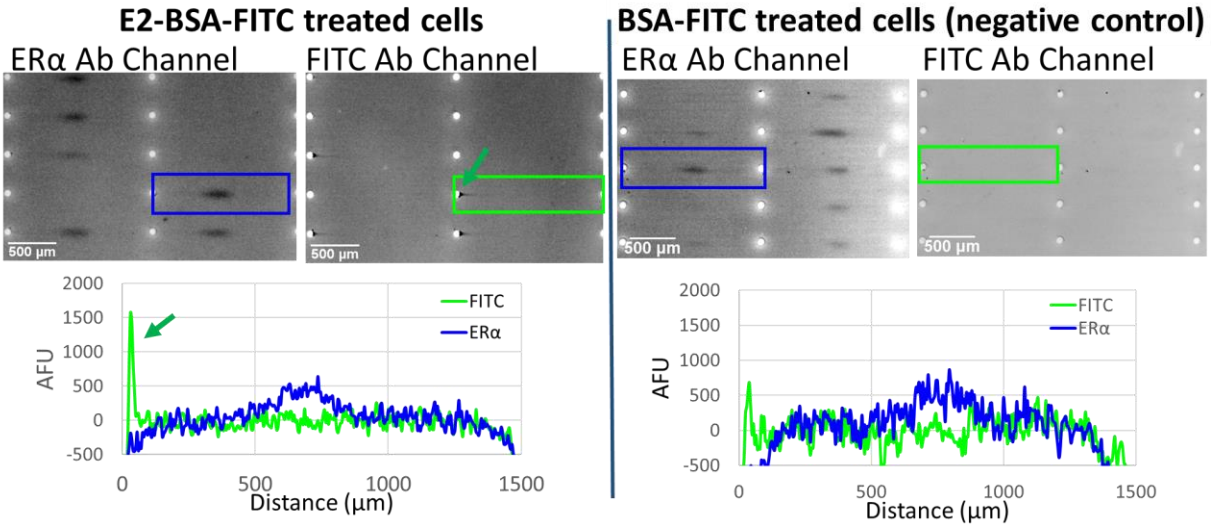


Figure 5-2: Single-cell pull down blot of MCF-7 cells with E2-BSA-FITC stimulation reveals the membrane-bound E2-BSA-FITC ligand. False-colored micrographs and corresponding intensity profiles from E2-BSA-FITC treated cells (left) suggesting the presence of ER- α 66 (blue) and bound E2-BSA-FITC (green) at the edge of the microwell. Compared to negative control BSA-FITC treated MCF-7 cells (right) that only have detectable ER- α 66 peaks and no detectable peaks in the FITC channel.

Analyzing only separations lanes that had ER- α signal, we compared the number of lanes that also had FITC signal (SNR > 3) for both treatment conditions. The number of lanes with detectable FITC signal was higher for the E2-BSA-FITC treated cells, with 37% of separations lanes with ER- α signal also having FITC signal at the microwell compared to 0% of lanes in the BSA-FITC treatment condition (Figure 5-3).

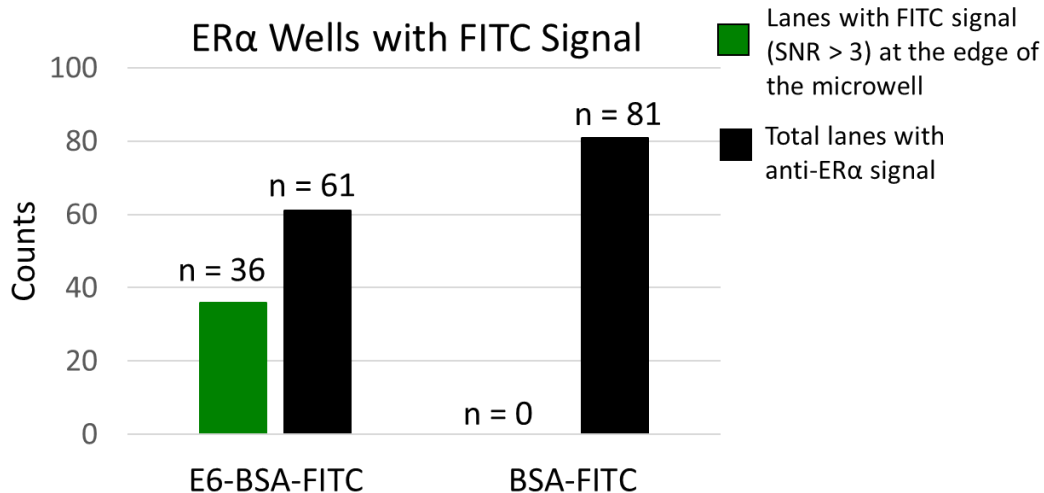


Figure 5-3: Number of microwells with ER- α 66 signal that also had FITC signal. Separations lanes positive for ER- α were analyzed for FITC signal at the microwell. E2-BSA-FITC treated cells had a higher number of individual cells (37%) with FITC signal at the microwell compared to BSA-FITC treated negative controls (0%).

Once both plasma membrane and intracellular species of ER- α can be distinctly quantified, the impact of these membrane-localized receptors on drug resistance, correlating expression with drug response, can be measured. Further analysis could include immunoprobings for protein targets involved in downstream signaling pathways known to be involved with drug resistance and compare expression levels to BSA-FITC treated cells.

Applying a single-cell resolution differential detergent fractionation assay (scDDF) toward breast cancers cells

Using previously published chemical conditions for cytoplasmic protein lysis in scDDF assays²² we were unable to isolate cytoplasmic proteins in breast cancers cells. Thus, we performed further investigation into cytoplasmic protein solubilization for selective electrophoretic separations to measure localization of ER- α isoforms.

First, to assess buffer efficacy with breast cancer cells, we initially ran the assay with an MCF-7 breast cancer cell line with transfected GFP protein expressed in the cytoplasm and immunoprobed for GFP and a nuclear control protein, PTBP1 (Figure 5-4). As expected, the GFP protein signal was detected on the cytoplasmic fraction side of the microwell, and the nuclear PTBP1 was detected on the opposite side of the microwell in the nuclear fraction.

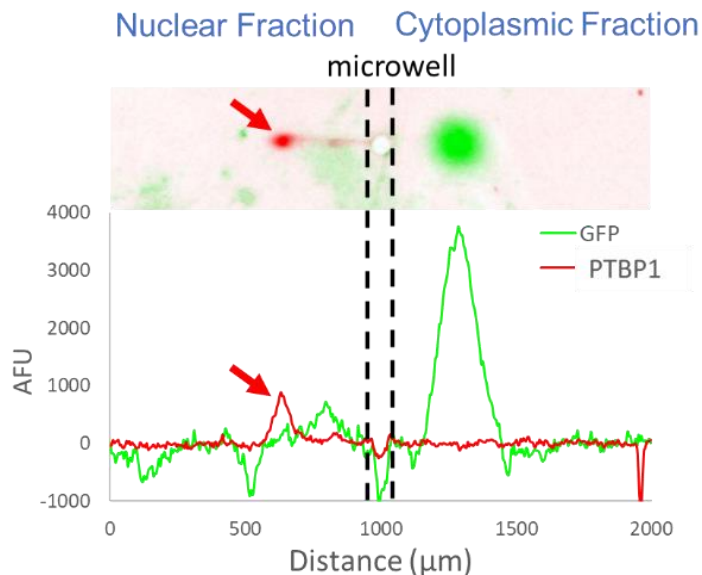


Figure 5-4. Detection of GFP protein localized to the cytoplasmic fraction and nuclear PTBP1 localized to the nucleus after performing scDDF.

False color micrographs (top) and corresponding intensity profile (bottom) of a single-cell separation lane from the scDDF assay with MFG7-GFP cells. Dotted lines indicate microwell location. Following the cytoplasmic and nuclear lysis steps, an electric field at 40 V/cm was applied for 30 s to electrophorese proteins through the 8% T gel.

Next, to investigate the robustness of the detergents to various protein targets in breast cancer cells, we immunoprobed for three 'housekeeping' proteins (β -tubulin, Keratin 8 and GAPDH) reported to be expressed only in the cytosol (Figure 5-5). However, none

of the three targets were detected in the cytoplasmic fraction of the microwell. Instead, all three protein targets either were detected in the nuclear fraction (Keratin 8 and GAPDH) or were not quantifiable, with an SNR less than 3 (β -tubulin).

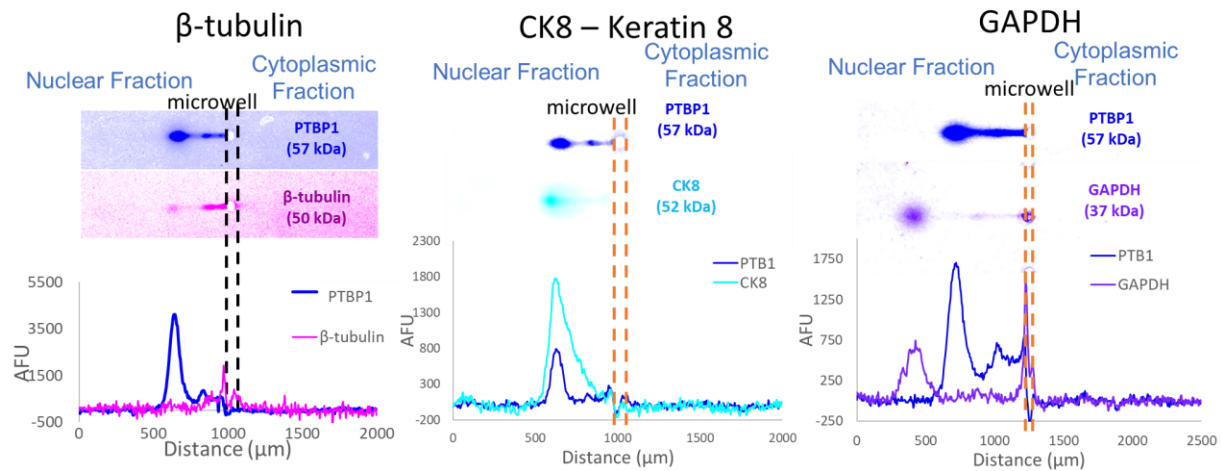


Figure 5-5: Detection of three cytoplasmic proteins in the nuclear fraction after performing scDDF. False color micrographs and corresponding intensity profiles of single-cell separation lanes from the scDDF assay with MCF-7 cells, immunoprobining for cytosolic proteins β -tubulin, Keratin 8 and GAPDH and nuclear protein PTBP1. Dotted lines indicate microwell location. Following the cytoplasmic and nuclear lysis steps, an electric field at 40 V/cm was applied for 30 s to electrophorese proteins through the 8% T gel.

From these results, we hypothesize that the current scDDF lysis buffers are not robust to fully solubilize endogenous cytoplasmic proteins and instead may only be permeabilizing the cell membrane of breast cancer cells. Permeabilization would allow the transfected GFP protein, which does not serve a biological function in the cell, and thus is not involved in interactions with other proteins, to freely diffuse out of the cell during lysis and electrophoresis. However, for endogenous protein targets such as β -tubulin and Keratin 8 that interact to form the cytoskeleton of the cell and GAPDH which is known to form tetramers, we hypothesize that the non-ionic lysis buffer does not dissociate these complexes and the pores in the cell membrane formed from permeabilization are not large enough to allow the entire protein complex to diffuse and migrate out of the cell. To confirm our hypothesis, we performed an experiment to observe and monitor lysis in naive MCF-7 cells. We treated cells with wheat germ agglutinin (WGA) labeled with Alexa Fluor 488, that binds to sialic acid and N-acetylglucosaminyl residues found on glycoproteins and glycolipids in the plasma membrane to monitor cell membrane integrity after the cytoplasmic lysis buffer was applied and during electrophoresis (Figure 5-6). After settling the treated cells into microwells, we used an epifluorescence microscope and time-lapse imaging to record fluorescence intensity profiles during cytoplasm-specific lysis and electrophoresis. When the cytoplasm-specific buffer is applied, we observe that the fluorescence signal diffuses to fill the well, indicating that the plasma membrane is breaking down. However, upon application of the electric field, we observe that most of the signal remains in the microwell and is not injected into the 8%T gel separation lane. This supports the hypothesis that there is incomplete solubilization of the plasma membrane and some cellular structure remains intact, preventing proteins from being injected into the gel.

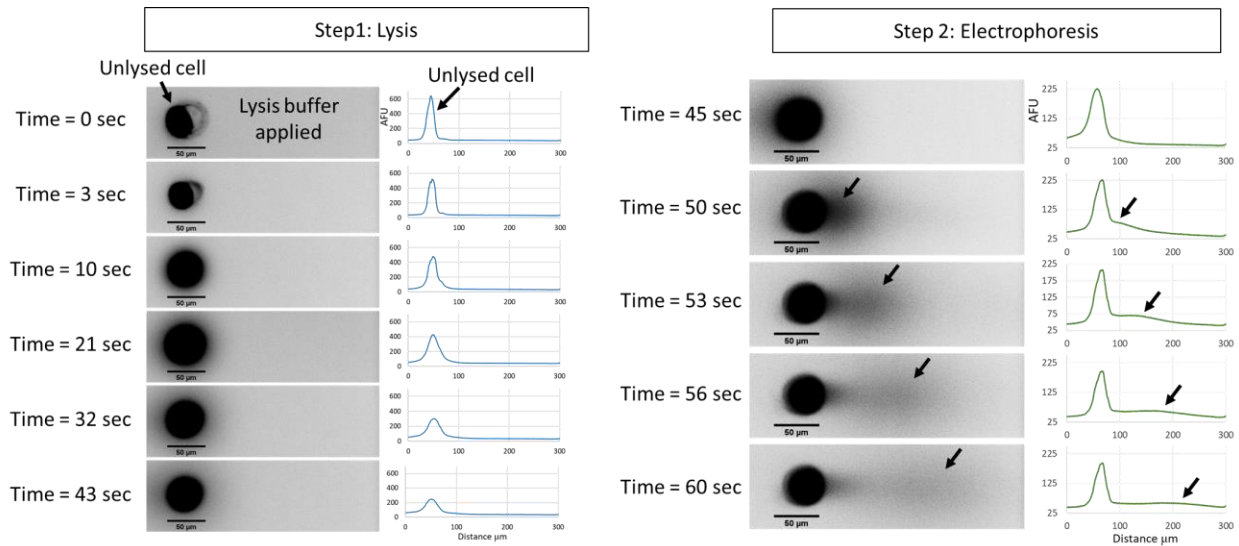


Figure 5-6: False-colored micrographs of a microwell containing a naïve MCF-7 cell that has been treated with fluorescently labelled wheat germ agglutinin that bind specifically to the plasma membrane, as it undergoes cytoplasm-specific lysis (left) and electrophoresis (right). Line intensity profiles are shown to the right of each micrograph. During lysis, the labeled WGA signal expands to fill the microwell, however during electrophoresis, a majority of the signal is retained in the microwell. All scale bars are 50 μm.

In order to improve the lysis and separations conditions for isolating and detecting cytoplasmic proteins from MCF-7 cells, we tested increasing the Triton X-100 concentration up to 10% (Figure 5-7), using convection to deliver the lysis buffer as opposed to the diffusion from a gel lid, and increasing the lysis temperature to 55°C (Figure 5-8), as well as extending the lysis time (up to 60 seconds), and electrophoresis times (up to 60 seconds) (Figure 5-9) used during the cytoplasmic portion of the assay. However, our initial results were not promising and did not show improvement for detecting endogenous cytoplasmic proteins.

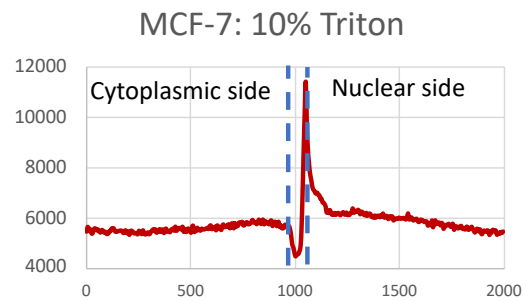
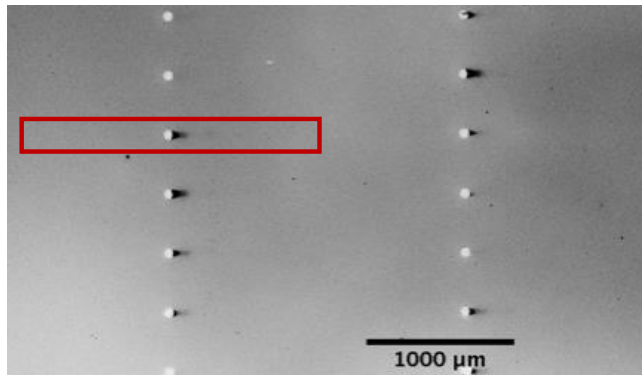
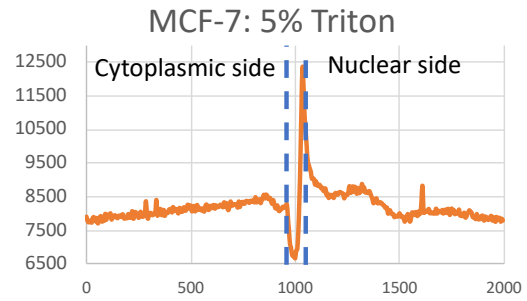
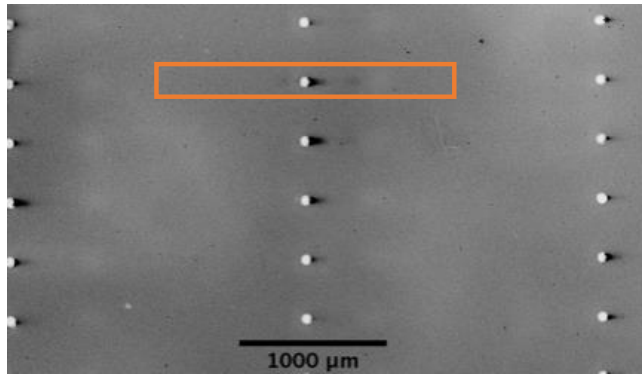


Figure 5-7: Increasing concentration of Triton X-100 in cytoplasmic lysis buffer formulation does not improve detection of cytoplasmic proteins. Triton X-100 was increased to 5% and 10% (original concentration was 1%). Cytoplasmic lysis was performed for 30 seconds and electrophoresis was performed for 30 seconds at 40 V/cm. Nuclear lysis was performed following cytoplasmic lysis per previously published protocol. Even at higher concentrations of Triton X-100, the cytoplasmic protein control β -tubulin, was not solubilized and separated during the cytoplasmic lysis step and instead was only detected after nuclear lysis and separation.

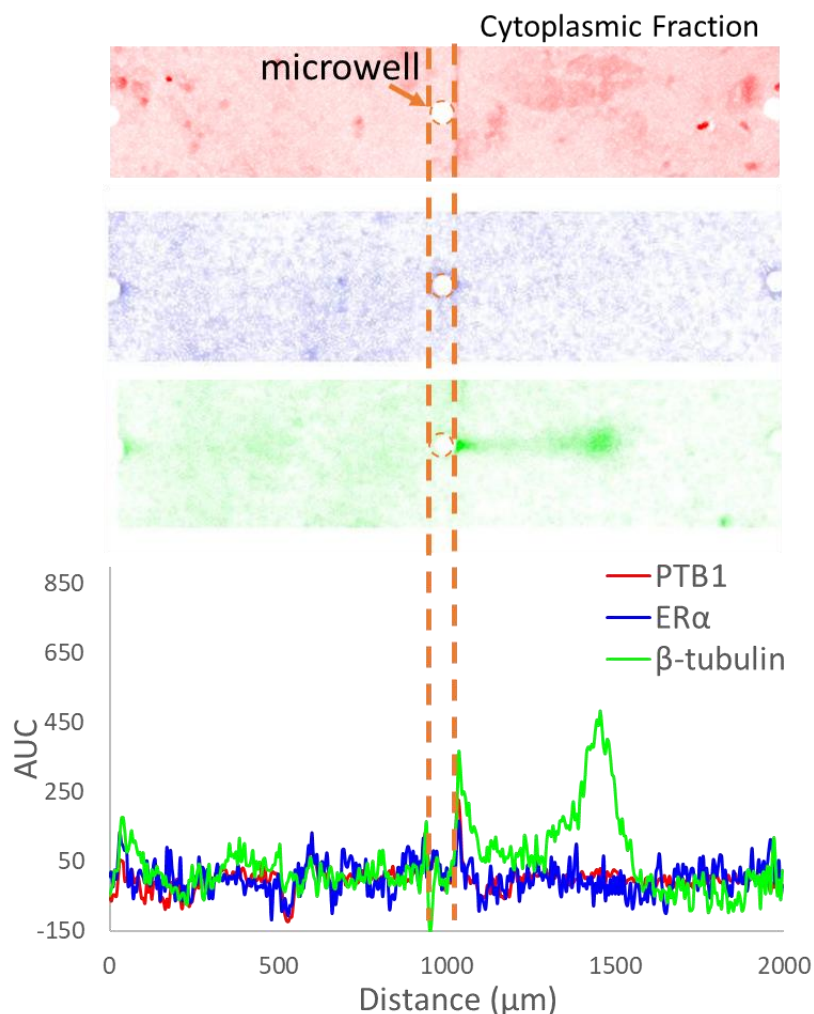


Figure 5-8: Heating cytoplasmic lysis buffer with convection delivery solubilizes β -tubulin. Cytoplasmic lysis buffer was heated to 55 °C and poured onto the microwell array gel with single cells. Lysis was performed for 30 seconds, and electrophoresis was performed for 30 seconds at 40 V/cm. The nuclear lysis step was not run. While the heated lysis buffer did enable detection of the positive cytoplasmic protein control β -tubulin, we were unable to solubilize/detect the protein target of interest, cytoplasmic ER α . Furthermore, the SNR of the detected β -tubulin peak was low (SNR ~3.1) for an abundantly expression housekeeping protein.

To improve cytoplasmic-specific lysis, alternative buffer compositions that would not disrupt the nuclear lamina structure can be investigated. One possibility is NP-40 (Nonidet P40) which is a nonionic detergent that has also been used to solubilize cytoplasmic protein in bulk assays and may be more effective solubilizing protein than Triton X-100³¹. Previous bulk studies using NP-40 to specifically study ER- α isoforms report varying success. Penot et al. previously used a 0.5% Nonidet P-40 lysis buffer in a bulk assay to isolate ER α isoforms³². However, Kocanova et. al. cited “unpublished observations” from V. Marsaud and H. Richard-Foy that low concentrations of detergents such as NP-40 may also be extracting nuclear receptors proteins, such as ER- α , which may lead to an artificial enrichment of cytoplasmic ER- α ³³. CHAPS may be another particularly promising alternative as it is as a non-denaturing zwitterionic

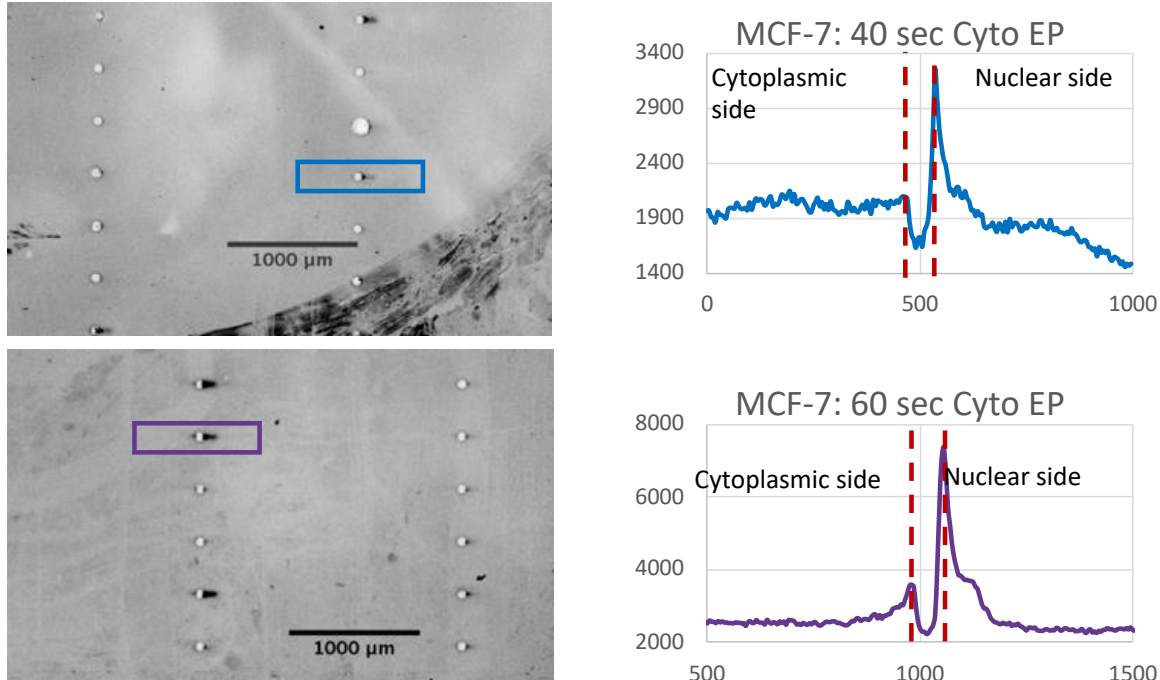


Figure 5-9: Increasing lysis times for the cytoplasmic lysis step did not improve detection of cytoplasmic proteins.

The cytoplasmic electrophoresis step, performed after lysis with gel lids, was increased to 40 seconds and 60 seconds at 40 V/cm. Nuclear lysis was performed following cytoplasmic protein immobilization per previously published protocol. Even at longer electrophoresis times, the positive cytoplasmic protein control β -tubulin, was not solubilized and separated during the cytoplasmic lysis step and instead was only detected after nuclear lysis and separation.

detergent capable of disrupting protein-protein interactions, leading to improved protein solubilization.³¹ Future experiments are necessary to determine efficacy of each detergent to selectively solubilize proteins from cytoplasm of breast cancer cells.

An initial titration experiment can determine concentrations necessary for each detergent until the cytoplasmic protein controls (β -tubulin, Keratin 8 and GAPDH) can be detected until expression levels match that of a whole cell lysis control. To ensure that the nuclear lamina is not lysed, the nuclear protein PTBP1 should be included as a negative control and should not be detected during cytoplasmic-specific lysis. However, at higher detergent concentrations it may be possible to disrupt the nuclear lamina structure and observe contamination of nuclear protein thus indicated the maximum detergent concentration.

Additionally, to evaluate the efficacy of altered detergent compositions, cell lines with fluorescently-tagged cytoplasmic proteins, such as GFP-tagged β -tubulin, can be used to directly monitor the cytoplasmic lysis and electrophoresis of target proteins in real time. Upon immunoprobing, it is expected that for each ROI containing a PTBP1 protein peak on the nuclear side of the microwell, there is a corresponding β -tubulin protein peak (SNR > 3) on the cytoplasmic side of the microwell.

5.4 Conclusions and Future Directions

These preliminary studies suggest the ability to isolate membrane-localized ER- α . However, the protein-probe complex does not migrate into the gel matrix as hypothesized. For the scPD experiments, 8%T gels were used, and further investigation is required to assess if a lower %T gel would allow the complex to be injected into the separation gel. Another method to increase pore size is by using porogen to create macropores that would be more amenable to the large protein complex migrating into the gel³⁴. Alternatively, if the complex is retained in the microwell during separations, we can determine if it is possible to perform a serial single-cell separations assay. After the protein immobilization step, we can perform a second lysis step with even stronger detergents or protein denaturants to break apart the complex. Then a second protein separations can be performed, migrating protein to the opposite side of the microwell where it is immobilized for downstream detection.

Potential problems and alternate strategies.

Detection of cytoplasmic ER- α requires that expression levels be above the limit of detection of the scWB assay (27,000 molecules).¹⁹ If the only a small percentage of total ER- α localizes to the cytoplasm and it is below the limit of detection, an alternative method to quantify could be an indirect method, whereby two samples from the same population are, one with whole cell lysis and one with the scDDF and compare the protein expression of the nuclear ER- α isoforms to whole-cell ER- α protein expression to detect if there is a shift in protein amounts detected. This would require that the assays be run as similarly as possible to compare results. It is anticipated that lower levels of nuclear ER- α expression detected with the scDDF assay, compared to whole-cell lysis levels, would be due to initial fraction and separation of cytoplasmic ER- α .

5.5 References

- (1) Manna, S.; Holz, M. K. Tamoxifen Action in ER-Negative Breast Cancer. *Sign. Transduct. Insights* **2016**, 5, STI.S29901. <https://doi.org/10.4137/STI.S29901>.
- (2) Veronesi, U.; Boyle, P.; Goldhirsch, A.; Orecchia, R.; Viale, G. Breast Cancer. *Lancet* **2005**, 365 (9472), 1727–1741. [https://doi.org/10.1016/S0140-6736\(05\)66546-4](https://doi.org/10.1016/S0140-6736(05)66546-4).
- (3) Ghayad, S. E.; Bieche, I.; Vendrell, J. A.; Keime, C.; Lidereau, R.; Dumontet, C.; Cohen, P. A. MTOR Inhibition Reverses Acquired Endocrine Therapy Resistance of Breast Cancer Cells at the Cell Proliferation and Gene-Expression Levels. *Cancer Sci.* **2008**, 99 (10), 1992–2003. <https://doi.org/10.1111/j.1349-7006.2008.00955.x>.
- (4) Osborn, J. L.; Lutz, B.; Fu, E.; Kauffman, P.; Stevens, D. Y.; Yager, P. Osborn Microfluidics without Pumps Ricco Single-Use Optofluidic Valves Microfluidics without Pumps: Reinventing the T-Sensor and H-Filter in Paper Networks †. **2010**, 10. <https://doi.org/10.1039/c004821f>.
- (5) Perey, L.; Paridaens, R.; Hawle, H.; Zaman, K.; Nole, F.; Wildiers, H.; Fiche, M.; Dietrich, D.; Clement, P.; Koberle, D.; et al. Clinical Benefit of Fulvestrant in

- Postmenopausal Women with Advanced Breast Cancer and Primary or Acquired Resistance to Aromatase Inhibitors: Final Results of Phase II Swiss Group for Clinical Cancer Research Trial (SAKK 21/00). *Ann. Oncol.* **2006**, *18* (1), 64–69. <https://doi.org/10.1093/annonc/mdl341>.
- (6) Johnston, S. R. D.; Dowsctt, M.; Smith, I. E. Towards a Molecular Basis for Tamoxifen Resistance in Breast Cancer. *Ann. Oncol.* **1992**, *3* (7), 503–511. <https://doi.org/10.1093/oxfordjournals.annonc.a058251>.
- (7) Stewart, J.; King, R.; Hayward, J.; Rubens, R. Estrogen and Progesterone Receptors: Correlation of Response Rates, Site and Timing of Receptor Analysis. *Breast Cancer Res. Treat.* **1982**, *2* (3), 243–250. <https://doi.org/10.1007/BF01806937>.
- (8) Hammond, M. E. H.; Hayes, D. F.; Dowsett, M.; Allred, D. C.; Hagerty, K. L.; Badve, S.; Fitzgibbons, P. L.; Francis, G.; Goldstein, N. S.; Hayes, M.; et al. American Society of Clinical Oncology/College of American Pathologists Guideline Recommendations for Immunohistochemical Testing of Estrogen and Progesterone Receptors in Breast Cancer. *J. Clin. Oncol.* **2010**, *28* (16), 2784–2795. <https://doi.org/10.1200/JCO.2009.25.6529>.
- (9) Márquez, D. C.; Pietras, R. J. Membrane-Associated Binding Sites for Estrogen Contribute to Growth Regulation of Human Breast Cancer Cells. *Oncogene* **2001**, *20* (39), 5420–5430. <https://doi.org/10.1038/sj.onc.1204729>.
- (10) Fan, P.; Wang, J.; Santen, R. J.; Yue, W. Long-Term Treatment with Tamoxifen Facilitates Translocation of Estrogen Receptor α out of the Nucleus and Enhances Its Interaction with EGFR in MCF-7 Breast Cancer Cells. *Cancer Res.* **2007**, *67* (3), 1352–1360. <https://doi.org/10.1158/0008-5472.CAN-06-1020>.
- (11) Li, L.; Haynes, M. P.; Bender, J. R. Plasma Membrane Localization and Function of the Estrogen Receptor Alpha Variant (ER46) in Human Endothelial Cells. *Proc. Natl. Acad. Sci. U. S. A.* **2003**, *100* (8), 4807–4812. <https://doi.org/10.1073/pnas.0831079100>.
- (12) Klinge, C. M.; Riggs, K. A.; Wickramasinghe, N. S.; Emberts, C. G.; McConda, D. B.; Barry, P. N.; Magnusen, J. E. Estrogen Receptor Alpha 46 Is Reduced in Tamoxifen Resistant Breast Cancer Cells and Re-Expression Inhibits Cell Proliferation and Estrogen Receptor Alpha 66-Regulated Target Gene Transcription. *Mol. Cell. Endocrinol.* **2010**, *323* (2), 268–276. <https://doi.org/10.1016/j.mce.2010.03.013>.
- (13) Chaudhri, R. A.; Hadadi, A.; Lobachev, K. S.; Schwartz, Z.; Boyan, B. D. Estrogen Receptor-Alpha 36 Mediates the Anti-Apoptotic Effect of Estradiol in Triple Negative Breast Cancer Cells via a Membrane-Associated Mechanism. *Biochim. Biophys. Acta - Mol. Cell Res.* **2014**, *1843* (11), 2796–2806. <https://doi.org/10.1016/j.bbamcr.2014.07.019>.
- (14) Wang, Z.-Y.; Yin, L. Estrogen Receptor Alpha-36 (ER-A36): A New Player in Human Breast Cancer. *Mol. Cell. Endocrinol.* **2015**, *418 Pt 3*, 193–206. <https://doi.org/10.1016/j.mce.2015.04.017>.
- (15) Teves, S. S.; An, L.; Hansen, A. S.; Xie, L.; Darzacq, X.; Tjian, R.; Hong, Y.; Park-Sarge, O.; Sarge, K.; Lavis, L.; et al. A Dynamic Mode of Mitotic Bookmarking by Transcription Factors. *Elife* **2016**, *5*, 421–423. <https://doi.org/10.7554/eLife.22280>.
- (16) Schnell, U.; Dijk, F.; Sjollema, K. A.; Giepmans, B. N. G. Immunolabeling Artifacts

- and the Need for Live-Cell Imaging. *Nat. Methods* **2012**, *9* (2), 152–158. <https://doi.org/10.1038/nmeth.1855>.
- (17) Schwanhausser, B.; Busse, D.; Li, N.; Dittmar, G.; Schuchhardt, J.; Wolf, J.; Chen, W.; Selbach, M. Global Quantification of Mammalian Gene Expression Control. *Nature* **2011**, *473* (7347), 337–342.
 - (18) Barone, I.; Brusco, L.; Fuqua, S. A. W. Estrogen Receptor Mutations and Changes in Downstream Gene Expression and Signaling. *Clin. Cancer Res.* **2010**, *16* (10), 2702–2708. <https://doi.org/10.1158/1078-0432.CCR-09-1753>.
 - (19) Hughes, A. J.; Spelke, D. P.; Xu, Z.; Kang, C.-C.; Schaffer, D. V.; Herr, A. E. Single-Cell Western Blotting. *Nat. Methods* **2014**, *11* (7), 749–755. <https://doi.org/10.1038/nmeth.2992>.
 - (20) Kang, C.-C.; Lin, J. M. G.; Xu, Z.; Kumar, S.; Herr, A. E. Single-Cell Western Blotting after Whole-Cell Imaging to Assess Cancer Chemotherapeutic Response. *Anal. Chem.* **2014**, *86* (20), 10429–10436. <https://doi.org/10.1021/ac502932t>.
 - (21) Kang, C.-C.; Yamauchi, K. A.; Vlassakis, J.; Sinkala, E.; Duncombe, T. A.; Herr, A. E. Single Cell–Resolution Western Blotting. *Nat. Protoc.* **2016**, *11* (8), 1508–1530. <https://doi.org/10.1038/nprot.2016.089>.
 - (22) Yamauchi, K. A.; Herr, A. E. Subcellular Western Blotting of Single Cells. *Microsystems Nanoeng.* **2017**, *3* (1), 1–9. <https://doi.org/10.1038/micronano.2016.79>.
 - (23) Duncombe, T. A.; Herr, A. E. Photopatterned Free-Standing Polyacrylamide Gels for Microfluidic Protein Electrophoresis. *Lab Chip* **2013**, *13* (11), 2115–2123. <https://doi.org/10.1039/c3lc50269d>.
 - (24) Yamauchi, K. A.; Herr, A. E. Subcellular Western Blotting of Single Cells. *Microsystems Nanoeng.* **2017**, *3* (1), 1–9. <https://doi.org/10.1038/micronano.2016.79>.
 - (25) Rueden, C. T.; Schindelin, J.; Hiner, M. C.; DeZonia, B. E.; Walter, A. E.; Arena, E. T.; Eliceiri, K. W. ImageJ2: ImageJ for the next Generation of Scientific Image Data. *BMC Bioinformatics* **2017**, *18* (1), 1–26. <https://doi.org/10.1186/s12859-017-1934-z>.
 - (26) Schindelin, J.; Arganda-Carreras, I.; Frise, E.; Kaynig, V.; Longair, M.; Pietzsch, T.; Preibisch, S.; Rueden, C.; Saalfeld, S.; Schmid, B.; et al. Fiji: An Open-Source Platform for Biological-Image Analysis. *Nature Methods*. Nature Publishing Group July 28, 2012, pp 676–682. <https://doi.org/10.1038/nmeth.2019>.
 - (27) Sinkala, E.; Rosàs-Canyelles, E.; Herr, A. E. Single-Cell Mobility Shift Electrophoresis Reports Protein Localization to the Cell Membrane. *Analyst* **2019**, *144* (3), 972–979. <https://doi.org/10.1039/C8AN01441H>.
 - (28) Rich, R. L.; Hoth, L. R.; Geoghegan, K. F.; Brown, T. A.; LeMotte, P. K.; Simons, S. P.; Hensley, P.; Myszka, D. G. Kinetic Analysis of Estrogen Receptor/Ligand Interactions. *Proc. Natl. Acad. Sci. U. S. A.* **2002**, *99* (13), 8562–8567. <https://doi.org/10.1073/pnas.142288199>.
 - (29) Tamrazi, A.; Carlson, K. E.; Daniels, J. R.; Hurth, K. M.; Katzenellenbogen, J. A. Estrogen Receptor Dimerization: Ligand Binding Regulates Dimer Affinity and Dimer Dissociation Rate. *Mol. Endocrinol.* **2002**, *16* (12), 2706–2719. <https://doi.org/10.1210/me.2002-0250>.
 - (30) Wang, M.; Herrmann, C. J.; Simonovic, M.; Szklarczyk, D.; von Mering, C.

Version 4.0 of PaxDb: Protein Abundance Data, Integrated across Model Organisms, Tissues, and Cell-Lines. *Proteomics* **2015**, *15* (18), 3163–3168. <https://doi.org/10.1002/pmic.201400441>.

- (31) Labeta, M. O.; Fernandez, N.; Festenstein, H. Solubilisation Effect of Nonidet P-40, Triton X-100 and CHAPS in the Detection of MHC-like Glycoproteins. *J. Immunol. Methods* **1988**, *112* (1), 133–138. [https://doi.org/10.1016/0022-1759\(88\)90043-9](https://doi.org/10.1016/0022-1759(88)90043-9).
- (32) Penot, G.; Le Péron, C.; Mérot, Y.; Grimaud-Fanouillère, E.; Ferrière, F.; Boujrad, N.; Kah, O.; Saligaut, C.; Ducouret, B.; Métivier, R.; et al. The Human Estrogen Receptor- α Isoform HER α 46 Antagonizes the Proliferative Influence of HER α 66 in MCF7 Breast Cancer Cells. *Endocrinology* **2005**, *146* (12), 5474–5484. <https://doi.org/10.1210/en.2005-0866>.
- (33) Kocanova, S.; Mazaheri, M.; Caze-Subra, S.; Bystricky, K. Ligands Specify Estrogen Receptor Alpha Nuclear Localization and Degradation. *BMC Cell Biol.* **2010**, *11*. <https://doi.org/10.1186/1471-2121-11-98>.
- (34) Righetti, P. G.; Caglio, S.; Saracchi, M.; Quaroni, S. 'Laterally Aggregated' Polyacrylamide Gels for Electrophoresis. *Electrophoresis* **1992**, *13* (1), 587–595. <https://doi.org/10.1002/elps.11501301119>.

Chapter 6: Conclusions and Future Directions

In this dissertation we have focused on understanding and expanding the capability of utilizing thin microscale hydrogels (~30-100 μm thick) for electrophoretic separations and subsequent in-gel protein isoform detection for single-cell analysis applications. Understanding how physicochemical phenomena influence each step of the single-cell electrophoretic cytometry workflow can guide assay design to optimize performance. Our understanding of established electromigration models has elucidated anomalous electromigration of large molecular mass proteins. Additionally, we have investigated two alternative protein capture methods: 1) an alternative photoactivatable molecule and 2) offset electrotransfer from thin gels to a blotting membrane.

For future directions, detection of a wide range of protein targets, both in terms of molecular mass and protein abundance, is necessary to understand mechanisms for disease progression and treatment. Future optimizations can be made with on-chip single-cell sample preparation, particularly for large molecular mass protein targets and for subcellular measurements. Subcellular protein expression is potentially lower than that of the whole cell, thus being able to detect lower abundance targets is critical. Furthermore, being able to detect additional protein targets can elucidate which signaling pathways are activated based on isoform location, potentially guiding therapeutic strategies and improve clinical outcomes with more personalized treatment.

Appendix

A. RT-qPCR experiments for analysis of mRNA transcript expression after drug treatment

A.1 Method

Three biological replicates were run with three technical replicates per gene, per biological replicate. MCF-7 and MDA-MB-231 cells were grown in charcoal-stripped media with. Cells were grown to confluency and treated with 1 μ M of Tamoxifen or Estradiol in ethanol for the treatment groups. Control group was treated with an equal volume of ethanol. Cells were collected 24 hours post-treatment using a cell scrapper (Corning) and centrifuged to pellet. Cell pellets were homogenized using a QIAshredder before RNA was isolated using a QIAGEN RNeasy Mini Kit. RNA was then treated with DNase using the TURBO DNA-free™ Kit (Invitrogen/ThermoFisher). One-step RT-qPCR was performed using Bio-Rad's iTaq™ Universal SYBR® Green One-Step Kit and CFX Connect™ Real-Time PCR Detection System. RT-qPCR cycling conditions were 10 minutes at 50°C, 1 minute at 95°C, [10 seconds at 95°C, 30 seconds at 60°C] (40 cycles) followed by melt curve analysis.

Each RT-qPCR reaction had a total volume of 20 μ L with a final primer concentration of 300 nM. A total of 50 ng of RNA was used for each reaction, except for RT-qPCR experiments targeting ER α transcripts in MDA-MB-231 cells which had 500 ng of starting RNA due to low levels of ER α expression (Figure A-1B). A negative control with all reaction components except for the RNA template was included for each gene of interest in order to detect primer dimers. An additional negative control reaction with all components except the Reverse Transcriptase enzyme was included for each gene of interest in each cell type to detect potential genomic amplification.

The change in gene expression due to drug treatment was assessed by calculating relative expression levels (ΔC_t) of the target gene to GAPDH, which was used as an internal control gene whose expression did not change across treatment groups. A higher ΔC_t value indicates that the overall expression was lower relative to the internal control gene (GAPDH), as it took more cycles for signal to be above the fluorescence threshold. The Kruskal-Wallis test with Dunn correction was used to compare ΔC_t between treatment groups.

A.2 Results and Discussion

Signal was not observed in any of the negative controls, indicating that there was no signal from primer dimers and no signal from genomic DNA contamination. Plot represents the relative expression, $2^{-\Delta C_t}$ value which is the difference between ΔC_t values of the treatment (E2 or TAM drug treatment conditions) and reference negative control (untreated) samples. Each point corresponds to one biological replicate, with error bars representing the confidence interval calculated from the three technical

replicates for each gene (Kruskal-Wallis test with Dunn and Sidák correction, * $p < 0.05$, ** $p < 0.1$).

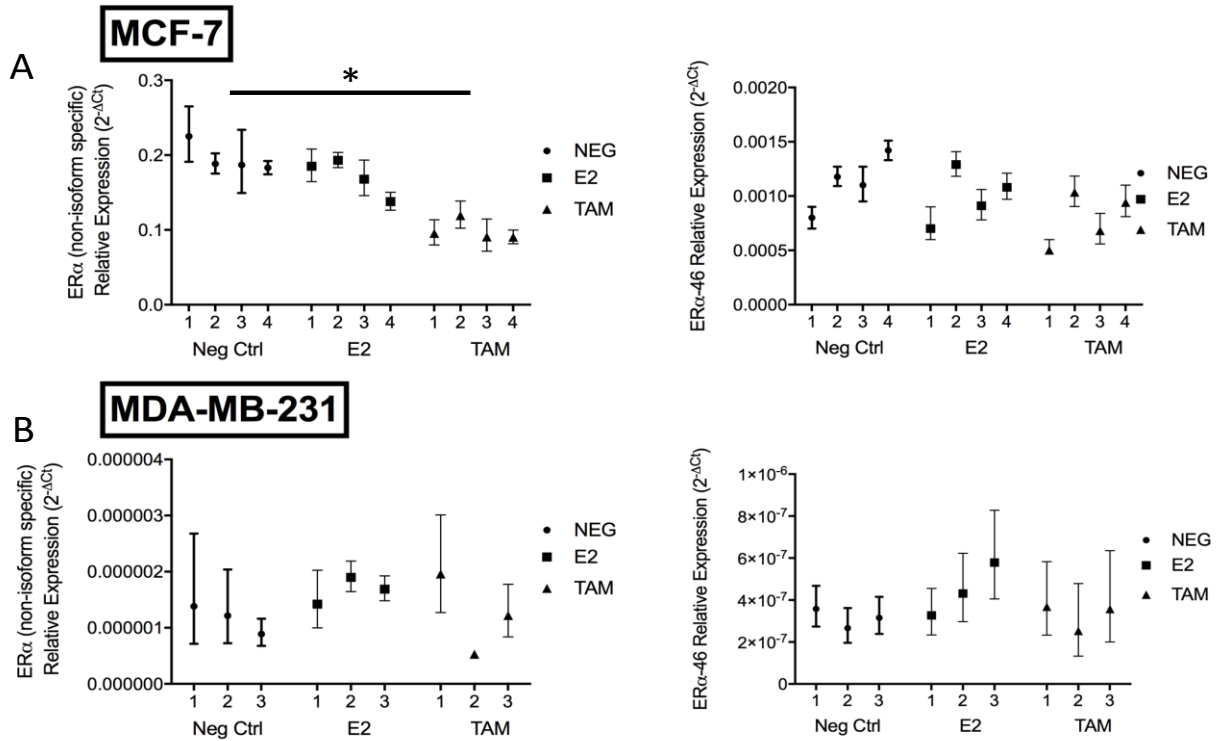


Figure A-1: Effect of Tamoxifen and E2 treatments on ER α mRNA expression.

(A) Relative expression of all ER α mRNA isoforms in MCF-7 cells in response to drug treatment (Kruskal-Wallis test with Dunn and Sidák correction, * $p < 0.05$). (B) Relative expression of all ER α mRNA isoforms in MDA-MB-231 cells. Overall the relative expression value of ER α transcripts, compared to GAPDH, is much lower in MDA-MB-231 cells. Each point represents one biological replicate. Error bars represent confidence interval calculated from variation of technical replicates

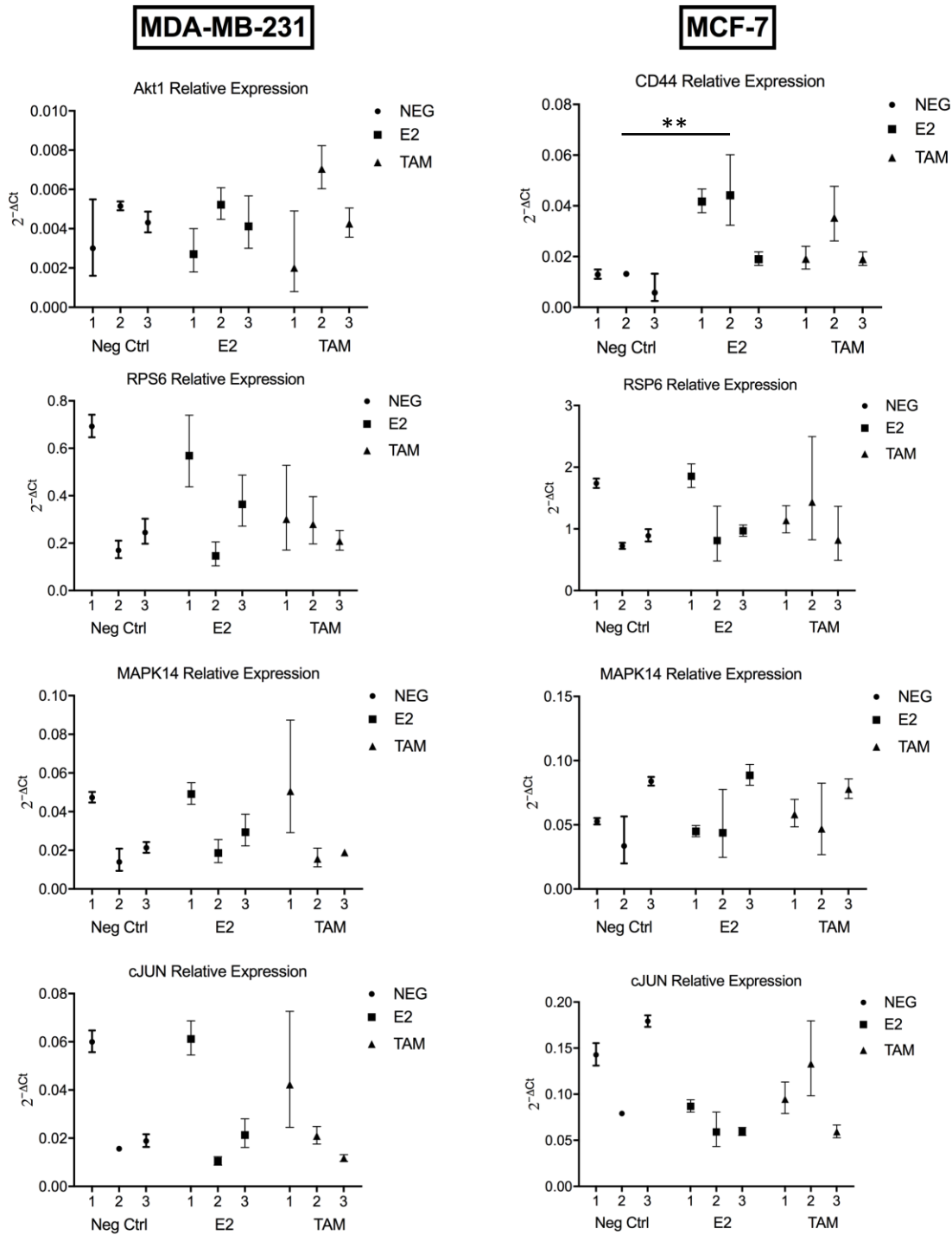


Figure A-2: Effect of Tamoxifen and E2 treatments on corresponding mRNA transcripts from ER α signaling pathways for MDA-MB-231 and MCF-7 cell lines. Kruskal-Wallis test with Dunn and Sidák correction, **p < 0.1 (exact p-value = 0.06). Each point represents one biological replicate. Error bars represent confidence interval calculated from variation of technical replicates.

A.3 Supplementary Information

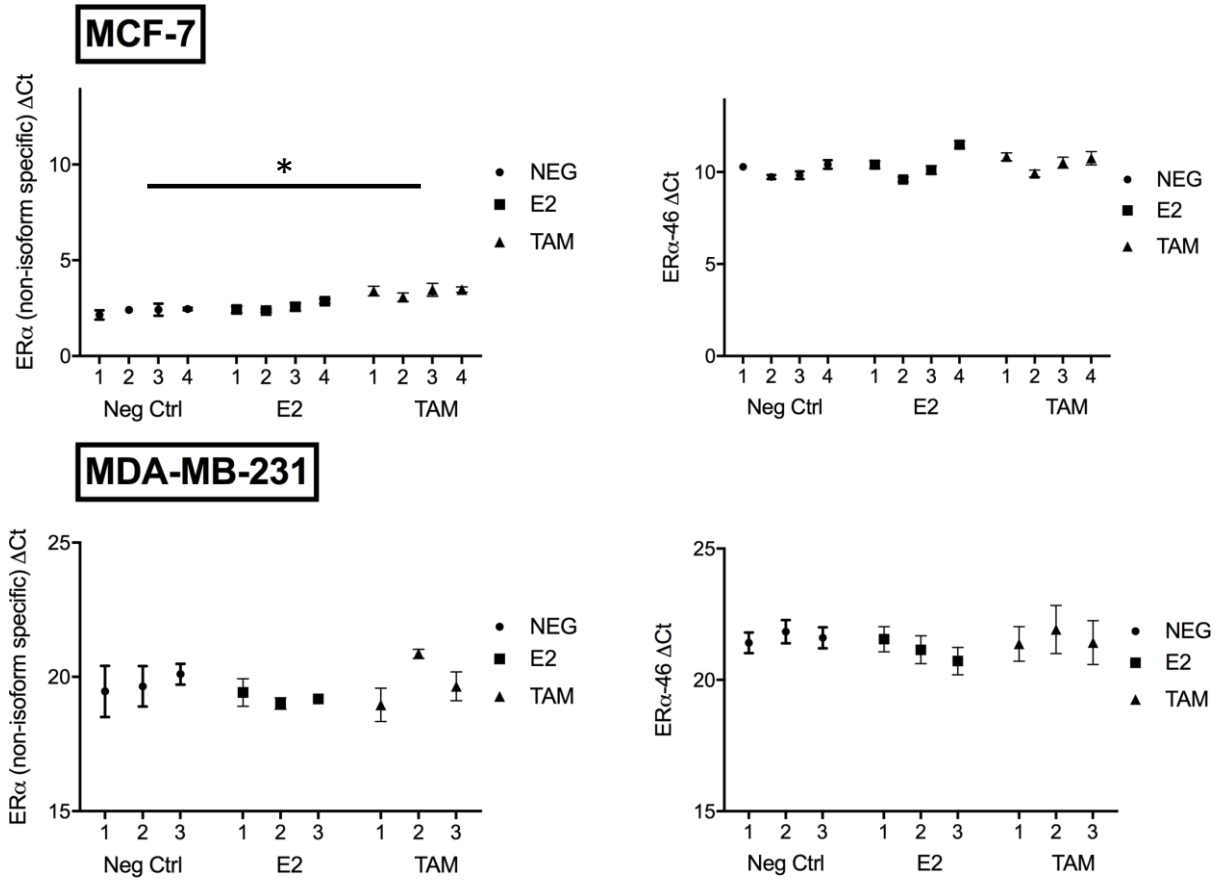


Figure A-3: ΔC_t values for ER α mRNA transcript expression

ΔC_t was calculated from $C_{t \text{ target}} - C_{t \text{ reference}}$. Error bars represent standard deviation, calculated from error propagation of standard deviation of technical replicates.

Table A-1: RT-qPCR Primers used in experiments.

All primers were designed using the IDT RealTime qPCR Assay Entry tool (<https://www.idtdna.com/scitools/Applications/RealTimePCR/>) or chosen from the RT primer database (www.rtprimerdb.org) which is a database of primers that have been used in publications.

Primer Name	Target Gene	Fwd Sequence	Rev Sequence
16_GAPDH	GAPDH	ACATCGCTCAGACACCATG	TGTAGTTGAGGTCAATGAAGGG
P38-MAPK	MAPK14	ACATTGTTTCCTGGTACAGACC	AGTTCATCTTCGGCATCTGAG
10_RPS6	NM_001010 (RPS6)	TGATGTCCGCCAGTATGTTG	TCTTGGTACGCTGCTTCTTC
9_AKT1	NM_005163.2 (AKT1)	GCAGCACGTGTACGAGAAGA	GGTGTCAGTCTCCGACGTG
7_CD44	NM_000610.3 (CD44)	TGCCGCTTTGCAGGTGTAT	GGCCTCCGTCCGAGAGA
5_JUN	NM_002228.3 (JUN)	TCGACATGGAGTCCCAGGA	GGCGATTCTCTCCAGCTTCC
ERall	NM_000125 (ESR1) All isoforms	CAGGGAGAGGAGTTTGTGTG	AGGTGGATCAAAGTGTCTGTG
ER66_1	Only ER α -66	GGACTGCACTTGCTCCCGT	AGAGCACAGCCCGAGGTTAG
ER66_2	Only ER α -66	TTCGTCCTGGGACTGCACTTG	AGAGCACAGCCCGAGGTTA
ER46	XM_006715375.3	ACTCTCCACCCACTTACCGT	GGAGGTGTTTTCCCCACAA

Table A-2: List and description of primers tested using RT-qPCR

Primer Name	Transcript Target	Notes
GAPDH	GAPDH	
ER α _all	All ER α isoforms	Designed to target Exons 2-8
ER α -E1	ER α -66 only	Designed for Exon 1 of mRNA transcript
ER α -66	ER α -66 only	Designed from the first 685 bp of ER α -66 mRNA sequence
ER α -46	ER α -46 only	Designed from the first 793 bp of ER α -46 mRNA sequence

The protein structure of ER α -46 is a truncated version of ER α -66 that is missing the first domain which functions as the Activation Function 1 domain (AF-1). Therefore, ER α -66-specific primers were designed to target the first exon of the ER α mRNA transcript (Figure A-5). A primer to target all the ER α isoforms was also selected by targeting a region common to all isoforms to amplify. Using BLAST to compare the reported ER α -66 mRNA sequence with the predicted ER α -46 mRNA sequence, we realized that the first ~700 bp of the ER α -46 transcript were unique, and so we designed a primer to target that region to determine if we could detect only the ER α -46 mRNA. (Figure A-5).

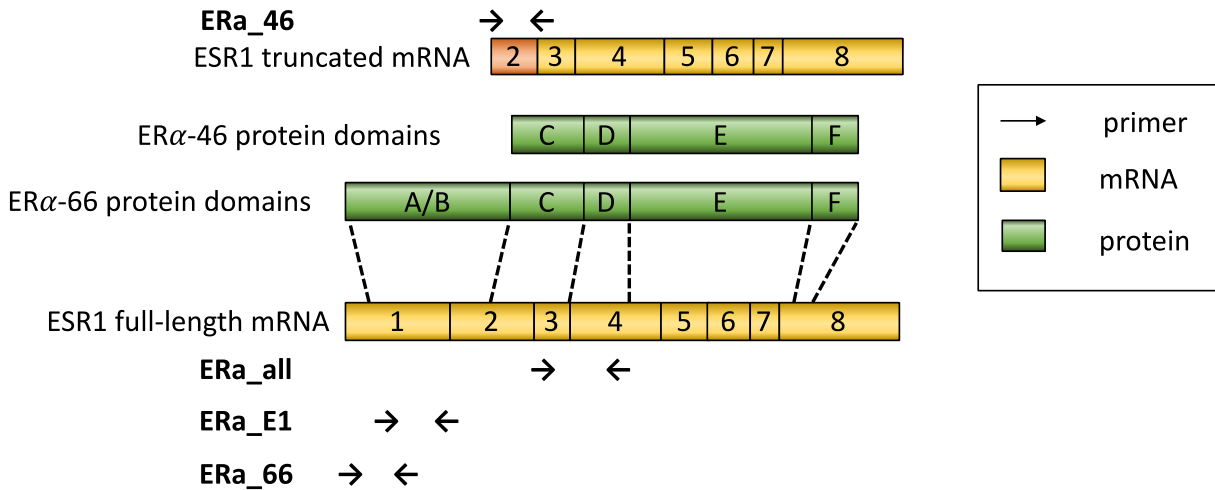
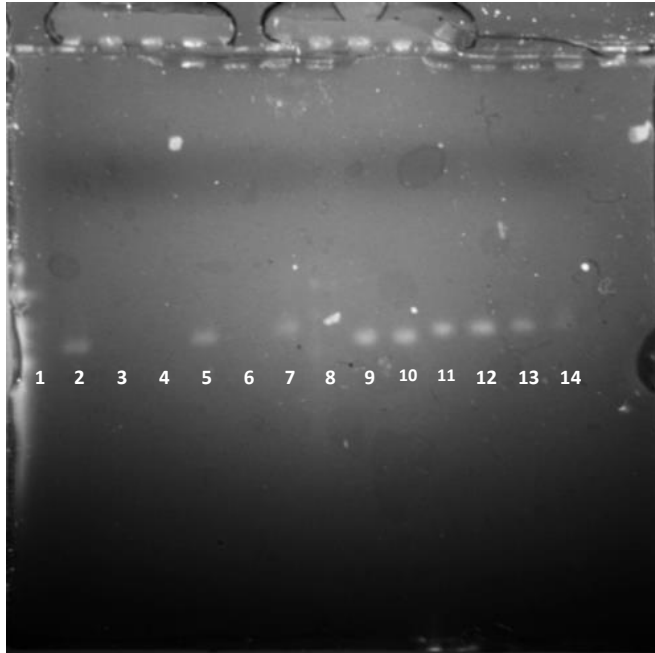


Figure A-5: Schematic of ER α protein domains and how they map to the mRNA transcript sequence. Arrows depict where the primers are designed to target.

Validation of RT-qPCR primers

In order to determine what is being amplified we decided to run the RT-qPCR product on an agarose gel to determine the size of the amplified cDNA product. Unfortunately, when we ran the first gel, the ladder did not show up in the gel, either because it was not stained properly or because it was not correctly added to the gel (Figure A-6). However, from the gel, we can identify that as expected, ER α _all negative controls and the GAPDH_noRNA negative control do not have a band. We also observe the same size products for the other ER α primers in both the sample and the 'noRT control' indicating that the same target is being amplified in both reactions. Furthermore, all the DNA bands are roughly the same length which corresponds to the predicted ER α _all and GAPDH product length of ~130 bp, so ER α _E1, ER α _66, and ER α _46 are also around that size (Table A-1). These results indicate that we have probably amplified our intended target, but from genomic DNA as opposed to RNA.



Lane	Sample
1	Ladder
2	ERa_all MCF7
3	ERa_all MCF7_noRNA
4	ERa_all MCF7_noRT
5	GAPDH_HEK
6	GAPDH_HEK_noRNA
7	GAPDH_HEK_noRT
8	Ladder
9	ERa_E1 MCF7
10	ERa_E1 MCF7_noRT
11	ERa_66 MCF7
12	ERa_66 MCF7_noRT
13	ERa_46 MCF7
14	ERa_46 MCF7_noRT

Figure A-6: RT-qPCR product run on a 2% agarose gel. The gel was run at 5 V/cm for 47 minutes followed by staining with SYBR safe DNA stain for 30 min. Ladders were either not added properly or were not stained properly and did not show up during imaging. For ER α isoform specific primers, the product length of the sample and the no RT control are the same.

To confirm our results, we ran a second gel with the DNA stain incorporated into the gel and with the ladders at a higher concentration than the first gel and we were able to see the ladder this time (Figure A-7). The RT-qPCR amplified product does indeed look like it's the same size as the intended product, which indicates that we are amplifying DNA and that the abundance of mRNA of these targets is very low, relative to the DNA contaminants.



Lane	Sample
1	Ladder
2	ERa_all MCF7
3	ERa_all MCF7_noRT
4	GAPDH_HEK
5	GAPDH_HEK_noRT
6	Ladder
7	ERa_E1 MCF7
8	ERa_66 MCF7
9	ERa_46 MCF7
10	Bank
11	ERa_46 MCF7_noRT

Figure A-7: RT-qPCR product run on a 2% agarose gel with SYBR safe stain. The gel was run at 5 V/cm for 43 minutes. The SYBR safe stain was incorporated in gel precursor before gel was cast. Additionally, 2 μ L of DNA ladder was run, instead of the 1 μ L used previously in Figure A-6. DNA bands appear between 150 - 200 bp in size, which match the intended target sequence.

We analyzed results from two RT-qPCR experiments to test efficacy of ER α primers and determined that contamination from genomic DNA is contributing to results. As a result, we need to use DNase during RNA extraction to degrade any genomic DNA remaining in the isolated RNA sample. We also designed and ordered new isoform-specific primers to test with DNase treated RNA samples (Figure A-8)

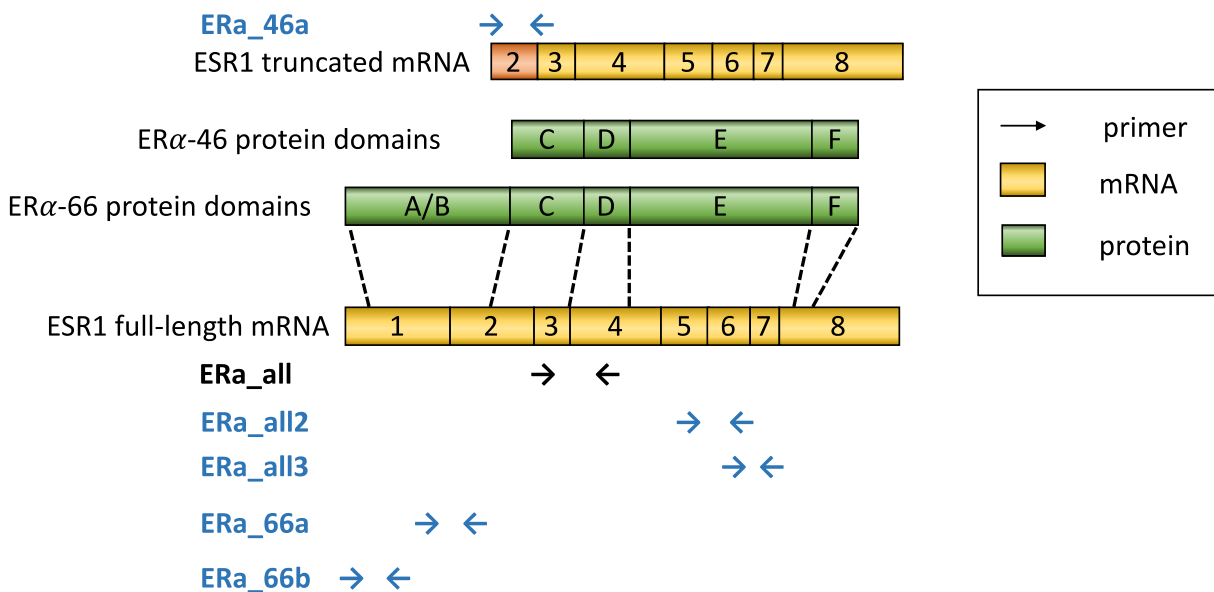


Figure A-8: Location of new primers ordered (blue) ER α -46 and ER α -66 primers are in the same general location, targeting the same exon, but different sequences from previous primers.